

ABSTRACT

Title of dissertation: ATMOSPHERIC CHARACTERIZATION
 OF GIANT EXOPLANETS
 IN EXTREME ENVIRONMENTS

Ashlee Wilkins, Doctor of Philosophy, 2017

Dissertation directed by: Professor Drake Deming
 Department of Astronomy

The study of planets around other stars has entered a science-rich era of characterization, in which detailed information about individual planets can be inferred from observations beyond discovery and confirmation, which only yield bulk properties like mass or radius. Characterization probes more revealing quantities such as chemical abundances, albedo, and temperature/pressure profiles, allowing us to address larger questions of planet formation mechanisms, planetary evolution, and, eventually, presence of biosignature gases. The primary method for characterization of close-in planets is transit spectroscopy. My dissertation comprises transiting exoplanet case studies using the *Hubble Space Telescopes* Wide-Field Camera-3 (*HST*/WFC3) as a tool of exoplanet characterization in a near-infrared band dominated by broad water absorption. Much of my efforts went toward a characterization of the WFC3 systematic effects that must be mitigated to extract the incredibly small (tens to 200 parts per million) signals. The case study subjects in this dissertation are CoRoT-2b (in emission), WASP-18b (in transmission and emission),

and HATS-7b (in transmission), along with some partial/preliminary analyses of HAT-p-3b and HD 149026b (both in transmission). I also present an analysis of transit timing of WASP-18b with HST and other observatories as another clue to its evolution as a close-in, extremely massive planet purported to be spiraling in to its host star. The five planets range from super Neptunes to Super-Jupiter in size/mass. The observability of such planets – i.e. giants across a continuum of mass/size in extreme local environments close to their respective host stars, – is a unique opportunity to probe planet formation and evolution, as well as atmospheric structures in a high-irradiation environment. This genre of observations reveal insights into aerosols in the atmosphere; clouds and/or hazes can significantly impact atmospheric chemistry and observational signatures, and the community must better understand the phenomenon of aerosols in advance of the next generation of space observatories, including JWST and WFIRST. In conducting these case studies as part of larger collaborations and *HST* observing campaigns, my work aids in the advancement of exoplanet atmosphere characterization from single, planet-by-planet, case studies, to an understanding of the large, hot, gaseous planets as a population.

Atmospheric Characterization of Giant Exoplanets in Extreme
Environments

by

Ashlee Wilkins

Dissertation submitted to the Faculty of the Graduate School of the
University of Maryland, College Park in partial fulfillment
of the requirements for the degree of
Doctor of Philosophy
2017

Advisory Committee:

Professor Drake Deming, Chair

Professor Doug Hamilton

Professor Andy Harris

Professor Lee Mundy

Dr. Avi Mandell

Dr. Daniel Lathrop, Representative of the Dean of the Graduate School

© Copyright by
Ashlee Wilkins
2017

Preface

Much of this thesis has been published in peer-reviewed journals and/or presented at international conferences. Chapter 3 was published in *The Astrophysical Journal* as "The Emergent 1.1-1.7 Micron Spectrum of the Exoplanet CoRoT-2b as Measured Using the Hubble Space Telescope" (Wilkins et al., 2014). Chapter 4 was published in *The Astrophysical Journal Letters* as "Searching for Rapid Orbital Decay of WASP-18b" (Wilkins et al., 2017). Chapter 5 is in preparation to be submitted to *The Astronomical Journal*. Chapter 2 contains some analysis supplemental to, but not previously published with, Chapters 3, 4, and 5, as well as some preliminary results that will be included in a future journal article. Results from Chapter 3 were presented at the *217th Meeting of the American Astronomical Society* in January 2012 and the *General Assembly of the European Geosciences Union* in April 2013. Preliminary and final results from chapters 2, 3, 4, and 5 have been presented at the *Twenty Years of Giant Exoplanets Conference* in October 2015, the *ExoClimes Conference* in August 2016, and the *229th Meeting of the American Astronomical Society* in January 2017.

Hubble data were taken as part of Cycle 18 (Program ID: 12181, PI:Deming), Cycle 23 (Program ID: 14260, PI:Deming), and an archival Cycle 22 program (Program ID: 13467, PI: Jacob Bean).

*“Curiouser and curiouser!’ cried Alice
(she was so much surprised, that for the moment
she quite forgot how to speak good English).”*

*Lewis Carroll, **Alice’s Adventures in Wonderland***

Acknowledgments

The community at the UMD Department of Astronomy has been paramount to my survival these last seven years. Thank you for welcoming me into the community, for valuing my voice in it, and for helping me grow as a scientist, a scholar, and person. Thank you to all of you who are stewards of this community, formal or informal. You have been my friends, my colleagues, my mentors, my inspiration. I am proud to have been a part of this village. Every one of you has made this community what it is for me, but I would like to especially acknowledge my classmates, Taro, Kory, John, Kim, Alice, and Maxime; the senior-to-me graduate students who were friends and mentors, Katie, Alex, Jithin, Megan, Che-yu, Shaye, and Daniel; the Peanut Butter Padis, Gabriele and Krista; and, of course, Stuart Vogel, mentor to me, department chair and driver of so much good in the department.

Somehow, I managed to enter the University of Maryland just as Drake Deming was transitioning to a faculty position; I am so grateful for that lucky break and Drake's willingness to usher me into the world of exoplanet science. The work of this dissertation quite literally would not have been possible without him; his dedication to the science and his incredible skill at writing NASA observing proposals provided me with both a trove of data and a fully engaged advisor who was always waist-deep in the science, the data, and the coding with me. Thank you, Drake, for your support, patience, kindness, and understanding of my guacamole mistakes.

Thank you to the members of my thesis committee: Doug Hamilton, Andy Harris, Avi Mandell, Lee Mundy, and Daniel Lathrop, for ensuring that I leave UMD

a capable and tested scientist. Thank you to Aki Roberge, who ultimately could not attend my defense – thank you, Avi, for stepping up – but who has been a font of knowledge and honest engagement for many years.

Amy Mainzer was the first scientist who truly made me believe that I could do this: that I could be an astronomer, full stop. Not just an astronomy student; just an astronomer-in-training; or just a girl who loved books, but also thought NASA was cool and that she could play-act as a scientist sometimes; but a capable colleague with something to contribute. Her support and encouragement has sustained me in the years since I left JPL.

Thank you to the educators of Cornell, especially Julie Thom, Kendra Letchworth-Weaver, Ravi Ramakrishna, and Terry Herter, for giving me the foundations of advanced math and science, and for modeling a dedication to teaching and passion for your fields.

Thank you to my mom, Shelli Sprouse, for long phone conversations, even though I do not call often enough; for teaching me independence and resilience; for telling me that I could have the world, as long as I wanted to put in the work; and for not doing or saying anything *too* embarrassing at my thesis defense.

Thank you to my dad, Seth Wilkins, for always, always believing in me; for asking questions and challenging me; for not excessively gloating at my finally being a Terp; and also for not doing or saying anything *too* embarrassing at my thesis defense.

(I'm counting on you, parents, with both fingers crossed).

Thank you to my sisters, Rachael and Maggie, for inspiring me with your

creative minds and combined talent for and dedication to your respective crafts (including impeccable makeup application). Thank you for always keeping me humble, and for taking care of Mom and each other while I got wrapped up in this astronomy thing.

My wife, Hannah has seen me at my worst far more than at my best, and still manages to believe in me enough for both of us.

Finally, I say this: graduate school and académie were designed to be challenging, but they were also designed to be nearly impossible for folks who do not fit into an incredibly narrow definition of “scientist.” These were features, not bugs, of the system, the former being necessary for excellence, the latter being a barrier to it. Thank you to those who came before me who broke barriers, challenged norms, and faced down exclusion so that I, and all of the ways that I do not fit into that original narrow definition, could enter and persist in this field. Thank you to those who have fought and are still fighting the battles to expand that definition further and to make the world more just and astronomy more excellent at the same time. Thank you to those who open my eyes to injustice, teach me new truths, tolerate my mistakes, and hold me accountable. To the activists and the agitators, to the community-builders and the concerned citizens, to the excluded and the empathetic: thank you. Keep up the good fight.

Table of Contents

Preface	ii
Dedication	iii
Acknowledgements	iv
List of Tables	x
List of Figures	xi
List of Abbreviations	xiii
1 Introduction	1
1.1 (Exo)Planet Formation and Evolution	3
1.1.1 Before Exoplanet Discovery: The Solar System	6
1.1.2 After Exoplanet Discovery: More Questions than Answers	8
1.2 Characterizing Exoplanets in Extreme Environments	14
1.2.1 Interactions Between Close-in Planets and their Host Stars	15
1.2.1.1 Tides	16
1.2.1.2 Mass Loss	18
1.2.1.3 Radius Inflation	19
1.2.2 Spectroscopy of Transiting Exoplanets	20
1.2.2.1 Transmission (Transit) Spectroscopy	23
1.2.2.2 Emission (Eclipse) Spectroscopy	26
1.3 Modeling Exoplanet Atmospheres	29
1.3.1 Radiative Transfer in an Exoplanet Atmosphere	30
1.3.2 Temperature and Pressure Structure	32
1.3.3 Chemistry and Line Opacities	33
1.3.4 Scale Height	36
1.3.5 Aerosols	37

2	The Hubble Space Telescope, Unexpected Explorer of Extrasolar Atmospheres	41
2.1	Why HST?	41
2.2	Planet Targets	42
2.3	The Wide Field Camera 3	43
2.4	Future Outlook for HST Targets	45
3	The Emergent 1.1-1.7 Micron Spectrum of the Exoplanet CoRoT-2b as Measured Using the Hubble Space Telescope	50
3.1	Introduction	51
3.2	Observations	53
3.3	Initial Data Analysis	54
3.3.1	Bad Pixel Correction	57
3.3.2	Background Subtraction	58
3.3.3	Wavelength Calibration	58
3.3.4	Flux Calibration	60
3.3.5	Second, Overlapping Source	62
3.3.5.1	Characterization	63
3.3.5.2	Removal	63
3.4	Systematics: Characterization	65
3.4.1	Persistence Correction	71
3.4.2	Pixel-by-Pixel Evaluation of the Hook	71
3.5	White-Light Eclipse Curve	75
3.5.1	Modified divide-oot	78
3.5.2	White-Light Eclipse Amplitude	79
3.5.3	Eclipse Central Phase	82
3.6	Calculation of the Eclipse Spectrum	82
3.6.1	Beyond divide-oot : the Differential Method	85
3.6.1.1	The Spectrum of CoRoT-2b Using the Differential Method	88
3.6.1.2	Errors	92
3.7	Implications for the Atmosphere of CoRoT-2b	96
3.7.1	A Blackbody Spectrum?	96
3.7.2	Limit on WFC3 Spectral Features	100
3.7.3	Solar Abundance Model Atmospheres	101
3.7.4	A Carbon-rich Model Atmosphere	104
3.7.5	Reprise of the Model Atmosphere Comparisons	105
3.8	Summary	106
4	Searching For Rapid Orbital Decay of WASP-18b	108
4.1	Introduction	109
4.2	New Observations	112
4.2.1	TRAPPIST	112
4.2.2	<i>Hubble Space Telescope</i>	112
4.3	Analysis: Deriving the new White Light Curves	113

4.3.1	TRAPPIST Light Curves	113
4.3.2	HST White Light Curves	115
4.4	Results: Transit Timing Evolution over Nine Years	115
4.5	Discussion: Implications of the Absence of Rapid Tidal Decay	118
4.5.1	Tidal Dissipation in G vs. F Stars	120
4.5.2	Estimating the Tidal Q' for WASP-18	123
4.6	Conclusion	125
5	The <i>HST</i> Infrared Transmission Spectrum of Hot Neptune HATS-7b	127
5.1	Introduction	127
5.2	Observations	131
5.3	HST Data Reduction	133
5.3.0.1	Wavelength Solution and Wavelength-Dependent Flat Field	133
5.3.0.2	Background Subtraction	136
5.3.0.3	Sample-up-the-ramp	137
5.3.0.4	Bad Pixels	138
5.4	Results: Extracting the HST White Light Curve and Spectrum	139
5.5	Discussion	146
5.5.1	Comparing to other sub-Saturn Spectra	147
5.5.2	A Forward Model of the Atmosphere of HATS-7b	149
5.6	Conclusion	155
5.7	Acknowledgements	156
	References	162

List of Tables

3.1	CoRoT-2 Observation Summary	53
3.2	Observed Eclipse Spectra for CoRoT-2b	94
4.1	WASP-18 parameters used for this analysis.	111
4.1	WASP-18 parameters used for this analysis.	112
4.2	WASP-18 Full Observation Summary	114
5.1	The HST Sub-Saturns	157
5.2	HATS-7 Summary of Transit Observations	158
5.3	HATS-7 HST Observation Details	158
5.4	HATS-7 System Parameters	159
5.5	HATS-7 Observed Transmission Spectrum	160
5.5	HATS-7 Observed Transmission Spectrum	161

List of Figures

1.1	The average Sun-like protoplanetary disk	6
1.2	The Periodic Table of Exoplanets	10
1.3	The occurrence of planets by size around FGKM stars	13
1.4	Phases of a transiting exoplanet	24
1.5	Mass-radius diagram of confirmed exoplanets	25
1.6	Transmission Spectroscopy of a Transiting Exoplanet	27
1.7	Starlight transmission through different exoplanet atmospheres	28
1.8	Aerosols in the Solar System	39
2.1	Mass-radius diagram of confirmed exoplanets with our HST Targets	43
2.2	Uncorrected WASP-18b Full-Phase Observation	45
2.3	Uncorrected WASP-18b Full-Phase Observation	46
2.4	Uncorrected WASP-18b Full-Phase Observation	47
2.5	White light transits of HD 149026b and HAT-p-3b	48
2.6	TESS Predicted Planet Yield	49
3.1	Flat-field-corrected spectra of TRES-2 and CoRoT-2	61
3.2	The HST direct image of CoRoT-2 and the nearby infrared source	64
3.3	The normalized signal measured from the background pixels over the course of the observations.	68
3.4	Four examples of the systematic hook pattern.	69
3.5	Examining the average shape of the hook pattern for two sets of observations.	72
3.6	A quantification of an additive effect from the detector for a selection of objects.	74
3.7	Measuring any possible dependence of the hook effect on pixel row	76
3.8	Phase plot of the uncorrected wavelength-integrated flux from the three visits of CoRoT-2	80
3.9	Wavelength-integrated light curve of CoRoT-2 after correction of the hook and visit-long ramps	83
3.10	Error analysis for the amplitude and central phase of the white light eclipse.	84
3.11	Results of the shift-and-fit procedure for CoRoT-2	89

3.12	Differential eclipses of CoRoT-2b	91
3.13	Emission spectrum of CoRoT-2b from our α and β analyses	95
3.14	Our WFC3 results for CoRoT-2b shown in the context of previous observations	98
4.1	New WASP-18 transit and eclipse light curves from TRAPPIST and HST	116
4.2	MCMC posterior probability distributions for the parameters of the quadratic fit	119
5.1	Mass-radius diagram of characterized exoplanets	132
5.2	Results of the Shift-and-Fit Procedure for HATS-7	142
5.3	HATS-7 HST corrected white light curve and residuals	143
5.4	Results of the residual permutation error estimations on the HATS-7b transit	145
5.5	Comparison of exo-Neptune spectra in scale height space	148
5.6	Compare HATS-7b spectrum to ExoTransmit models (1 of 4)	151
5.7	Compare HATS-7b spectrum to ExoTransmit models (2 of 4)	152
5.8	Compare HATS-7b spectrum to ExoTransmit models (3 of 4)	153
5.9	Compare HATS-7b spectrum to ExoTransmit models (4 of 4)	154
5.10	χ^2 goodness-of-fit measurement of the Exotransmit model spectra with various cloud heights and temperatures.	155

List of Abbreviations

AU	Astronomical Unit (1.496×10^{13} cm)
k_b	Boltzmann Constant (1.38×10^{-16} erg \cdot K $^{-1}$)
μm	micrometer (10^{-6} m)
M_{\oplus}	Earth mass (5.97×10^{27} g)
M_{\odot}	Solar mass (g)
M_J	Jupiter mass
R_{\oplus}	Earth radius (6.3710×10^8 cm)
R_J	Jupiter radius (6.9911×10^9 cm)
R_{\odot}	Solar radius (6.957×10^{10} cm)
R_p	Planetary radius
R_{star}	Stellar radius
v_{esc}	Escape velocity
CoRoT	Convection, Rotation, and planetary Transits space observatory
HAT	Hungarian-made Automated Telescope Exoplanet Survey
HATS	Hungarian-made Automated Telescope South Exoplanet Survey
HST	Hubble Space Telescope
JWST	James Webb Space Telescope
KELT	Kilodegree Extremely Little Telescope
LTE	Local Thermodynamic Equilibrium
MIPS	Multiband Imager for Spitzer
NASA	National Aeronautics and Space Administration
ppm	parts-per-million
STScI	Space Telescope Science Institute
TRAPPIST	Transiting Planets and Planetesimals Small Telescope
WASP	Wide-Angle Search for Planets

Chapter 1: Introduction

In this thesis, I present observational case studies of several planets that orbit stars beyond our own solar system; we call such objects extrasolar planets, or exoplanets. The subjects of the case studies are but a few of the more than 3500 exoplanets confirmed as of August 2017¹; that number has risen dramatically since the first discoveries trickled in one-by-one over the 1990s. Exoplanet discoveries will continue to grow at a significant pace, as a new generation of both ground-based and space-based planet-hunting facilities comes online (e.g., [Borucki et al. 2010](#); [Gillon et al. 2013](#); [Swift et al. 2015](#); [Jurgenson et al. 2016](#)). What must follow, and sometimes happen in concert with, discovery is *characterization*: the detailed study of individual planets, often via atmospheres, to understand what they are, how they came to be, and, eventually, for some, what clues they hold to how life came to be, and could (have) come to be elsewhere. The growing number of known planets allows some of this understanding through statistics on occurrence rates of different planets around different stars, but we must probe the planets themselves for more complete answers.

¹Databases: NASA Exoplanet Archive (<https://exoplanetarchive.ipac.caltech.edu/>), Exoplanet Orbit Database (<http://exoplanets.org/>), Extrasolar Planets Encyclopedia (<http://exoplanet.eu/>), Open Exoplanet Catalogue (<http://www.openexoplanetcatalogue.com/>)

The subjects of the case studies undertaken in this thesis are do not center on planets any known Earth-based life form would find remotely comfortable. The path to finding “another Earth” is a long and winding one, and it is blazed by our assembling knowledge from phase spaces that are unexpected and unexplored, filled with planets that are not just unlike Earth, but also often unlike anything we see in our Solar System. They are the missing puzzle pieces we did not know we needed, the test cases for the seemingly impossible tasks to which we wish to set our instruments and models, and the enablers of necessary practice and refinement as our observatories become more complex, and their time becomes more precious. They are not just means to an end, however; the planets of this thesis, in this early era exoplanet characterization, exist at extremes in all dimensions: they are blazingly hot (on one side, at least); they are massive; they are stretched and wrenched by powerful tides; and they are blasted with harsh UV radiation. Such environments test our theories at their boundaries; the theories break, and that is when learning happens. Chemistry and dynamics we could not have imagined are now accessible (if not always readily, hence: this thesis) via instruments conceived before we were even sure there were exoplanets, let alone populations entirely unlike the Solar System planets. Harnessing such instruments for the unintended study of unexpected planets is scientifically compelling in its own right.

We begin the thesis in this first chapter, the Introduction, with context on what is known and unknown in (exo)planet formation and evolution, particularly as it applies to giant planets that have atmospheres and orbit incredibly close to their central stars, and what we can learn through atmospheric characterization. Chapter

2 is a brief overview of the Hubble Space Telescope as a tool of exoplanet characterization, and includes unpublished preliminary and supplemental results. Chapter 3 is a refereed, published study of the thermal emission coming from CoRoT-2b, a planet nearly four times the mass of Jupiter orbiting its host star once every 42 hours. Chapter 4 is a refereed, published study of the influence of gravitational tides on the dynamical evolution of WASP-18 (the star) and its companion, WASP-18b, a planet more than ten times the mass of Jupiter that takes just 22.5 hours to complete an orbit. Finally, Chapter 5 contains a preliminary study of HATS-7 b, which in preparation for submission to a refereed journal; the planet is just 12% of the mass of Jupiter, but it is nearly twice the mass of Neptune or Uranus, and it orbits in the relatively lengthy 3.2 days.

1.1 (Exo)Planet Formation and Evolution

To understand the mysteries remaining in planetary formation and evolution, we must first identify the context and environment of planet formation, which is, of course, the formation of stars. Only the highlights are covered here, but, for a more detailed review, see [McKee and Ostriker \(2007\)](#) and references therein. Giant Molecular Clouds (GMCs), or dense, slowly-rotating nebulae of diffuse gas and dust, are the birthplaces of stars. GMCs are inhomogeneous or “clumpy;” dense cores form at the center of clumps within the cloud as gravity attracts more material until the inward-pointing gravitational force overtakes the outward-pointing gas pressure, triggering a fast collapse at a critical mass known as the “Jeans Mass.”

During the gravitational infall of material and the free-fall collapse, the conservation of energy and angular momentum cause the central material to heat up and the core to spin faster, respectively. Eventually, the densely-packed, spherical protostar in the center becomes hot enough to ignite thermonuclear fusion, and the increasing rotation speed flattens the infalling material into a disk around the protostar. This “protostellar disk” has the same initial elemental composition as the star, but the extreme temperatures, densities, and pressures in the (proto)star prevent the formation of molecular bonds, whereas complex chemical compounds can be found in the disk, which is cooler and more diffuse than the stellar interior.

That rotating disk of the leftover material from star formation provides the gas and dust needed to form planets. Temperature and density decrease radially outward, and, for the first few - 10 million years, strong winds come from the young, active central star, and gas and dust still accrete onto the star from the inner edge of the disk. Within such an environment, we can identify two potential mechanisms for planet formation:

1. *Core Accretion* ([Pollack et al., 1996](#)), through which the solid dust grains in the protoplanetary disk collide and merge to form planetesimals, eventually growing massive enough to accrete gaseous material; and
2. *Disk (Gravitational) Instability* ([Boss, 1997](#)), an analog of the initial star formation process, through which planet cores begin as overdensities within the disk that, if the disk cools rapidly enough, eventually fragment and gravitationally collapse into planets.

Core accretion is a slow process (accumulation of the solid core would take $\sim 10^{6-7}$ years, [Wetherill 1996](#)) and therefore perhaps may only function in the longest-lived gas disks ([Boss, 2002](#)), while disk instability is a rapid process, able to form gas and ice giants in $\sim 10^3$ years ([Boss, 2003](#)). The two processes result in markedly different internal structure and differentiation: nominally, a planet formed via core accretion would have a distinct solid core surrounded by a distinct gaseous envelope, while a planet formed via disk instability would demonstrate more mixing. However, the nature of the available material to build a given planet in either scenario depends on the planet’s location in the disk, with different molecules condensing at different distances from the host star ([Öberg et al., 2011](#)). For an example, see [Figure 1.1](#), which is adapted from [Figure 1](#) of that paper; the authors built a model demonstrating how the C/O ratio in giant planet atmospheres would necessarily differ from that of their host star. The [Öberg et al. \(2011\)](#) model uses the canonical solar C/O ratio (0.54), a power-law disk temperature profile ([Andrews and Williams, 2007](#)),

$$T = T_0 \times \left(\frac{r}{1AU}\right)^{-q} \quad T = 200K \times \left(\frac{r}{1AU}\right)^{-0.62} \quad (1.1)$$

and known evaporation temperatures and measured densities of the major compounds (CO, CO₂, H₂O, carbonaceous dust grains, and silicate dust grains) from observations of solar-type protoplanetary disks ([Pontoppidan, 2006](#)) and the ISM ([Draine, 2003](#); [Whittet, 2010](#)). Note the locations of the ice lines – also known as the snow or frost lines, the point at which a given species would condense – for CO, CO₂, and H₂O on the plot and how they impact the C/O ratios of the gas and dust

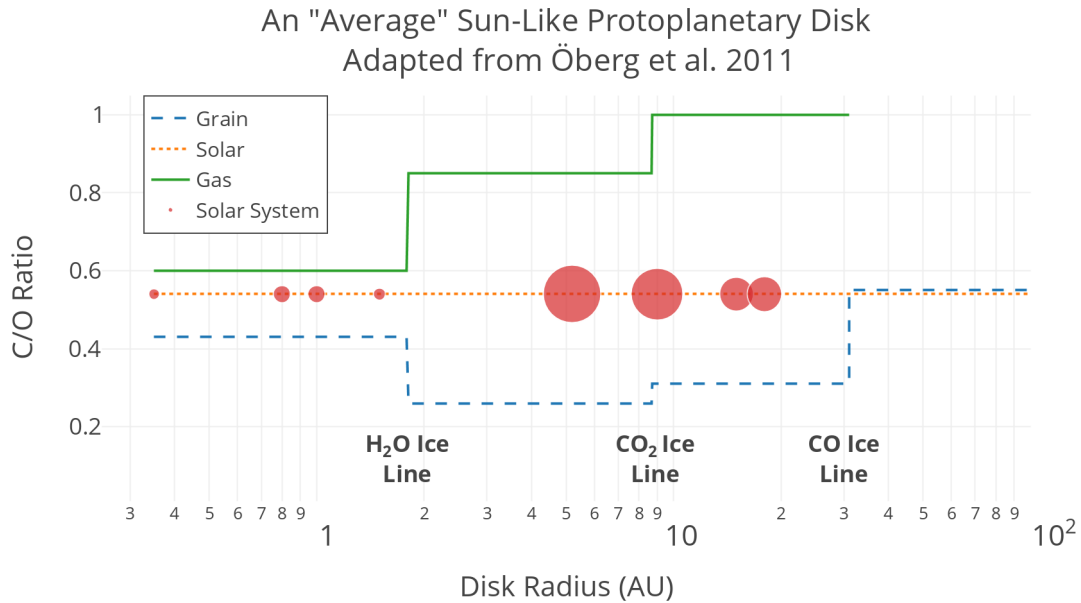


Figure 1.1 The model of the carbon-to-oxygen ratio (C/O) used by Öberg et al. (2011) to show the dependence on formation location by the ultimate gas (solid green line) and grain (dashed blue line) content of giant planet atmospheres. The solar C/O ratio is plotted in the orange, dotted line for reference, and the orange circles are placed at the approximate formation locations of the Solar System planets (on the Solar C/O line just for clarity, not because their C/O values are/were Solar). Neptune and Uranus are placed inward of their current locations per to the predictions of the Nice model (Tsiganis et al. 2005; Levison et al. 2011, others).

grains.

1.1.1 Before Exoplanet Discovery: The Solar System

Consider the architecture we observe in our own Solar System: small, terrestrial (rocky) planets orbit close to the Sun, and large, gaseous/icy giants orbit further away. The boundary between the two planet classes coincides with the water snow/ice line at about 1.8 AU. With only carbonaceous, silicate, and heavier-metal dust grains able to condense inward of the ice line, it follows that the terrestrial planets formed via some type of core accretion mechanism. The relatively low

abundances of metals from the original solar nebula limited the supply of material to accrete, thereby limiting the ultimate size of a planet in the inner solar system to that of Earth. An planetesimal the mass of Earth (or less) would not be massive enough to hold onto, or potentially even to accrete at all, much of the nearby primordial H/He-dominated gas, much of which may have been blown out by the stellar wind, anyway. Instead, the terrestrial planet atmospheres of today comprise heavier elements that were outgassed from the solid core over time (e.g., Earth's atmosphere is primarily molecular nitrogen and oxygen). The giant planets likely formed cores in much the same way, through the agglomeration and collisions of grains, then clumps of solid matter, and increasingly more massive objects. The giant planets were able to grow much larger cores because more solid material – namely ices – would have been available beyond each ice line. Those cores should have grown to at least several Earth masses, or more, enabling the accretion of nearby gases into an envelope that roughly doubled the planets' radii.

Thus, the core accretion mechanism, operating to build rocky, terrestrial planets near the Sun and giant, gaseous/icy Jovians beyond the snow line, goes far to explain the Solar System we observe today. The core accretion model as originally proposed does operate too slowly, and there are a few more nuanced dynamical questions that need further explanation from theories like the Nice Model ([Tsiganis et al., 2005](#); [Levison et al., 2011](#)) or the Grand Tack Hypothesis ([Walsh et al., 2012](#)). Preliminary results from the Juno mission also call into question the presence of a distinct, solid core of Jupiter ([Bolton et al., 2017](#)). However, astronomers and planetary scientists were confident in their broad, general picture of planet formation, and

saw no reason to expect anything radically different when searching for exoplanets around other Sun-like stars.

1.1.2 After Exoplanet Discovery: More Questions than Answers

The “pulsar planets,” two terrestrial planets orbiting PSR 1257 +12, were the first confirmed exoplanet discoveries (Wolszczan and Frail, 1992). Finding planets in orbit around an evolved star like a pulsar was unexpected, certainly, but such systems remain rare and thus invite only an expansion of possibility in specific planet evolution (e.g. Miller and Hamilton 2001), rather than a paradigm shift in general theories of planet formation and evolution around main-sequence stars. A paradigm shift was to come, though: just three years later, Mayor and Queloz (1995) announced the discovery of 51 Pegasus b, the first exoplanet around a main-sequence star, orbiting just 0.052 AU away from a Sun-like (G2) star, with an orbital period of 4.2 days. In the solar system, Mercury, the closest-in planet, orbits in 88 days, at an average distance of 0.4 AU. 51 Peg b is nothing like Mercury, or any of the inner terrestrial planets: the exoplanet is at least half as massive as Jupiter (minimum mass $M_p \sin i = 0.46M_J$) and nearly twice Jupiter’s size (radius $R_p = 1.9R_J$).

while such planet should be thermally stable (Guillot et al., 1996), planet formation models like the Öberg et al. (2011) model of Figure 1.1 do not support the *in situ* formation of such a large planet so close to its host star; there simply isn’t the supply of condensed material to assemble a sufficiently-massive core in the immediate vicinity of the star, where equilibrium temperatures would be well over

1000 K. Instead, astronomers reckon with the hundreds of giant, close-in planets (see Figure 1.2) by invoking orbital migration (Lin et al., 1996). Migration mechanisms involve gravitational torques exerted on young planets by the gas component of the protoplanetary disk, the Kozai effect, and/or gravitational scattering as a result of close encounters between planet(es) (see reviews Lubow and Ida 2010; Kley and Nelson 2012 and references therein).

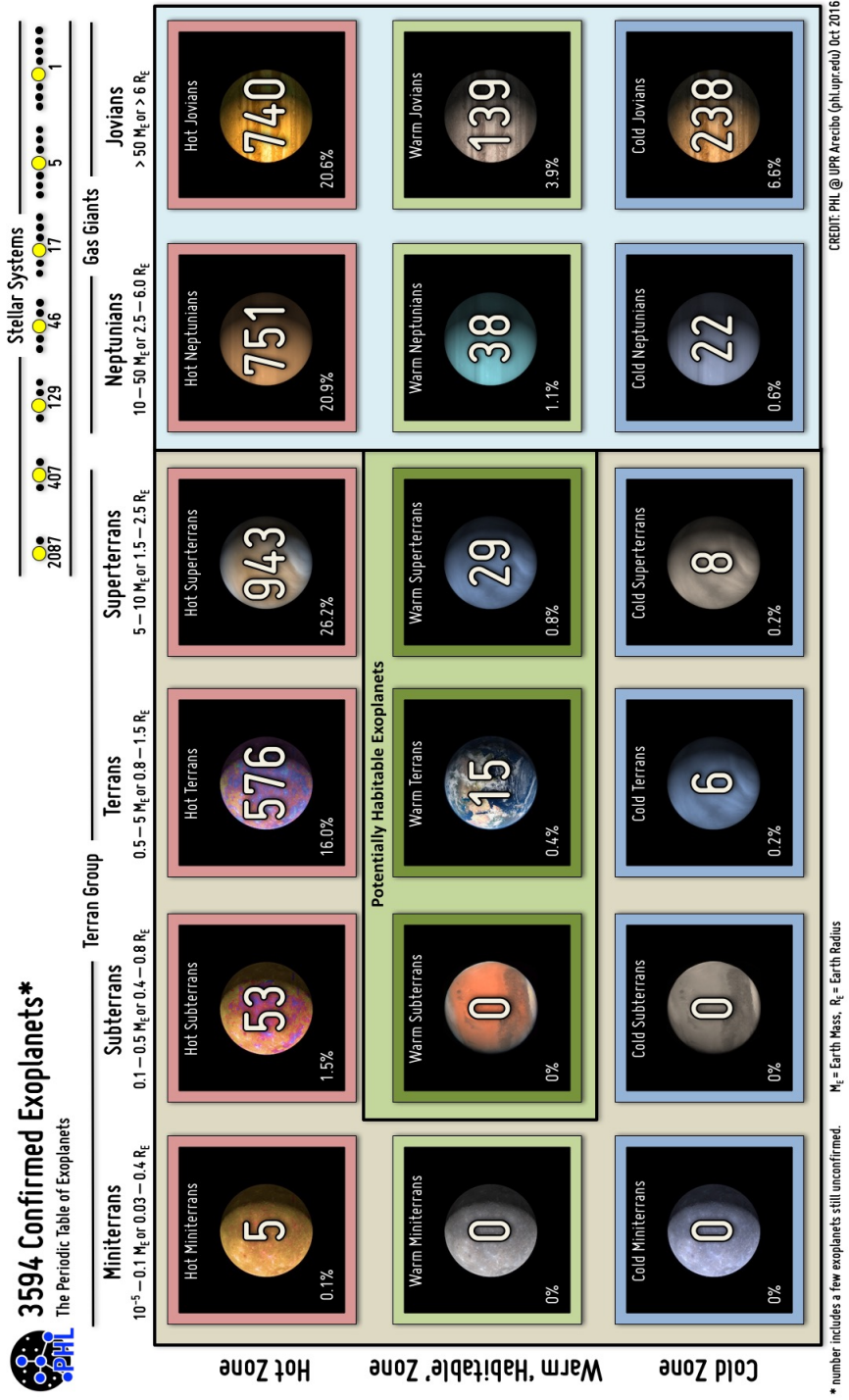


Figure 1.2 From the Planetary Habitability Laboratory at the University of Puerto Rico². Confirmed exoplanets as of October 2016, separated into 18 bins across two dimensions: equilibrium temperature (three bins) and radius (six bins). Note the marked difference between the demographics of known exoplanets versus the Solar System, which is both a selection effect (giant, close-in planets are easier to detect) and an astrophysical one (super-Earths/mini-Neptunes are the most common type of exoplanet).

In addition to challenging our understanding of planet formation and evolution, 51 Peg b represented a boon for exoplanet science: instead of the expected slow start to exoplanet discovery as instrumentation capable of detecting solar-system-like planets, there has been an explosion, with more than 3500 known exoplanets confirmed today. That number is so high in large part because this previously unknown phase space (close-in, giant planets) is far easier to explore for nearly all of the exoplanet discovery methods.

Because planets are generally much smaller and much fainter than their host stars, they can generally only be spatially resolved from their host star and directly imaged when at great orbital distances (and thus large angular separations) and warm (and thus bright) from not-yet-dissipated heat from formation. The most studied planets so far are in the four-planet HR 8799 system (Marois et al., 2008). Coronagraphic technology continues to advance such that direct imaging and direct spectroscopy should become more accessible for a larger population of planets (e.g. Macintosh et al. 2014; Crooke et al. 2016). For now, however, the primary methods for exoplanet discovery require looking for signatures of indirect effects of a planet on its host star, which will be stronger with higher planet mass (the radial velocity method), higher planet-to-star radius ratio (the transit method), and/or smaller semi-major axis (both radial velocity and transit methods). Figure 1.2 shows the size and equilibrium temperature (correlates inversely with planet-star separation) distribution of confirmed exoplanets as of October 2016. Indeed, more than two-thirds of the confirmed exoplanets shown in the figure are close-in and far larger

²<http://phl.upr.edu/projects/habitable-exoplanets-catalog/media/pte>

than the Earth.

As we discover more planets, we are able to account for this bias in the distribution of known exoplanets; the “Hot Jupiters,” as we have come to refer to Jovian-sized planets in orbits shortward of ten days, are over-represented because of their relative ease of detection, but they are in fact relatively rare; see Figure 1.3, wherein a steep drop-off in the occurrence of planets larger than about $2.8 R_{\oplus}$ ($0.25 R_J$), as shown in the [Fressin et al. \(2013\)](#) analysis of *Kepler* results. Further, the most commonly occurring planet size known as a super-Earth or mini-Neptune ($1.3\text{-}3 R_{\oplus}$). Although a recent dynamical study does argue the influence of such a planet in the Kuiper Belt ([Batygin and Brown, 2016](#)), no confirmed super-Earth planet has ever been observed in our own Solar System, and thus the formation and evolution of this common, but missing, link in between ice giants and terrestrial planets has not been a focus of theoretical efforts.

We are left with more questions than answers surrounding planet formation and evolution upon discovery of the incredible diversity of exoplanet system architectures, occurrence rates, and bulk parameters. The various planetary migration mechanisms invoked to explain the biggest surprise – the existence of close-in, giant planets – operate on very short timescales, and are therefore unlikely to be observed actually occurring. Further, the possibility of distinguishing signatures of the two planet formation mechanisms – disk instability and core accretion – in observations of planet-forming disks ([Jang-Condell, 2009](#)) is still tentative, and thus we still seek observational signatures in already-formed exoplanet atmospheres, the gateways to

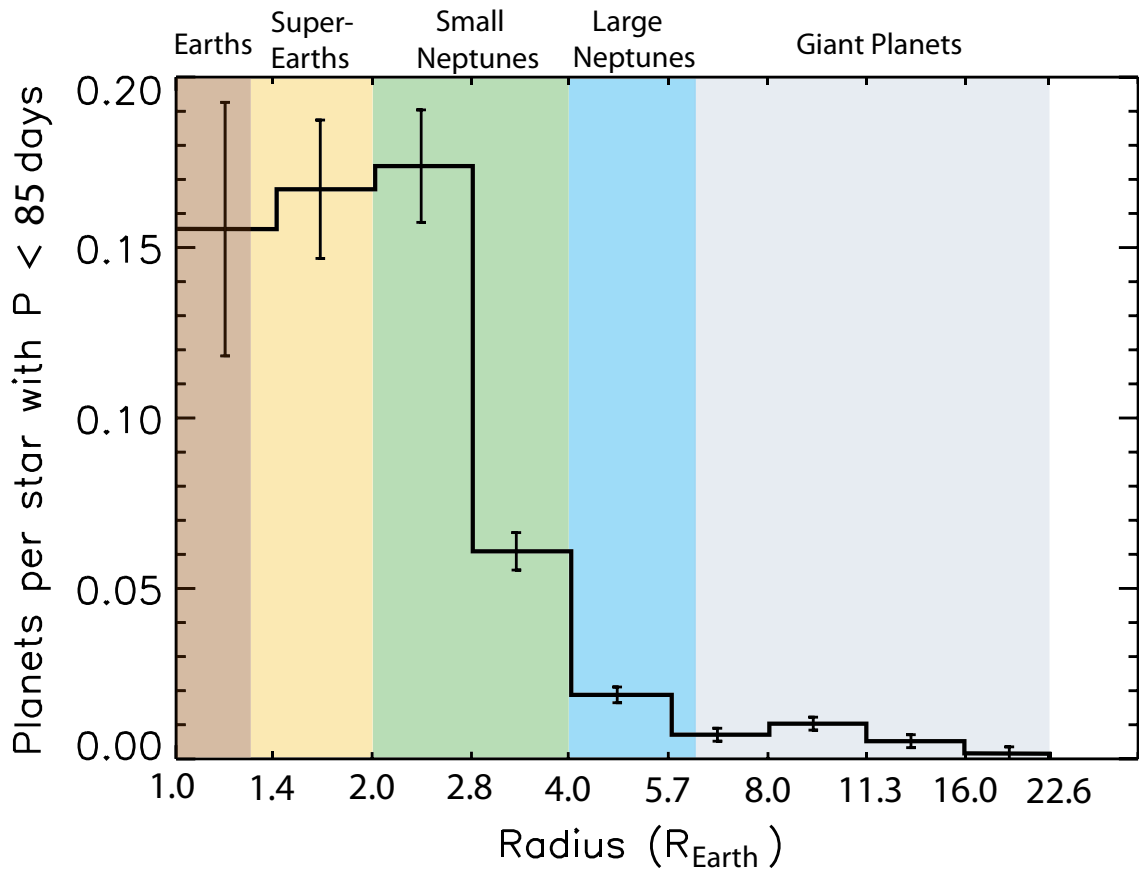


Figure 1.3 From [Fressin et al. \(2013\)](#), Figure 13. The occurrence of planets within 85-day periods by size around FGKM stars, based on the first six quarters of Kepler data and corrected for both false positives and incompleteness. Note that super-Earths/mini-Neptunes are the most common size of planet; even though Hot Jupiters(/Saturns/Neptunes) are frequently found, they are by far the least frequently occurring planet size.

understanding an individual planets' history. Even as it appeared that the community was coming to a consensus for the need for migration to explain close-in giant planets, [Batygin et al. \(2016\)](#) found that an *in situ* formation scenario for at least some Hot Jupiters cannot be ruled out. We must leverage the findings of multiple studies (e.g., [Öberg et al. 2011](#); [Madhusudhan et al. 2014](#); [Brewer et al. 2017](#)) that atmospheric abundances, particularly metallicities and carbon-to-oxygen ratios, are tied to the formation location and mechanism – core accretion or disk instability – of giant exoplanets.

1.2 Characterizing Exoplanets in Extreme Environments

Figure 1.2 hints at the limit of what we can learn about individual exoplanets using discovery techniques. We can extract orbital parameters and some bulk parameters (e.g., mass, radius), and perhaps make predictions about internal structure.

We are hard-pressed even to map what we know about solar system planets onto exoplanets, because the environments of our planets are so different from those of our exoplanet discoveries, even when their bulk parameters are roughly analogous. The challenge increases when a planet's bulk parameters have no solar system analog. For example, WASP-18b, presented in Chapters 2 and 4, is more than ten times the mass of Jupiter, orbiting its F star in just 22 hours ([Hellier et al., 2009](#)).

In a further refinement of occurrence rates based on the Kepler dataset, [Fulton et al. \(2017\)](#) found observational evidence for a theoretically-supported (numerical

studies: [Owen and Wu 2013](#); [Lopez and Fortney 2013](#), analytical study: [Owen and Wu 2017](#)) “evaporation valley,” a marked absence of close-in (orbital period shorter than 100 days) planets around a radius of $1.8 R_{\oplus}$ ($0.16 R_J$), creating a bimodal distribution with distinct peaks at 1.3 and $2.6 R_{\oplus}$ (0.12 and $0.23 R_J$). If it is indeed an *evaporation* valley, the lower-radius peak is populated by evaporated cores of former giant planets, while the higher-radius peak is populated by what they were before, at roughly twice their radius. The “herding” photoevaporation appears to do makes it all the more curious why we have neither an approximately Earth-radius evaporated core nor a twice-Earth-radius close-in giant in our own solar system.

[Thorngren et al. \(2016\)](#) found that close-in, *warm* ($<1000\text{K}$) planets tend to possess higher metallicities than those of their host stars; this agrees with the general trend observed in the Solar System giants (e.g., [Fortney et al. 2007](#)). However, theoretical approaches suffer a degeneracy for hot ($T_{eq} > 1000\text{K}$) planets, because the gaseous envelopes at high irradiation levels are subject to inflation, which puffs up the atmospheres to large radii. Detailed characterization of hotter planets is therefore doubly necessary to understand their metallicities and break the degeneracy caused by

1.2.1 Interactions Between Close-in Planets and their Host Stars

Before we approach the happenings inside of an exoplanet atmosphere, let us first review the interactions the planet (and its atmosphere) have with the host star. The proximity to the host star exposes these hot, giant exoplanets to extremes in

gravity and irradiation, which in turn triggers unexpected phenomena and assembles atmospheres unlike anything we have studied before.

1.2.1.1 Tides

Tides arise from the difference in the strength and direction of the net gravitational force, which operates as an inverse-square law, on various parts of an extended body. Following the derivation of [de Pater and Lissauer \(2010\)](#), we consider two objects: the first is a finite sphere of radius R centered at the origin, and the second is a point source of mass m located at a point \mathbf{r}_0 , such that $|\mathbf{r}_0| = r_0 \gg R$, i.e., the point source m is far enough away to see R as approximately a point source. If R is of finite size, though, R will feel a stronger gravitational pull from m on the side closest to m , and a weaker gravitational pull from m on the side furthest from m , so there's a differential across the sphere, which is known as the tidal force. To see why tides are particularly consequential for close-in planets, we can derive the tidal force, \mathbf{F}_{TIDE} , per unit mass (or “specific” tidal force) of the sphere at some point $\mathbf{r}_1 = (x_1, y_1, z_1)$ would be the difference between the gravitational forces exerted by m at the origin and at point \mathbf{r} , or

$$\mathbf{F}_{\text{TIDE}}(\mathbf{r}_1) = \frac{G m}{r_0^3} \mathbf{r}_0 - \frac{G m}{|\mathbf{r}_0 - \mathbf{r}_1|^3} (\mathbf{r}_0 - \mathbf{r}_1) \quad (1.2)$$

If we think of m as a planet a distance r_0 away along the equatorial plane from the center of a star, we can simplify the geometry such that m is on the x-axis and also only consider the tidal force at points along the x-axis. In that case, $|\mathbf{r}_0| = x_0$

and $|\mathbf{x}_1| \Rightarrow x_1$, and the tidal force becomes

$$\mathbf{F}_{\text{TIDE}}(x_1) = \frac{G m}{x_0^2} - \frac{G m}{(x_0 - x_1)^2}, \quad (1.3)$$

which can be estimated via a Taylor expansion as

$$\mathbf{F}_{\text{TIDE}}(x_1) \approx \frac{2x_1 G m}{x_0^3}. \quad (1.4)$$

The magnitude of the tidal force scales linearly with distance from the center of the sphere and as the inverse *cube* of the separation, so tides can be incredibly consequential for close-in exoplanets. We know, of course, that the Moon raises discernible tides on the Earth, so how does the tidal force felt on the surface of the Earth from the Moon ($m = M_{\text{moon}}$, $x_1 = R_{\oplus}$, $x_0 = \text{Earth} - \text{Moondistance}$) compare to the WASP-18 system studied in Chapter 4 ($m = 10.27 M_J$, $x_1 = 1.26 R_{\odot}$, $x_0 = 0.02034 \text{ AU}$)? The WASP-18b tidal force is nearly five orders of magnitude stronger per unit mass ($\sim 8.6 \times 10^4$).

Significant tidal forces can distort (as seen with Earth’s oceans) or even disrupt (as seen with Comet Shoemaker-Levy, [Asphaug and Benz 1994](#)) planetary and stellar bodies. The most important, broadly-applicable outcome of the strong tidal forces in close-in orbits is tidal locking, the synchronization of the planets’ orbital periods with their rotation periods, resulting in one side of the planet always facing the host star (the “day side”), and one side always facing away in darkness (the “night side”), as is the case with the Earth’s Moon. For the analysis in this thesis, I assume all of the planets are tidally locked.

1.2.1.2 Mass Loss

The incredibly high levels of X-ray and extreme-ultraviolet (XUV) irradiation very close to the central star can drive photoevaporation and hydrodynamic mass loss on planets in small orbits. Though [Guillot et al. \(1996\)](#) concluded that Hot Jupiters like 51 Peg b should generally be stable against thermal or hydrodynamic mass loss, active mass loss has been observed in multiple systems since (e.g., [Vidal-Madjar et al. 2003](#); [Ehrenreich and Désert 2011](#)). Atmospheric mass loss occurs when the mean thermal velocity ($v_{th} = \sqrt{2KT/m}$) of the atoms and/or molecules in an atmosphere exceeds the escape velocity (v_{esc}) of the planet. The ratio of the squares of these two velocities is known as the Jeans escape parameter, λ , where, in the case of hydrostatic equilibrium,

$$\lambda \equiv \left(\frac{v_{esc}}{v_{th}} \right)^2 = \frac{GM_p m}{k_B T r}. \quad (1.5)$$

for a particle of mass m and temperature T at some radial distance, r , from the center of a planet of mass M_p . [Fossati et al. \(2017\)](#) define the restricted Jeans escape parameter, Λ , as an estimate of λ in the case of a hydrogen-dominated atmosphere ($m \rightarrow m_H$) in the outer atmosphere of a planet ($r \rightarrow R_p, T \rightarrow T_{eq}$),

$$\Lambda \equiv \frac{GM_p m_H}{k_B T_{eq} R_p}. \quad (1.6)$$

The authors find that a planet with $\Lambda \lesssim 20 - 30$ should be experiencing very high mass-loss rates. [Cubillos et al. \(2017a\)](#) calculate Λ and estimate envelope fractions for exoplanets with measurements of both mass and radius and mass less than twice that of Neptune. They find that a large subset of Neptunes have measured bulk

parameters consistent with both the retention of the primordial H/He-dominated atmosphere *and* a very high H/He mass loss rate, which cannot be simultaneously true for more than a tiny fraction of a planets' lifetime. The authors assert that there is likely some kind of systematic error in our measurement of one or more planetary parameters (e.g., an underestimation of mass or over-estimation of radius) or assumptions (e.g., hot/warm Neptunes could have systematically higher albedos than hot/warm Jupiters), motivating further detailed study of hot/warm Neptunes.

1.2.1.3 Radius Inflation

Examining Figure 1.5, we can observe a clear break in the correlation between mass and radius above approximately $0.5M_J$. At that point, the planets with higher equilibrium temperatures, a proxy for incident flux, have systematically higher radii that are well above theoretical predictions; this phenomenon was quantified by [Weiss et al. \(2013\)](#) into a set of relations defining two fundamental planes in planetary radius, planetary mass, and incident flux. CoRoT-2b, the focus of Chapter 3, is a highly inflated planet. The true cause of radius inflation is still not clear; [Fortney and Nettelmann \(2010\)](#); [Baraffe et al. \(2014\)](#) review the many mechanisms that have been suggested, but there is no clear answer, adding yet another layer of degeneracy to attempts to model atmospheres of such planets. [Miller and Fortney \(2011\)](#); [Demory and Seager \(2011\)](#) were able to identify a critical threshold: below an incident flux of $\sim 2 \times 10^8 \text{ erg s}^{-1} \text{ cm}^{-2}$ ($T_{eq} \lesssim 1000 \text{ K}$), radius inflation is not observed. HATS-7b, the subject of Chapter 5 of this thesis, sits just above this

threshold, with an equilibrium temperature estimate of 1065 K.

1.2.2 Spectroscopy of Transiting Exoplanets

Transiting exoplanets are those whose orbital planes align with our line of sight, such that they will pass directly between us and their host star once per orbit, briefly dimming the light of the host star by a small fraction. In addition, the total light from the exoplanet-star system will also dim slightly when the planet disappears behind the host star once per orbit. The geometry is illustrated in Figure 1.4; we call the passage of the planet in front of the star, between the observer and the star, the (*primary*) *transit*, and the passage of the planet behind the star, the (*secondary*) *eclipse* or *occultation*. Because the orientation of a planetary system relative to an observer at Earth is completely random, we can precisely calculate the likelihood, $p_{\text{transiting}}$ of a planet of radius R_p in an orbit with eccentricity e and semi-major axis a is to transit or be eclipse by a star of radius R_{star} such that an observer at celestial longitude ω could observe it (Winn, 2010):

$$p_{\text{transiting}} = \begin{cases} \left(\frac{R_{\text{star}} \pm R_p}{a} \right) \left(\frac{1+e \sin \omega}{1-e^2} \right), & \text{primary transit} \\ \left(\frac{R_{\text{star}} \pm R_p}{a} \right) \left(\frac{1-e \sin \omega}{1-e^2} \right), & \text{eclipse} \end{cases}$$

which, in the limiting case of a small planet ($R_p \ll R_{\text{star}}$) orbiting in a circular orbit ($e = 0$), reduces to

$$p_{\text{transiting}} = \frac{R_{\text{star}}}{a} \tag{1.7}$$

The likelihood of a planet in an Earth-like orbit ($a = 1 AU$) around a Sun-like star ($R_{star} = 1 R_{\odot}$) is about 0.5%, but the likelihood of a Hot Jupiter ($a = 0.02 AU$) orbiting the same star is 23%. Transiting planets make up the largest population of confirmed planets to date, primarily due to the *Kepler* mission (Borucki et al., 2010), which monitored 156,000 stars continuously for nearly four years seeking those characteristic dips in the stellar light indicating the presence of planets.

Charbonneau et al. (2000) reported the first observation of an exoplanet transiting its host star, finding that the known exoplanet HD 209458b, initially discovered by a radial velocity survey, causes a 1.41% decrease in the light coming from the Sun-like ($1.1 R_{\odot}$, $1.1 M_{\odot}$) star it orbits. Just ten years later, *Kepler* harnessed the transit method as a powerful tool for the discovery of exoplanets, having confirmed 2,335 new planets as of July 2017, fully two-thirds of the total number known. *K2*, the follow-up mission to *Kepler*, searching the ecliptic plane for planets after the failure of two reaction wheels (Howell et al., 2014), has added another 146 so far. The application of the transit method reaches far beyond discovery, however; it is also a powerful tool for the *characterization* of exoplanets, i.e., the observation of individual, known planets in ways that divulge far more information beyond bulk and/or orbital parameters derived from discovery.

Transit spectroscopy is simple in concept, but quickly becomes more complex in execution: observations need only disperse the light received from a star before, during, and after primary transit (and/or secondary eclipse), and use the changing transit (or secondary eclipse) depth as a function of wavelength to derive insights on the nature and composition of the planet's atmospheres. Such variations in the

transit depth are small, and only the best instruments available can even begin to tease out the signal of a planet’s atmosphere from the starlight. The primary workhorses in transit spectroscopy have been the *Hubble Space Telescope (HST)* (e.g., [Charbonneau et al. 2002](#); [Sing et al. 2011](#); [Berta et al. 2012](#); [Kreidberg et al. 2014](#); [Fraine et al. 2014](#); [Wakeford et al. 2017b](#)) and *Spitzer* (e.g. [Grillmair et al. 2007](#); [Knutson et al. 2008](#); [Désert et al. 2011](#); [Todorov et al. 2013](#)).

From the ground, broad-band spectrophotometry has found some successes, though true spectroscopy is more challenging, as it requires simultaneously obtaining the spectrum of a reference star (of similar brightness and spectral type to the exoplanet host star) to account for atmospheric and instrumental fluctuations over time, which necessitates using a multi-object spectrograph (e.g., [Bean et al. 2013](#); [Huitson et al. 2017](#)).

However, direct (not time-series) ground-based spectroscopy can measure both transmission and emission spectra using high-resolution ($\lambda/\Delta\lambda \gtrsim \text{few} \times 10^4$) observations to distinguish Doppler-shifted exoplanetary spectral lines from stationary stellar and telluric lines (e.g. [Redfield et al. 2008](#); [Snellen et al. 2010a](#); [Birkby et al. 2013](#); [Brogi et al. 2016](#)).

At $2.7 R_{\oplus}$ and $6.4 M_{\oplus}$, GJ 1214b ([Charbonneau et al., 2009](#)) was the first planet in the super-Earth/mini-Neptune phase space to be characterized via transit spectroscopy ([Bean et al., 2010](#); [Désert et al., 2011](#); [Bean et al., 2011](#); [Berta et al., 2012](#); [Kreidberg et al., 2014](#)). GJ 1214b has come to define an archetype, sitting at the center of the continued super-Earth-versus-mini-Neptune debate. Early observations attempted to break the degeneracy between two scenarios: a mini-Neptune

with a solid rocky or icy interior and a low-mean-molecular-weight, hydrogen- and helium-dominated atmosphere, or a “water world” with a mostly water-ice and fluid interior and a steam atmosphere. High-precision transmission spectra with HST [Berta et al. \(2012\)](#); [Kreidberg et al. \(2014\)](#) showed that the planet is enshrouded by an aerosol-dominated atmosphere.

1.2.2.1 Transmission (Transit) Spectroscopy

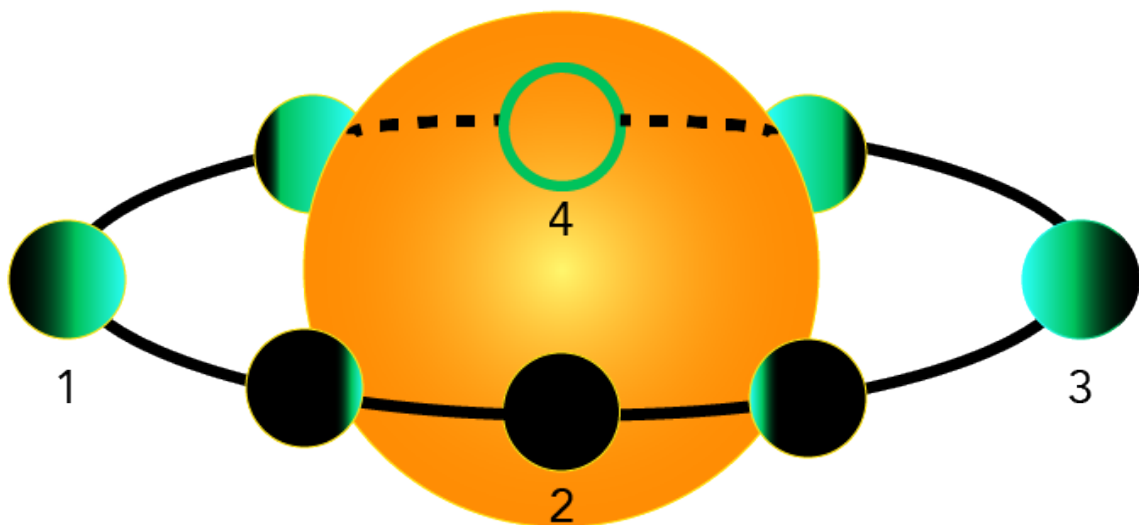
The nominal maximum decrease in light measured from a star of radius R_{star} and disk-averaged intensity I_{star} being transited by a planet of radius R_p and night-side, disk-averaged intensity $I_{p,night}$ is

$$\text{Transit Depth} = \left(\frac{R_p}{R_{star}} \right)^2 \left[1 - \frac{I_{p,night}}{I_{star}} \right] \quad (1.8)$$

known as the transit depth ([Winn, 2010](#)). For tidally-locked planets, as most close-in planets and all planets studied in this thesis are assumed to be, the night-side of the planet is permanently dark, ensuring $I_{p,night} \ll I_{star}$, reducing the transit depth to simply the square of the planet-to-star radius ratio. However, the depth, and therefore the apparent radius, of a transiting planet can vary with wavelength. If a transiting exoplanet has a gaseous envelope – i.e., an atmosphere – the starlight will be filtered through the outermost layers of that atmosphere as the planet passes in front of it; a side view of a transit is shown in [Figure 1.6](#). The filtered starlight

³Data from the [NASA Exoplanet Archive](#), which is operated by the California Institute of Technology, under contract with NASA under the Exoplanet Exploration Program

Secondary Eclipse



Primary Transit

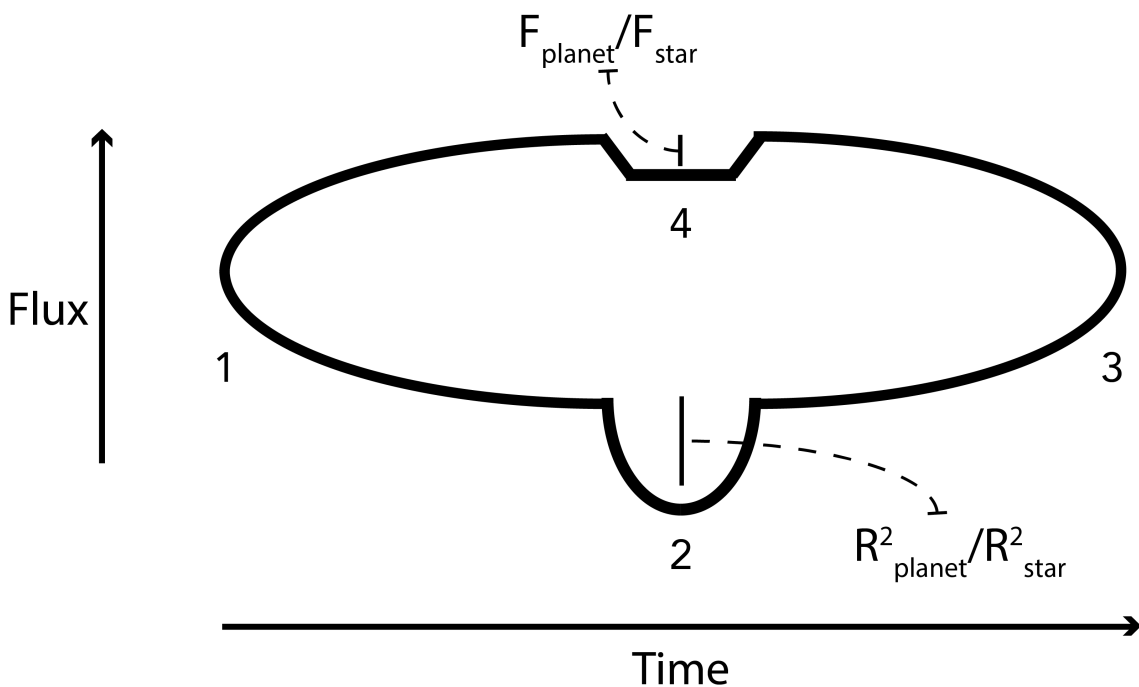


Figure 1.4 Schematic of the phases of a close-in transiting exoplanet aligned with the observer's line of sight. Planets close to their host stars will likely have circularized and become tidally locked, such that one side of the planet is permanently facing the star.

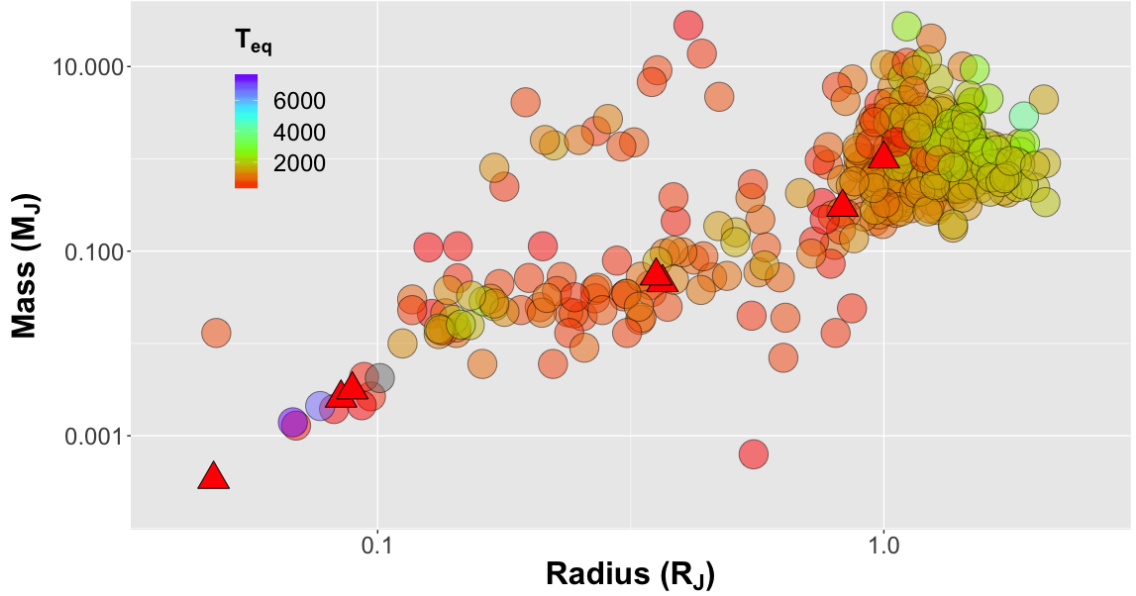


Figure 1.5 A mass-radius diagram of confirmed exoplanets for which both parameters are known, as of July 25, 2017³, colored by their equilibrium temperatures (see Equation 1.17). Seven solar system planets (all but Mercury) are overplotted as red triangles for reference (note that Earth and Neptune cover most of Venus and Uranus, respectively).

modulates the stellar spectrum during transit at the wavelengths of gaseous atmospheric constituents, producing absorption lines that can provide valuable insight into the chemical abundances and structure of the atmosphere (Seager and Sasselov, 2000). A transmission spectrum is therefore a measure of the transit depth, i.e., the planet’s apparent radius, against wavelength. The change in transit depth $\delta_{transitdepth}$ due to absorption by the exoplanet atmosphere should be a small multiple (usually estimated as 5) of the ratio of the area of the atmospheric annulus one pressure scale height (H_0 (see § 1.3.4) deep to the stellar disk area, or (Brown, 2001;

Encrenaz, 2014):

$$\begin{aligned}
 \delta_{\text{transit depth}} &= \left(\frac{\delta F}{F}\right)_1 - \left(\frac{\delta F}{F}\right)_2 \\
 &\approx \ln\left(\frac{\sigma_2}{\sigma_1}\right) \times \left(\frac{\delta A}{A}\right)_{\text{Atmosphere}} \\
 &\approx 5 \times \frac{2 \pi R_p H_0}{\pi R_{star}^2} = \frac{2 R_p H_0}{R_{star}^2}
 \end{aligned}
 \tag{1.9}$$

While we suspect that many small, close-in exoplanets would not have retained any atmosphere they may have had, or are bare, evaporated cores of gaseous planets, we do expect that larger planets, potentially from super-Earths/mini-Neptunes upward, based on their bulk densities must have some kind of atmosphere. The modulations are small, however; for a hypothetical hot Jupiter with a hydrogen/helium-dominated envelope, temperature of 1000K, radius of $1 R_J$, and orbiting a $1 M_\odot$ star, we would expect a $\delta_{\text{transitdepth}}$ of 5×10^{-4} , or 500 parts-per-million (ppm). We do not know how those atmospheres are differentiated, though, and we do not know either how the primordial atmospheres were constituted or how they might have evolved during whatever migration process might have brought the planet inward, or how the harsh irradiation environment would affect the atmospheric chemistry.

1.2.2.2 Emission (Eclipse) Spectroscopy

Emission spectroscopy, like transit spectroscopy, requires the orbital geometry of an exoplanet-star system to align with the observer’s line of sight so that the planet disappears behind its host star every orbit. If the exoplanet’s orbit is circular ($e = 0$), then any planet that transits would also eclipse. Analogously to transit spectroscopy, an eclipse spectrum is calculated by measuring the depth of the eclipse as a function

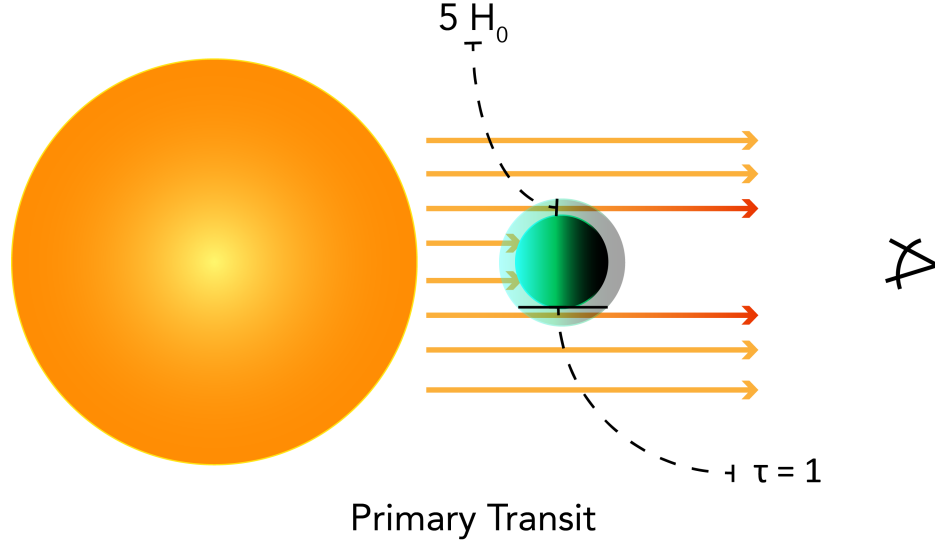


Figure 1.6 A side view of observing an exoplanet in transmission. Most of the planet is opaque to the starlight, but some starlight will get filtered through the limb, or the diffuse outer layers of the atmosphere, to a chord of optical depth $\tau = 1$. This leaves imprints of the atmosphere on the stellar spectrum as the atmospheric constituents absorb some of the starlight. The depth of the atmosphere through which the starlight penetrates should be approximately five scale heights (see § 1.3.4)

of wavelength. Unlike transit spectroscopy, however, an eclipse spectrum is not indirect detection of atmospheric signatures, but a direct measurement of the light coming from the planet, which is a combination of stellar light that has been from the planet and the thermal emission or heat coming directly from the planet. The nominal maximum decrease in light measured from a star of radius R_{star} and disk-averaged intensity I_{star} when a planet of radius R_p and day-side, disk-averaged intensity $I_{p,day}$ disappears behind it is (Winn, 2010)

$$\text{Secondary Eclipse Depth} = \left(\frac{R_p}{R_{star}} \right)^2 \frac{I_{p,day}}{I_{star}}. \quad (1.10)$$

The reflection and emission spectra of a planet are, to zeroth order, blackbodies peaking typically in optical and (near-)infrared wavelengths, respectively, depending on the temperature and albedo of the planet and the temperature of the star. An

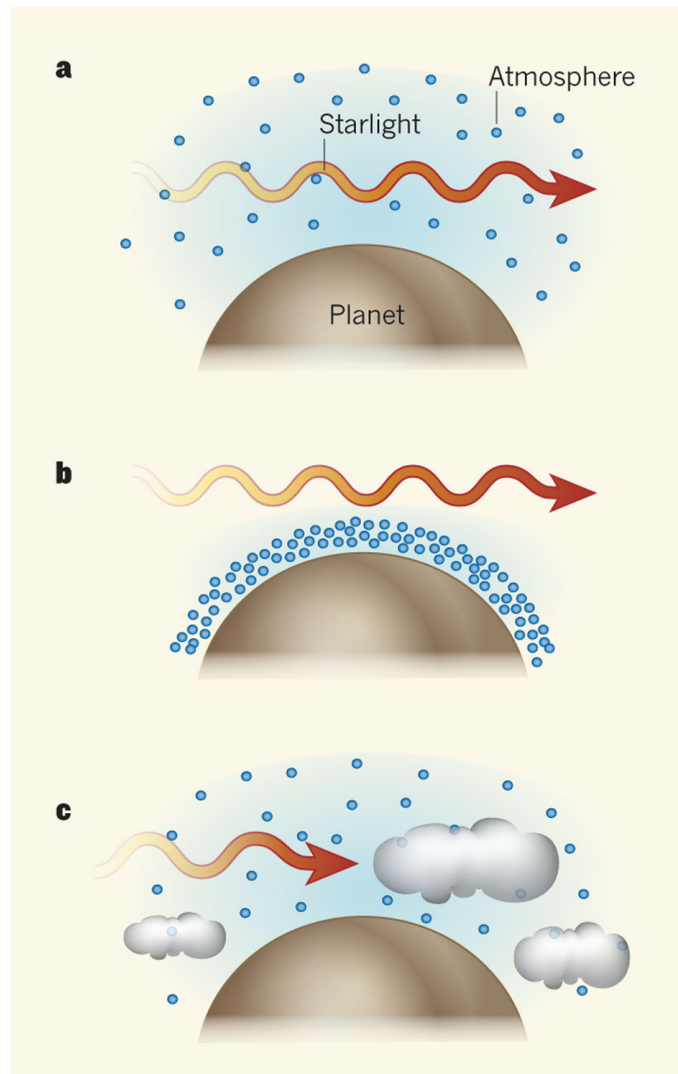


Figure 1.7 From [Deming \(2010\)](#), this schematic shows three scenarios if you were to zoom in on the planet of Figure 1.6. Scenario (a) depicts a clear atmosphere of a large scale height, i.e. large and dominated by mostly H/He, with most of the hydrogen in water vapor. Starlight passing through this gas would get absorbed at the wavelengths of various water transitions, varying the resulting observed spectrum. Scenario (b) depicts a clear atmosphere of a small scale height, i.e. condensed and dominated by heavier elements. Much less of the starlight would pass through this atmosphere, so the observed spectrum would not show any imprint of the atmosphere. Scenario (c) depicts a high-scale-height atmosphere as in (a), but the starlight entering the atmosphere is blocked from leaving it by high-altitude condensates, either clouds or hazes, preventing any modified starlight from traveling to the observer. The spectrum from (c) would therefore be qualitatively similar to one from (b), presenting a degeneracy in possible interpretations of flat transmission spectra.

emission spectrum, therefore, can yield insight into the energy budget of a planet and, when observed at more than one wavelength, can reveal the albedo (reflectance) of a planet. While the depth of the transit scales as the square of the planet-to-star radius ratio, the depth of the eclipse scales as the planet-to-star flux ratio; the strongest eclipses are observed when the stellar flux is low relative to the planetary flux, like in the mid-infrared, particularly for very hot stars, whose spectra peak in the visible/UV, which heat up close-in planets to temperatures that peak in the near- or mid-infrared. It is therefore unsurprising that the first secondary eclipse spectra were observed with the Spitzer MIPS instrument at $24\mu\text{m}$, of a Hot Jupiter (orbital period 3.5 days, brightness temperature 1150K) around a 6000K-star (HD 209458b, [Deming et al. 2005](#); [Charbonneau et al. 2005](#); since then, secondary eclipse spectra have been observed with both cryogenic and warm Spitzer (e.g., [Richardson et al. 2007](#); [Knutson et al. 2008](#); [Swain et al. 2008](#); [Deming et al. 2011](#); [Todorov et al. 2014](#) HST (e.g. [Wilkins et al. 2014](#); [Stevenson et al. 2014](#); [Line et al. 2016](#); [Beatty et al. 2016](#), and ground-based observatories (e.g., [Knutson et al. 2010](#); [Zhou et al. 2015](#)), and, further, eclipse mapping (e.g., [Knutson et al. 2007](#); [Majeau et al. 2012](#)).

1.3 Modeling Exoplanet Atmospheres

In this final section, I highlight some of the most relevant inputs and considerations when modeling the transmission and emission spectra from exoplanet atmospheres. Far more information exists than could possibly go here, both in re-

views (Crossfield, 2015; Madhusudhan et al., 2016; Deming and Seager, 2017; Heng and Marley, 2017) and textbooks (Seager, 2010; Heng, 2017).

1.3.1 Radiative Transfer in an Exoplanet Atmosphere

We begin as Heng and Marley (2017) do, and follow their formalism: we will define optical depth, τ , which corresponds to the number of mean free paths (*mfp*) in a medium (i.e., the average number of interactions a photon would have before being absorbed when passing through the medium) in three different ways:

$$\tau \equiv \int n\sigma dx = \int \kappa d\tilde{m} = \int \alpha_e dx, \quad (1.11)$$

where n is the number density of the medium, σ is the absorption cross-section, x is the spatial coordinate, κ is the opacity of the medium (cross-section per unit mass), \tilde{m} is the column mass (mass per unit area), and α_e is the extinction coefficient ($= 1/mfp$). σ , κ , and α_e are all wavelength-dependent parameters, making τ wavelength-dependent as well. When observing a planet in transmission, photons traveling from the star will typically make it out of the planet’s atmosphere above a chord corresponding to $\tau \approx 1$ (see Figure 1.6; because τ varies with wavelength, the radius to which the chord corresponds (the “transit radius”) and, in turn, the transit depth, will also vary with wavelength in the presence of an atmosphere. Similarly, photons coming directly from the planet’s atmosphere can originate from no deeper than $\tau \sim 1$, so the emission spectrum comprises only photons from above $\tau \sim 1$ (the photosphere), which is typically deeper than the transit radius.

Next, we will take an abbreviated look at the radiative transfer equation,

which begins as a simple differential equation balancing the sources of energy in a medium. If we take that deceptively simple equation and apply the plane-parallel approximation, which allows the atmosphere to be sliced into layers that can each be treated one-by-one as axially symmetric and at a constant density, pressure, and temperature, it becomes

$$I_\nu(\hat{k}, \tau_\nu) = I_\nu(\hat{k}, 0)e^{-\tau_\nu} + \int_0^{\tau_\nu} S_\nu(\hat{k}, \tau'_\nu)e^{-\tau'_\nu} d\tau'_\nu \quad (1.12)$$

where I_ν is the emitted intensity as a function of opacity, optical depth, and frequency, and S_ν is the source function.

In local thermodynamic equilibrium (LTE), the source function becomes

$$S_\nu = (1 - A_\nu)B_\nu(T) + A_\nu\Phi, \quad (1.13)$$

where Φ is a function describing scattering.

$$I_\nu = B_\nu(T)(1 - e^{-\tau_\nu}) \quad (1.14)$$

In transmission spectroscopy, where there is no scatter or emission to worry about ($S_\nu = 0$), the emergent intensity is

$$I_\nu(0)e^{-\tau_\nu}. \quad (1.15)$$

While in thermal emission, where the scatter terms can again be dropped, Kirchoff's Law (source function \rightarrow Planck function, $B_\nu(T)$),

$$I_\nu = I_\nu(0)e^{-\tau_\nu} + B_\nu(T)(1 - e^{-\tau_\nu}). \quad (1.16)$$

These are the equations that govern the model atmospheres, layer by layer.

1.3.2 Temperature and Pressure Structure

Our first approximation of the expected temperature of an exoplanet is to calculate its equilibrium temperature, T_{eq} , which is the temperature the planet would have if it were in complete equilibrium with the blackbody radiation emitted from the central star; i.e. had an isothermal surface and no internal sources of heating or cooling:

$$T_{eq} = T_{eff,*} \sqrt{\frac{R_*}{a}} (f'(1 - A_B))^{1/4}, \quad (1.17)$$

where $T_{eff,*}$ is the effective stellar temperature, R_* is the stellar radius, a is the semi-major axis (average planet-star separation), and A_B is the Bond albedo. f' is a correction factor accounting for the fraction of the atmosphere we are observing and/or the efficiency of heat redistribution on the planet (Seager, 2010), recalling that all – or most – close-in planets are going to be tidally locked, with one side of the planet permanently faced toward its host star, and one side permanently left "dark." f' can range from 2/3 (no redistribution of heat) to 1/2 (full redistribution of heat) (Evans et al., 2013).

In modeling transmission spectra, we assume an isothermal temperature gradient with height in the atmosphere (i.e., constant T); in transmission, we are simply measuring absorption, not continuum, and are therefore not very sensitive to temperature gradients, just the absolute temperature, which is typically left as a free

parameter. In emission spectroscopy, the temperature structure must be left as a free parameter, which significantly increases the complexity of models. Retrieval methods that parametrize the temperature-pressure profile significantly reduce the computation time over generating a forward model from the equation of radiative transfer ([Madhusudhan and Seager 2009](#), for a review: [Line et al. 2013b](#)).

1.3.3 Chemistry and Line Opacities

In (exo)planet atmospheres, the densities are high enough to assume LTE conditions when building a model layer-by-layer; collisions dominate over radiation in the transfer of energy, maintaining thermal equilibrium locally, with no net loss or gain of energy, and largely blackbody behavior. In addition, a closed system is in chemical equilibrium when the bulk number densities of all atoms and molecules remain constant over time; various chemical reactions still occur, but they are generally all reversible, and the forward and reverse reactions (or reaction chains) have the same reaction rates. A closed system wants to be in chemical equilibrium, and thus generally reaches it, given enough time, as disequilibrium processes eventually run out of reactants. In planetary (and stellar) atmospheres, deeper layers are more likely to be in chemical equilibrium, because the higher temperatures speed up the reaction times, and those layers will reach equilibrium more quickly. One relevant example is seen in the observed abundances of CO (carbon monoxide) relative to CH₄ (methane) in the upper atmospheres of Jupiter and T-type brown dwarfs. Deep in the atmospheres of Jupiter and T-dwarfs, CO is the more abundant carbon-bearing

molecule, because its triple bond gives it a high enough binding energy to withstand the higher temperatures, whereas the more weakly-bonded CH_4 dissociates. In the cooler upper layers, CH_4 is the more dominant carbon sink instead. Observations, however, show that CO is far more abundant in the upper layers of Jupiter and T-dwarf atmospheres than chemical equilibrium predicts. This is because the system is not, in fact, closed: vertical mixing dredges some of the abundant CO deep in the atmosphere upward, and, while CO does tend to react with molecular hydrogen to produce CH_4 and H_2O via



which, also because of CO's strong triple bond, moves more slowly going forward (to the right) than in reverse (to the left). Therefore, CO gets replenished by vertical mixing faster than it can be replaced by converting to CH_4 , hence an overabundance. Similarly unexpected CO/ CH_4 over/under-abundances were measured in the atmosphere of hot Neptune GJ 436b ([Stevenson et al., 2010](#)), which could be a consequence of CO delivery via vertical mixing driven by the strong stellar radiation onto the day side of the hot Neptune. In most cases, however, it is reasonable to assume chemical equilibrium, because there are few circumstances in which our observations would be sensitive enough to see disequilibrium chemistry, although also see §1.3.5.

Given a list of molecules in chemical equilibrium, the next step in calculating a model spectrum would be to calculate the strength of any and all possible lines coming from those molecules in a set of given conditions. As line lists can approach

millions for hot giant exoplanet temperatures, this is a significant undertaking that need not be repeated each time a new model is generated. Modelers instead make use of line lists; the current preferred list is HITRAN [Richard et al. \(2012\)](#).

What is the line strength, though? Following the notation and derivations of the HITRAN team in [Šimečková et al. \(2006\)](#), first recall that the optical depth can be expressed as a spatial integral of the opacity (equation 1.11). The opacity, κ , of a single spectral line, integrated over all wavenumbers ($\tilde{\nu}$, not to be confused with ν of frequency) is the integrated line strength:

$$\mathcal{S} \equiv \int \kappa d\tilde{\nu} \quad (1.19)$$

When considering a pair of quantum energy levels in a molecule, the relation between the rates of absorption and emission is called *detailed balance*, and depends on the Einstein A- and B-coefficients, which are the rates of spontaneous and induced, respectively, emission or absorption, and are related by

$$g_1 B_{12} = g_2 B_{21}, \quad (1.20)$$

$$A_{21} = 8\pi h\tilde{\nu}^3 B_{21}, \quad (1.21)$$

where the subscripts refer to energy levels 1 and 2 (often denoted generally as m and n), g_1 and g_2 are the statistical weights of the respective levels. Using the detailed balance and radiative transfer equations with the definition of \mathcal{S} , we reach a definition of integrated line strength at a wavenumber $\tilde{\nu}$ of:

$$\mathcal{S}(T) = \frac{g_2}{Q_{tot}(T)} \frac{A_{21}}{8\pi c\tilde{\nu}_0^2} e^{-c_2 E_1/T} (1 - e^{-c_2 \tilde{\nu}_0/T}), \quad (1.22)$$

where T is the temperature, $Q_{tot}(T)$ is the total internal partition function of the molecule at T , $\tilde{\nu}_0$ is the central wavenumber of the line, E_2 is the energy level of line 2, defined such that $E_2 - E_1 = \tilde{\nu}$, c_2 is the second radiation constant, hc/k_b , and c is the speed of light, h is the Planck constant.

In this thesis, we make use of an internal radiative transfer code (Deming et al., 2013) to model CoRoT-2b, and Exo-Transmit (Kempton et al., 2017) for modeling transmission spectra of all of the other planets. Exo-Transmit is open-source and fast. The code uses the HITRAN line lists, assumes an isothermal temperature-pressure profile, and allows for a wide range of input temperatures, metallicities, and C/O ratios, as well as (uniform, grey) clouds at any depth and enhanced Rayleigh scattering (by a simple scale factor). Chapter 5 discusses the application of Exo-Transmit to modeling transmission spectra in more depth.

1.3.4 Scale Height

We can derive the pressure scale height by following the method described in Seager (2010), starting from assuming hydrostatic equilibrium. The pressure (P) gradient with respect to height in the atmosphere (z) is

$$\frac{dP}{dz} = -g\rho \quad (1.23)$$

where g is the gravitational acceleration and ρ is the density. Combining this equation with the ideal gas law,

$$P = nkT = \frac{\rho kT}{\mu_m m_H} \quad (1.24)$$

where n is the number density, k is the Boltzmann constant, μ_m is the mean molecular weight, and m_H is the mass of hydrogen. Rearranging equation 1.24 to isolate ρ ,

$$\rho = \frac{P\mu_m m_H}{kT}, \quad (1.25)$$

substituting it in to equation 1.23, and rearranging finds the differential equation

$$\frac{dP}{P} = -\frac{\mu_m m_H g}{kT} dz \quad (1.26)$$

which, with the nontrivial assumption that temperature (T) and mean molecular weight (μ_m) are constant with height (z) integrates to

$$P = P_0 e^{-z/H_0} \quad (1.27)$$

where H_0 , the pressure scale height, is defined as

$$H_0 \equiv \frac{kT}{\mu_m m_H g} \quad (1.28)$$

and represents the e-folding distance for pressure in the (isothermal, constant mean-molecular-weight) planet's atmosphere. At the wavelengths of a strong molecular or atomic transition, the transit depth deepens (as compared to the white-light or continuum transit depth) by a few scale heights, as the absorption of stellar light at those wavelengths causes the planet to appear larger (recall that the transit depth is dependent on the square of the planet's radius).

1.3.5 Aerosols

Aerosols, most simply defined as solid or liquid particles suspended in a gas, can be split into two categories defined by their formation mechanism:

- **Clouds**, which are formed via equilibrium, reversible processes of condensation of a gas, and
- **Hazes**, which are formed via disequilibrium, non-reversible processes.

Clouds and hazes are both abundant in Solar System atmospheres, as summarized in Figure 1.8 by Sarah Hörst, who also proposed the above formalism for defining clouds and hazes under the umbrella term “aerosols.” As explored in the thesis, aerosols are challenging to model, but also potentially incredibly consequential in exoplanet atmosphere observations (Marley et al., 2013).

In the case of a clear (aerosol-free) atmosphere, the scattering cross-section, which determines the optical depth for reflected starlight (equation 1.11), scales with wavelength λ as λ^{-4} . This dependence, combined with molecular absorption being stronger in longer wavelengths, means that the reflected spectrum measured on an exoplanet should drop off quickly when wavelength decreases, with relatively little contribution in the near- and far-infrared, where the thermally emitted spectrum dominates instead. If clouds are present, however, not only do they block starlight from passing through the terminator region, returning a featureless transmission spectrum, but they also introduce a bright, grey opacity (constant over a wide range of wavelengths), flattening out any distinction between the reflectance-dominated and emission-dominated regimes of the secondary eclipse spectrum (Marley et al., 2013; Cahoy et al., 2010).

⁴From: ‘Clouds and Haze and Dust, Oh My!’ by Sarah Hörst



Venus	H_2SO_4	H_2SO_4 and other heavier photochemical products like S_8 (?)
Earth	H_2O	Smog
Mars	H_2O, CO_2	No haze (but lots of dust)
Jupiter	H_2O, NH_3, NH_4SH	Forms from NH_3, CH_4, H_2S , etc. photochemistry
Saturn	H_2O, NH_3, NH_4SH	Forms from NH_3, CH_4, H_2S , etc. photochemistry
Titan	$CH_4, HCN, C_4N_2, C_2H_6$, other organics	Forms from CH_4, N_2, CO , etc. photochemistry
Uranus	H_2O, NH_3, NH_4SH	Forms from NH_3, CH_4, H_2S , etc. photochemistry
Neptune	CH_4, H_2S	Forms from NH_3, CH_4, H_2S , etc. photochemistry
Triton	N_2	Forms from CH_4, N_2, CO , etc. photochemistry
Pluto	N_2	Forms from CH_4, N_2, CO , etc. photochemistry
Exoplanets	CH_4, NH_3, H_2O alkali metals, iron, silicates, other, etc.	Yes. All the possible kinds.

Figure 1.8 Aerosols in the Solar System, credit: Sarah Hörst⁴. Aerosols, including both clouds and haze, are present in every planet, and most major moons, of Solar System bodies. The chemistry forming and maintaining these aerosols vary as widely as the planets' temperatures, pressures, and atmospheric constituents do, but the presence of aerosols in planetary atmospheres should not come as a surprise.

Global, high-altitude aerosols can enhance the albedo of a planet, as seen in Kepler-7 b ([Demory and Seager, 2011](#)), with a measured geometric albedo of ~ 0.30 , far larger than most of the previous findings for other hot giant exoplanets (e.g., albedo of 0.038 for HD 209458 [Rowe et al. 2008](#)).

I look at the impact clouds and hazes, separately and simultaneously, have on the final spectrum that we can actually measure.

Chapter 2: The Hubble Space Telescope, Unexpected Explorer of Extrasolar Atmospheres

*“The first few pictures came back blurred, and I felt ashamed
For all the cheerful engineers, my father and his tribe. The second time,
The optics jibed. We saw to the edge of all there is—
So brutal and alive it seemed to comprehend us back.”*

Tracey K. Smith, from “My God, It’s Full of Stars”

In this chapter, I briefly contextualize for the reader the *Hubble Space Telescope* as one of the primary, most essential tools in the characterization of exoplanet atmospheres, and the nearly exclusive source of data for my dissertation in particular. I present some preliminary, not-yet-published data to illustrate both the uses and challenges of using an instrument and telescope decidedly not intended as the marquee observatory of the first decade of characterizing the atmospheres of other worlds.

2.1 Why HST?

Though small, ground-based telescopes, even those of the backyard variety, are able to detect some exoplanets with relative ease, the characterization of exoplanet

atmospheres requires much higher sensitivity to detect the subtle modulations of a stellar spectrum by having passed through a planetary atmosphere. Ground-based transit observations require acquiring the spectrum of reference star of the same stellar type and brightness in the field simultaneously to account for atmospheric variability and wavelength-dependent effects. Finding such a reference star in the field is unlikely. There have been successes performing transit spectroscopy with high-dispersion spectrometers (e.g., [Redfield et al. 2008](#); [Snellen et al. 2008](#); [Birkby et al. 2013](#)), but the most important wavelength windows in the UV, near-infrared, and mid-infrared are virtually inaccessible from the ground. We must go to space, and we must use *HST* to access ultraviolet through near-infrared spectra; *Spitzer* provides complementary access to infrared spectrophotometry.

2.2 Planet Targets

The mass-radius diagram in [Figure 2.1](#) shows the two large surveys lead by Drake Deming. The first survey focused on giant planets across the mass distribution, and additionally targeted the “inflated” planets, which are among the most irradiated of them all, and consequentially get puffed-up to large radii. Upon the success and lessons learned with the first, the second program pushed down the mass-radius correlation to mini-Neptunes. The first result from that program is a Neptune-size planet with definitive water absorption detected in what appears to be a primordial atmosphere, rather than a secondary (out-gassed) atmosphere or one accreted/disturbed during migration ([Wakeford et al., 2017a](#)).

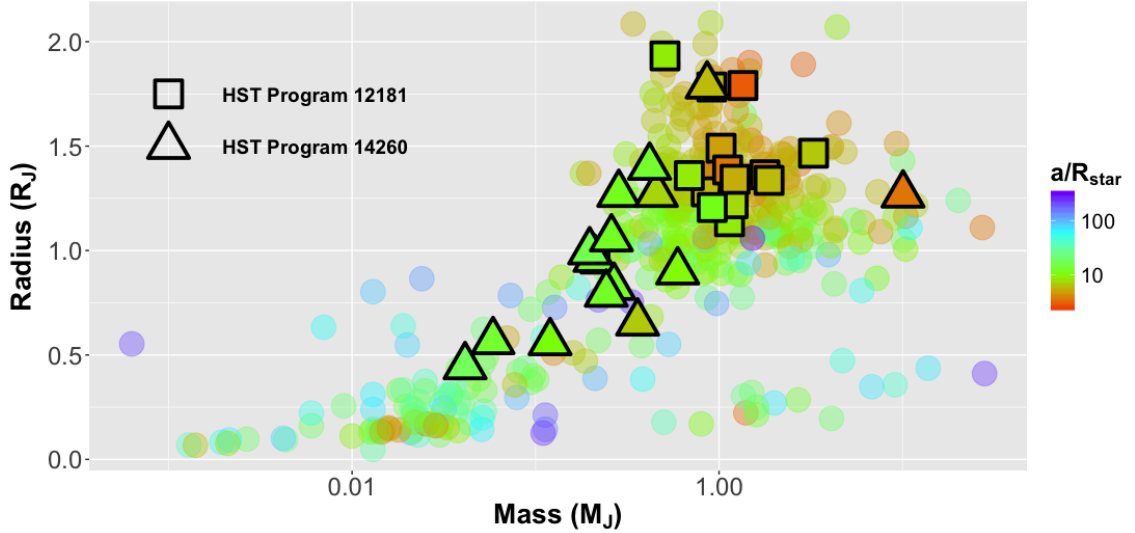


Figure 2.1 A mass-radius diagram of confirmed exoplanets for which both parameters are known, as of July 25, 2017¹, colored by their semi-major-axis-to-stellar-radius ratio (a/R_{star}). Overplotted are targets from the two large HST programs (PI Deming) that were the primary data sources for this thesis: Cycle 18 (observations 2010-11) in squares, and Cycle 23 (observations 2015-16) in triangles.

2.3 The Wide Field Camera 3

WFC3 was installed in the final *HST* servicing mission, replacing the Wide Field Planetary Camera 2 (WFPC2) in 2009. The data presented in Chapter 3, the observations of CoRoT-2b, are from one of the very first exoplanet characterization programs WFC3 carried out. We learned immediately that the WFC3 detector behaved curiously at the low noise levels we needed. As discussed in more detail in the next chapter, the detector suffered from low-level, time-dependent systematics that interfered with our attempts to achieve near-photon-limit-precision in time series data in order to even see a signal. I will leave the analysis of the original

¹Data from the [NASA Exoplanet Archive](#), which is operated by the California Institute of Technology, under contract with NASA under the Exoplanet Exploration Program

iteration of the WFC3 to the next chapter, and instead briefly describe what has managed to enable reaching that goal of near-photon-precision: spatial scanning. We found that those systematics were highly dependent on incident flux on the detector, though with far too much scatter to build a meaningful predictive model. Spatial scanning has the instrument drifting across the target, spreading the light from the star-planet system across the detector, maximizing the number of photons (to minimize SNR) while keeping the systematics somewhat at bay. Figure 2.2 shows an example of an uncorrected light curve; this one is particularly illustrative because it has so many orbits; most *HST* observations of exoplanet transits are 4 - 5 orbits, with the center two in transit, and the others just before and after. *HST* orbits the Earth in roughly 90 minutes, and spends a fraction of each orbit with the target blocked from view by Earth; this is why there are large gaps in coverage. WASP-18b is a particularly interesting planet, because it is in a tight 22-hour orbit, one of the shortest known, especially for a giant exoplanet. This observation is from the *HST* archive; the original PI was able to get a light curve covering the entire planet's orbit, which can serve other science goals, but, for our purposes, gave a far-larger-than-usual number of out-of-transit points, making the correction the systematics much easier: a version of the [Berta et al. \(2012\)](#) approach, which is to take advantage of the fact that the light curve should be flat and constant whenever not in transit, assuming a quiet star (not always a safe assumption). One can therefore make a template orbit by averaging all of the out-of-transit orbits, and simply divide that out. I take extra steps to account for the softening of the hook over the course of an observation; it is always worst in the first orbit and best in the last, so I fit for and

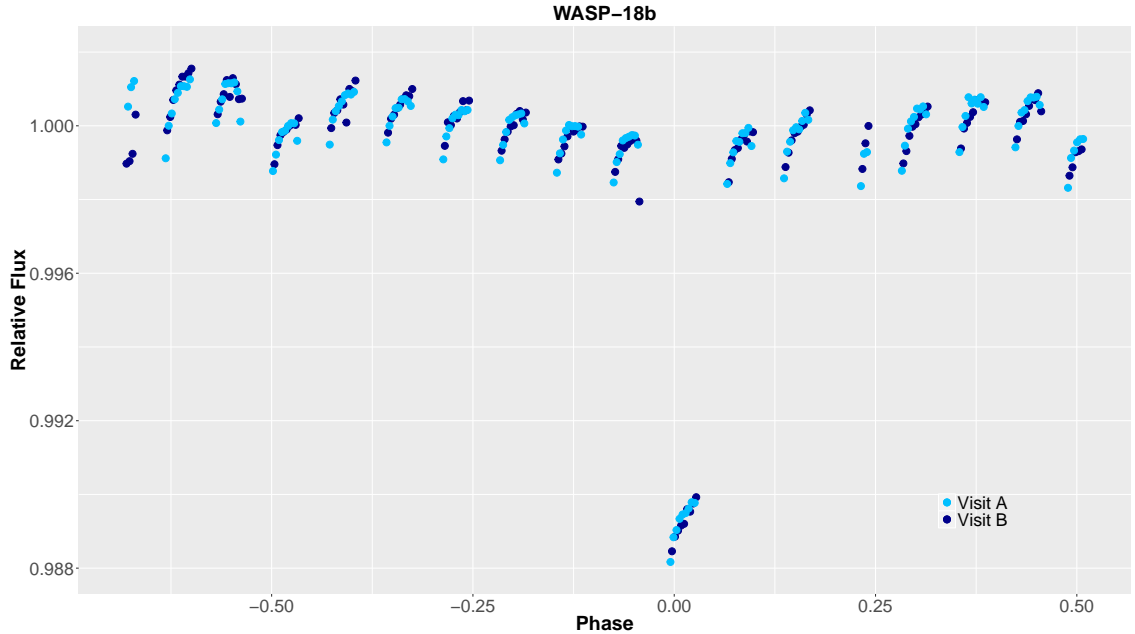


Figure 2.2 The WFC3 light curve (full phase) of the WASP-18b system, as seen with *HST* spatial scan. Visits A and B, denoted here by cyan and dark blue circles, are the forward and reverse scans, respectively.

quantify that evolution. Unfortunately, the systematics are not exactly the same manifestation each time, so I have to correct each data set separately. Attempts to get at the physical cause and/or develop a method to apply generally, such that we do not have to test and rewrite with each observation have proven to, at best, do no better than the divide-by-an-average method (e.g., the next chapter, also (Tsiaras et al., 2017; Zhou et al., 2017)). I include the (corrected) white light curves for HD 149026 and HAT-p-3b here, as well.

2.4 Future Outlook for HST Targets

While this entire dissertation could be seen as a treatise on the abilities of *HST* to rise to any challenge posed to it, we must recognize the *HST* – and nature herself

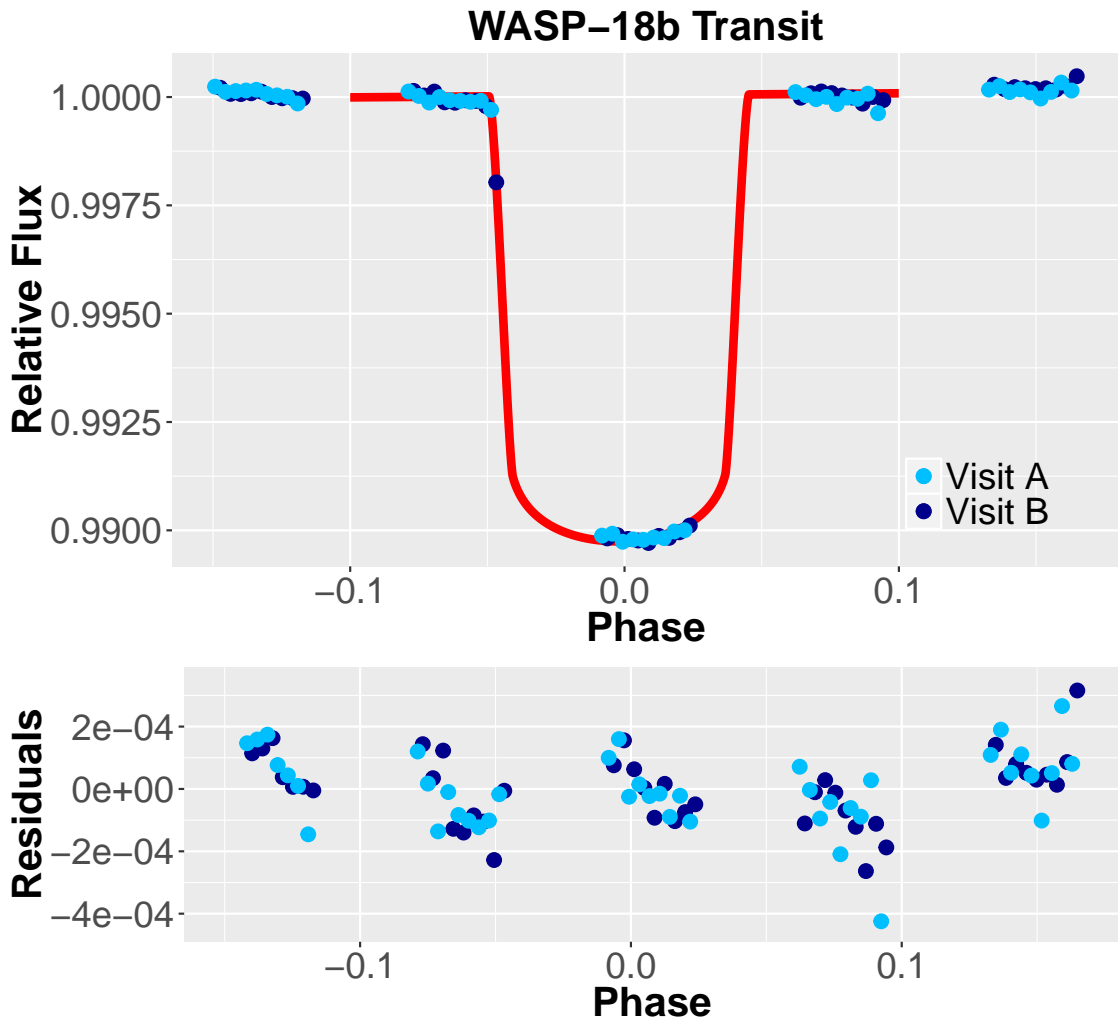


Figure 2.3 The systematics-corrected WFC3 white light curve of the WASP-18b transit, as seen with *HST* spatial scan.

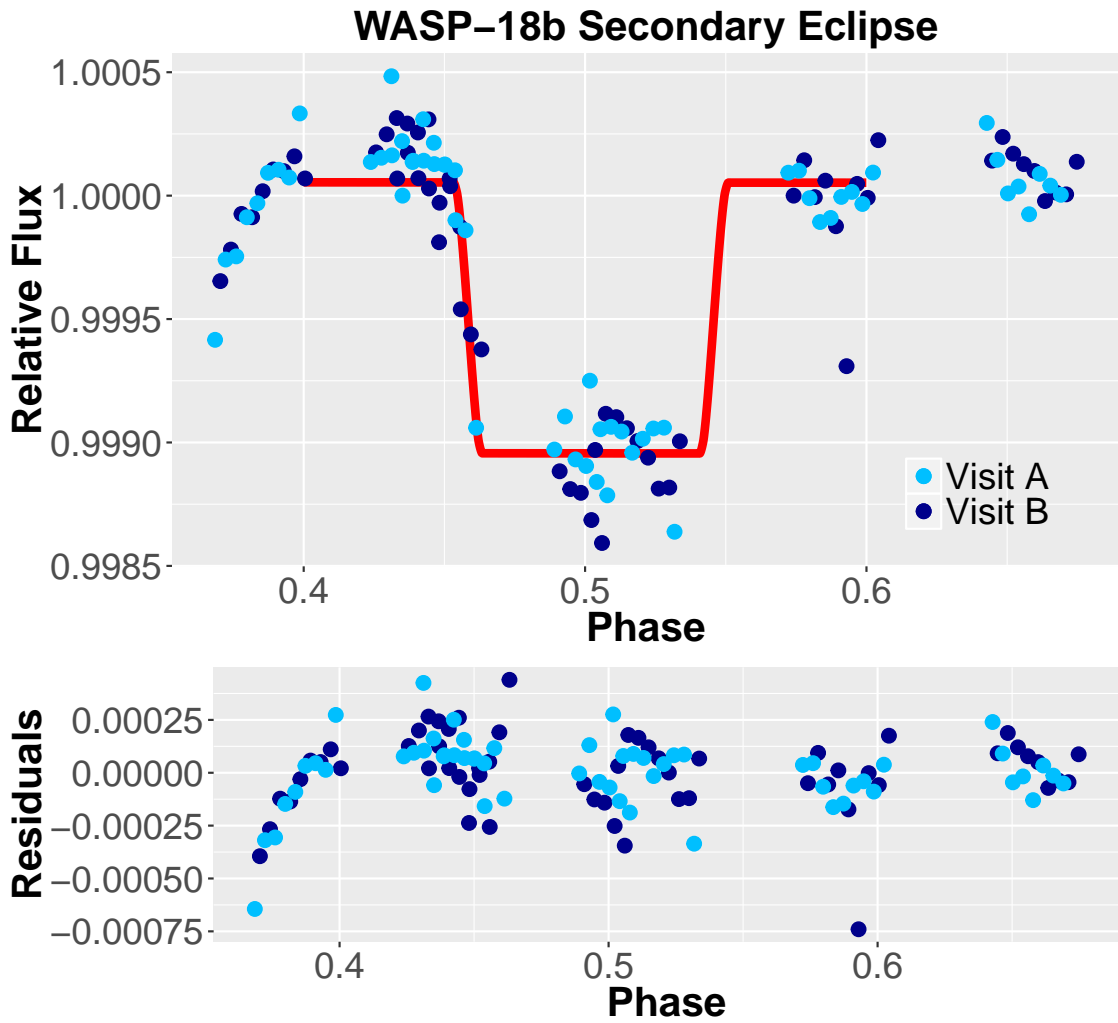


Figure 2.4 The systematics-corrected WFC3 white light curve of the WASP-18b secondary eclipse, as seen with *HST* spatial scan.

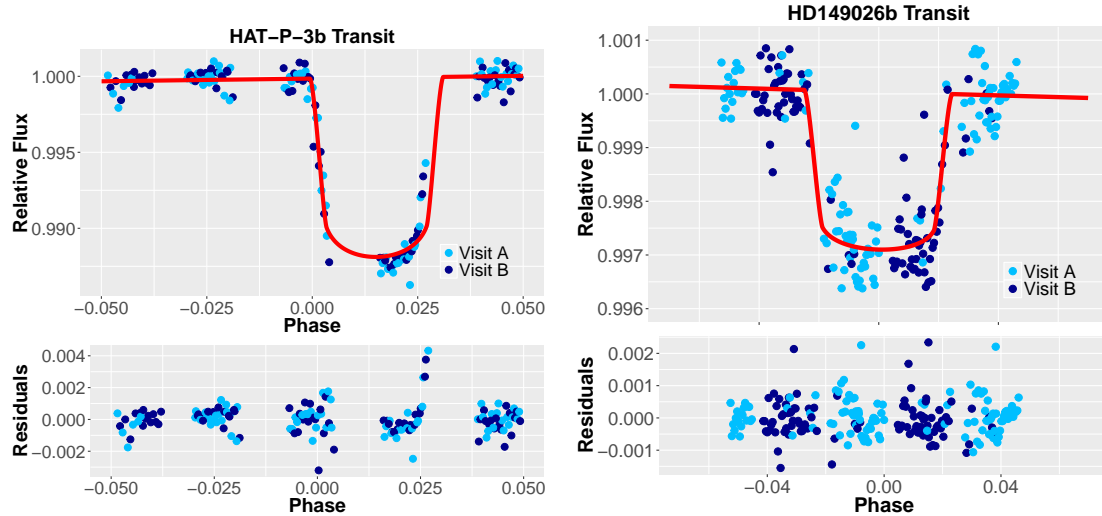


Figure 2.5 Systematics-corrected white light curves of the transits of HD 149026b and HAT-p-3b, and the respective residuals.

– have limits. *HST* requires targets to be bright stars, with favorable planet-to-star-radius ratios. There is simply a finite number of good targets for atmospheric characterization with *HST*. The TESS mission (Ricker et al., 2014) will find an incredible number of possibilities; see Figure 2.6. However, a careful look at the figure will reveal that TESS will not find many definitively “giant” planets. This is not because TESS cannot detect such planets, of course; the survey will “re-discover” plenty of our known giant planets. Instead, it is a sign that we are, or will be soon, approaching completeness of large planets around bright stars, which may not be able to be characterized from small, ground-based telescopes, but certainly detectable enough to discover/confirm. Such an inevitability is not to say that *HST* will ever worry about exoplanet proposal under-subscription, but that we as exoplanet astronomers must be deliberate about which planets we study, and also consider carefully how to use the observatory to understand giant planets as a population, given that we only get to observe a fraction of them.

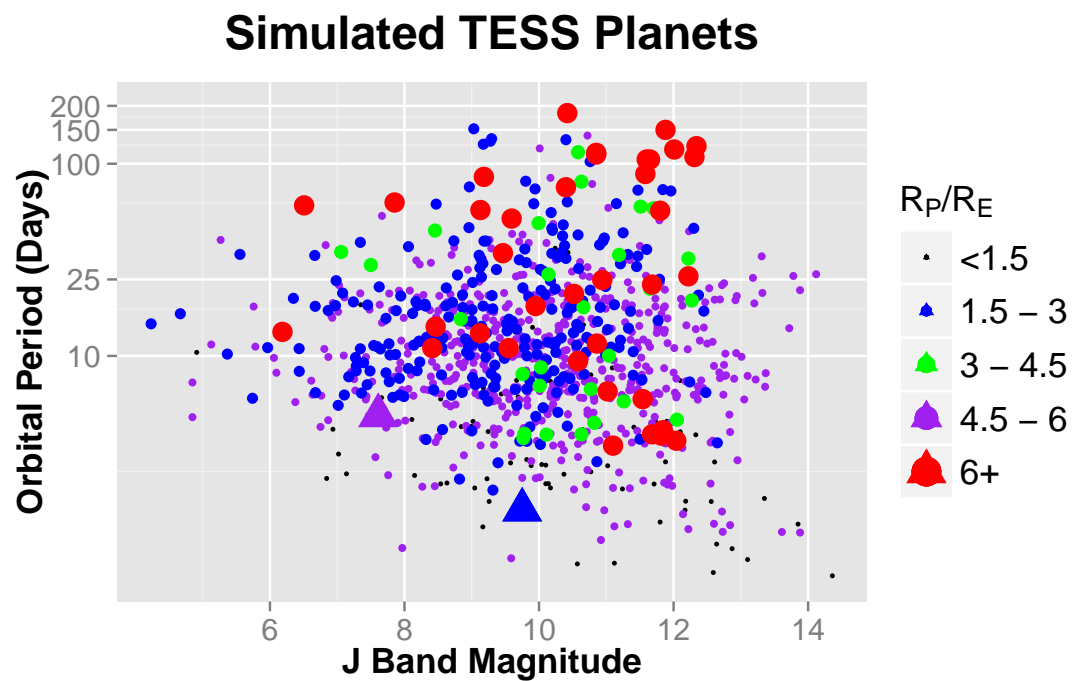


Figure 2.6 The predicted planet yield from the Transiting Exoplanet Survey Satellite (TESS), due to launch in March 2018, based on the results of (Sullivan et al., 2015); the colors and sizes of the points denote planet radius (R_p) in Earth radii (R_E). The large blue and purple triangles mark the coordinates of well-studied super-Earths/mini-Neptunes GJ 1214b and GJ 436b, respectively, for reference.

Chapter 3: The Emergent 1.1-1.7 Micron Spectrum of the Exoplanet CoRoT-2b as Measured Using the Hubble Space Telescope

Abstract

We have used Hubble/WFC3 and the G141 grism to measure the secondary eclipse of the transiting very hot Jupiter CoRoT-2b in the 1.1-1.7 μm spectral region. We find an eclipse depth averaged over this band equal to 395_{-45}^{+69} parts per million, equivalent to a blackbody temperature of $1788 \pm 18\text{K}$. We study and characterize several WFC3 instrumental effects, especially the “hook” phenomenon described by [Deming et al. \(2013\)](#). We use data from several transiting exoplanet systems to find a quantitative relation between the amplitude of the hook and the exposure level of a given pixel. Although the uncertainties in this relation are too large to allow us to develop an empirical correction for our data, our study provides a useful guide for optimizing exposure levels in future WFC3 observations. We derive the planet’s spectrum using a differential method. The planet-to-star contrast increases to longer wavelength within the WFC3 bandpass, but without water absorption or emission to a 3σ limit of 85 ppm. The slope of the WFC3 spectrum is significantly

less than the slope of the best-fit blackbody. We compare all existing eclipse data for this planet to a blackbody spectrum, and to spectra from both solar abundance and carbon-rich (C/O=1) models. A blackbody spectrum is an acceptable fit to the full dataset. Extra continuous opacity due to clouds or haze, and flattened temperature profiles, are strong candidates to produce quasi-blackbody spectra, and to account for the amplitude of the optical eclipses. Our results show ambiguous evidence for a temperature inversion in this planet.

3.1 Introduction

Very Hot Jupiters are gas-giant exoplanets with orbital periods less than about 3 days. The close proximity of VHJs to their host stars enhances the influence of irradiation, tidal forces, and stellar activity on their structure and evolution. CoRoT-2b (Alonso et al., 2008) is a VHJ of particular interest because of lingering questions about the structure of its atmosphere, which can be studied with observations of its secondary eclipse. Alonso et al. (2009) announced the first secondary eclipse observations of CoRoT-2 in the *CoRoT* optical waveband, followed by the mid-infrared *Spitzer* secondary eclipse measurements of Gillon et al. (2010), re-analyzed and expanded with Warm *Spitzer* eclipses by Deming et al. (2011). Alonso et al. (2010) added a secondary eclipse point in the K_s band. The analysis of Gillon et al. (2010) favored a poor day-night-side heat distribution in CoRoT-2b's atmosphere. Deming et al. (2011) found a high $4.5 \mu\text{m}$ flux as the only disagreement with a solar-composition, equilibrium chemistry model of the atmospheric temperature

structure. [Deming et al. \(2011\)](#) considered possible emission in the $4.5\ \mu\text{m}$ band from CO mass loss. Both works question, but do not rule out, the presence of a temperature inversion in the atmosphere caused by an upper atmosphere absorber. [Madhusudhan \(2012\)](#) finds that either a carbon-rich or solar abundance non-inverted model fits the data available in the literature.

These widely varied, competing explanations for this planet demonstrate the importance of spectroscopic observations. CoRoT-2b clearly does not fit the standard solar-composition, equilibrium chemistry model that satisfactorily describes many planets in its class, and we explore the anomalous spectral shape. For a clear illustration of CoRoT-2b's standing as an outlier among VHJs, see [Knutson et al. \(2010\)](#). CoRoT-2 is a very active star, a young Solar analog, and yet a temperature inversion cannot be ruled out and the planet does not fit clearly into the otherwise well-defined inverted/non-inverted planet classifications. This curious state of the planet is perhaps due to a magnetic interaction between the planet ([Lanza et al., 2009](#)) and CoRoT-2. Any further understanding would require more measurements of the planet in new wave bands.

In this paper, we use the G141 infrared grism on the Hubble Space Telescope's Wide-Field Camera 3 (HST's WFC3) to detect the day-side thermal emission spectrum of CoRoT-2b from $1.1\ \mu\text{m}$ to $1.7\ \mu\text{m}$. The CoRoT-2 system is part of an HST Cycle-18 program that observed a wide range of HJs/VHJs in transit and secondary eclipse, and gives us the basis for new insights into the instrumental effects of WFC3 ([Deming et al., 2013](#); [Huitson et al., 2013](#); [Line et al., 2013a](#); [Mandell et al., 2013](#); [Ranjan et al., 2014](#)). In what follows, we describe the observations of the CoRoT-

Table 3.1. CoRoT-2 Observation Summary

Visit	UT Date & Time (hr:min-hr:min)	Number of Exposures	Orientation Angle
A	10-18-2010 11:12-16:45	271	80.4°
B	9-16-2011 09:37-15:07	276	93.9°
C	9-23-2011 07:41-13:11	275	90.7°

2 system in §3.2 and the initial stages of data analysis in §3.3. In §3.4 we place our observations in the larger context of other HST programs with WFC3 in order to provide a comprehensive systematic description of the instrumental effects encountered in these observations. We then present our methods of obtaining the band-integrated secondary eclipse curve (§3.5) and derivation of the spectrum (§3.6) of CoRoT-2b. Finally, we use our results to constrain models for the atmosphere of the planet in §3.7, and we summarize in §8.

3.2 Observations

We observed CoRoT-2 using the G141 grism of WFC3 (1.1-1.7 μm), in three separate visits, each comprising four orbits of HST and hereafter called visits A, B, and C. We used the 128×128 -pixel subarray of the 1024×1024 -pixel detector. At the beginning of each visit, we acquired a single direct image of the system with the F139M filter, a medium-band filter centered at 1.39 μm ; the location of the target

in this direct image defines the initial wavelength solution for the grism spectra. A summary of the observations is in Table 3.1.

Most of our observations in program 12181, including those of CoRoT-2, were executed before the advent of spatial scan mode (McCullough and MacKenty, 2012). Lacking the spatial scan, WFC3 observations of relatively bright stars can be inefficient, because the time required to transfer the data greatly exceeds the exposure time for bright exoplanet host stars. We maximize the efficiency by using subarrays and by exposing the detector to fluence levels approaching or equaling saturation. Even at a saturated exposure level, an unsaturated signal is available because the detector is sampled ‘up the ramp’ multiple times within each exposure, and all the samples are saved in the data. Isolating less than the full number of samples, a linear signal can be obtained even in the saturated case. Our CoRoT-2 grism data are exposed so that the brightest pixel contains about 70,000 electrons in a full exposure, which is approximately the level of 5% non-linearity.

3.3 Initial Data Analysis

In order to explore whether our results are sensitive to details of the data analysis, we use two parallel but independent methods to process the data. To avoid confusion with the visit terminology (A, B, C), we denote the two methods as α and β . Method α makes more explicit corrections and manipulations of the data than does method β . Exoplanet signals are subtle, and the more the data are processed, the more the potential for adding numerical noise that may mask

the small exoplanet signal or even fooling oneself into detecting a false signal. Our dual-track analysis allows us to evaluate the trade-off between the most ‘complete’ method versus the potential for degrading the results by over-processing of the data. It also allows us to evaluate what corrections are necessary, and what corrections can be neglected. Upon measurement of the eclipse curve, the methods yield consistent results.

Method α uses “flt” FITS image files retrieved from the Mikulski Archive at Space Telescope (MAST) server, located at the Space Telescope Science Institute (STScI). The “flt” files were calibrated through the WFC3 pipeline’s high-level task, `calwf3`, which includes two low-level tasks, `wf3ir` and `wf3rej`, that apply to the infrared channel. `wf3ir` performs standard calibrations, including corrections for bias, non-linearity, dark current, and bad pixels due to energetic particle hits, while `wf3rej` completes more bad pixel rejection and combines images. [Rajan and et al. \(2011\)](#) gives details of this pipeline. We multiply the resultant signal rates (electrons per second) by the integration time to infer the accumulated signal on each pixel, in electrons.

Method β begins with “ima” FITS files from the MAST server. These files give the ‘sample-up-the ramp’ values of each pixel at 4 times during each 22-second exposure, and are processed to correct for non-linearity, but not to reject energetic particle hits. We process these files (minimally) by fitting a linear slope to the four samples as a function of time for each pixel, to determine the rate at which electrons are accumulating in the pixel. Our linear fit weights each sample of a given pixel by the square-root of the signal level, as appropriate for Poisson errors. Multiplying

the fitted slope by the 22-second integration time yields the accumulated signal in electrons. This process does not include any correction for energetic particle hits. Rather, we correct those at later stages of the β -analysis, and we also evaluate the success of the non-linearity corrections by repeating the β -analysis and restricting the linear fit versus sample time to only the first three samples.

Using the smaller subarray means the grism data consists of the central 128 pixel columns of the first-order spectrum out of the 150 on a larger (sub)array. Nevertheless, using the 128 subarray increased the efficiency of the observations (i.e., minimizing data transfer time on the spacecraft), more than justifying the loss of points at the edges of the grism response.

To extract the spectrum of the star+planet system, we sum the pixels after background subtraction, using a box defining a range in rows. We adopt a box size of height 61 pixels (a central pixel, plus 30 above and below it). The box length is the full 128 pixel length of the subarray, but we later trim the spectrum in wavelength. We sum the box over rows to produce spectra, and we further sum over wavelength to produce a ‘white light’ photometric time series. The spectra are very stable in position (jitter less than several hundredths of a pixel), and the intensity level falls by 2.5 orders of magnitude over the 30-pixel half-height of the box. Therefore we use fixed integral coordinates for the box in each visit, and we weight each pixel equally when performing the sum. This spectral extraction is the same for both the α and β analyses.

In the following, we discuss the various sub-elements of the data analysis (§3.3.1,3.3.2) including the wavelength calibration (§3.3.3) and flat-fielding (flux cal-

ibration, §3.3.4), while the more extensive task of characterizing the instrumental systematics is discussed in §3.4.

3.3.1 Bad Pixel Correction

Bad pixel correction due to energetic particle hits is part of the calwf3 processing used for our α analysis. Additional pixels not identified by calwf3 may still be erroneously high or low in value and need correction. For both α and β analyses, we identify and correct bad pixels immediately prior to the spectral extraction (i.e., before summing the box). Our α analysis inspects pixels in each column of the spectral box (i.e., a single wavelength) that deviate significantly from a Gaussian profile of the spectral trace. Such deviations are virtually always characterized by much higher intensity levels. Those pixels that are more than 10 times greater than the fitted Gaussian value are replaced by a 7-pixel median in the vertical direction (perpendicular to the dispersion) at that wavelength.

Our β analysis must be more sophisticated as regards bad pixels, since these data have not been processed by calwf3. We examine the ratio of a given pixel to the total of all pixels in that row, i.e., the ratio of a single pixel to the sum over wavelength at each spatial position. Because of spatial pointing jitter, pixel intensities can vary with time in an absolute sense, but their relative variation should be similar at all wavelengths. We examine the ratio as a function of time (i.e., for each exposure) and we identify instances where a given pixel does not scale with its row sum. We identify $> 4\sigma$ outliers, and correct them using a 5-frame median value

of the ratio at that time.

3.3.2 Background Subtraction

For both the α and β analyses, we calculate the background individually for each exposure by using pixels outside of the spectral box. Specifically, the pixels used are those that lie directly below the spectrum on the subarray, which is the section of the subarray corresponding to the width of the spectrum and extending from the bottom edge of the spectral box to the bottom edge of the subarray. We construct a histogram of intensity values in these pixels and fit a Gaussian to the histogram. The adopted background value is the intensity corresponding to the central value of the fitted Gaussian, and we do assume that it is independent of wavelength to the limit of our precision. This is typically a few tens of electrons per pixel, several orders of magnitude less than the signal in the stellar spectrum, and the sum is thus also significantly lower when calculating the white light curve and its corresponding background. Background subtraction therefore has a relatively minor effect on our analysis.

3.3.3 Wavelength Calibration

Wavelength calibration utilizes both the direct image and the spectral image, as the wavelength of a given pixel depends upon its location on the detector relative to the direct image. [Kuntschner et al. \(2009\)](#) outline the procedure for wavelength calibration in an STScI calibration report. The equations governing the wavelength

for a pixel at a given x-position in the first-order spectrum are:

$$\lambda(x) = dldp_0 + dldp_1 \Delta x \quad (3.1)$$

where

$$dldp_0 = a_0^0 + a_0^1 x_{center}$$

$$dldp_1 = a_1^0 + a_1^1 x_{center} + a_1^2 y_{center} + a_1^3 x_{center}^2 +$$

$$a_1^4 x_{center} y_{center} + a_1^5 y_{center}^2$$

$$\Delta x = x - x_{center}$$

The terms x_{center} and y_{center} are the central coordinates of the direct image. The coefficients (a_0^0 , a_0^1 , etc.) are calculated in [Kuntschner et al. \(2009\)](#).

In performing this calibration, we found that the calibrated grism response (sensitivity) curve did not line up precisely in wavelength space with the observed response (see [Figure 3.1](#)). We therefore adjusted the coefficients empirically to obtain optimal agreement with the observed grism response curve and with the wavelengths of two stellar hydrogen lines (Pa- β at 1.282 μm and Br-12 at 1.646 μm). These adjustments yielded:

$$a_0^0 \rightarrow 0.997 \times a_0^0$$

$$a_0^1 \rightarrow 0.90 \times a_0^1$$

$$a_1^0 \rightarrow 1.029 \times a_1^0$$

We used these adjusted values in the calibration presented in this work and also successfully applied them to other data sets in this HST program. Therefore, this empirical correction is not specific to this target or these visits, and we in fact used another object in the program (TrES-2) to find the correction, as it was observed on the larger subarray and thus the observations include all 150 pixels of the spectrum.

3.3.4 Flux Calibration

The flat field and sensitivity curve of the G141 grism on the WFC3 detector are the two components of flux calibration, and both are wavelength-dependent.

For imaging observations, `calwf3` applies the flat field to the data, but flat-fielding of grism data must be done by the observer. STScI provides a flat-field cube for the G141 grism. This cube is a four-extension FITS file, and each extension is the size of the full WFC3 IR array. For a given pixel on the data image with a given wavelength, the flat-field value for that pixel is given by a polynomial function with coefficients defined by the values of the flat-field cube extensions at the pixel's location.

This method is described in the aXe handbook (Kümmel, 2011) and laid out with the equations that follow. For a pixel at position (i,j), they define a normalized wavelength coordinate, x :

$$x = \frac{\lambda - \lambda_{min}}{\lambda_{max} - \lambda_{min}}$$

The parameters λ_{min} and λ_{max} are constants found in the flat-field cube header.

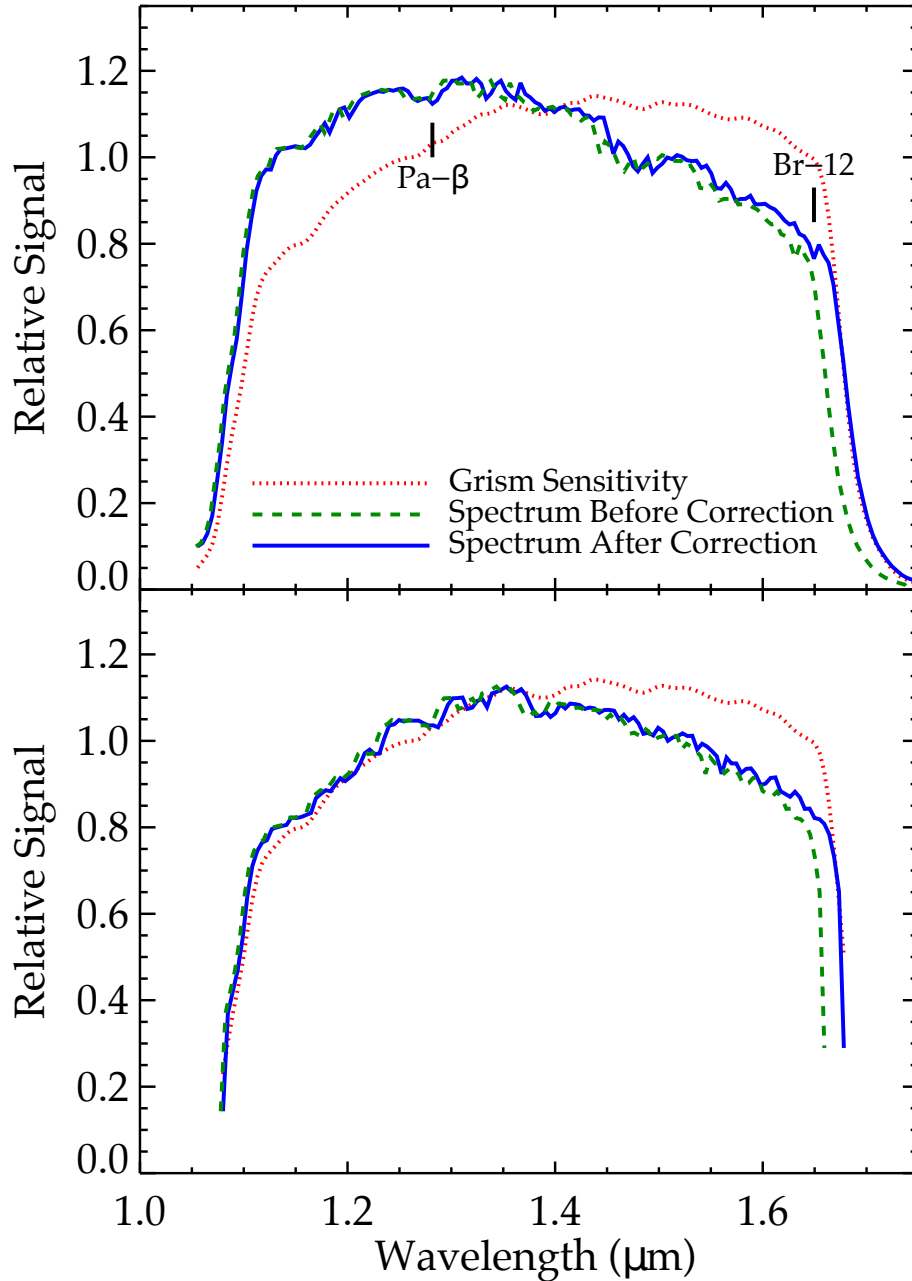


Figure 3.1 Flat-field-corrected spectrum of TRES-2 (*above*) and CoRoT-2 (*below*). Each plot shows the WFC3 G141 grism sensitivity curve (*red, dotted line*) and the spectrum before (*green, dashed line*) and after (*blue, solid line*) the correction has been made to the wavelength solution coefficients. The two hydrogen lines, Pa- β (1.282 μm) and Br-12 (1.646 μm), the two lines in TRES-2 used to adjust the wavelength coefficients, are also marked here. To get a normalized spectrum, one must simply divide by the sensitivity curve.

The flat field value of a pixel (i,j) with normalized wavelength coordinate x is then a polynomial function in x :

$$f(i, j, x) = a_0 + a_1x + a_2x^2 + a_3x^3 \quad (3.2)$$

where a_0 , a_1 , a_2 , and a_3 are the values at (i,j) in the zeroth, first, second, and third extension arrays in the flat-field cube file, respectively. For both our α and β analyses, we apply the flat-field correction to the spectral box by dividing by the corresponding flat-field “box,” generated pixel-by-pixel from the method above.

STScI also provides the wavelength-dependent sensitivity of the G141 grism. In Figure 3.1, we plot the scaled sensitivity curve over a flat-fielded spectrum from a single exposure of TRES-2, along with the two hydrogen lines used as reference points in adjusting the wavelength calibration coefficients.

3.3.5 Second, Overlapping Source

CoRoT-2 has a companion star, so our analysis must remove or correct for this second source. The direct image of CoRoT-2 appears in Figure 3.2, where the second, fainter source is evident. The proximity of the second source in the image depends on the orientation angle of the telescope, and varies between the three visits, but it is close enough to be of concern for source contamination. The spectra overlap minimally in visits A and C, but there is significant overlap in visit B, which has the lowest orientation angle and thus the smallest distance between the two spectra of the three observations. The orientation angles, which only vary a few degrees from each other, are reported in Table 3.1.

3.3.5.1 Characterization

This second source is an infrared source, 2MASS J19270636+0122577, but is just barely spatially resolved by the 2MASS observations. In the planet’s discovery paper, [Alonso et al. \(2008\)](#) suggest it may be a late-K or M-type star, and [Schröter et al. \(2011\)](#) identify it as a late K-type star. Both works posit that it may be gravitationally bound to CoRoT-2. We here address how to remove, or correct the effect, of this second source from the flux of the CoRoT-2 system. We have explored two approaches. Our α analysis removes the second source prior to extracting the grism spectrum from the 2-D frames. Our β analysis includes the second source in the extracted grism spectra, and corrects the derived exoplanetary spectrum after deriving that stellar spectrum.

The location of the second source allows us to generate its spectrum, albeit in a limited wavelength range. Its spatial offset results in losing the long-wavelength end of its spectrum. Comparing the partial spectrum to a grid of Kurucz models shows general agreement with the findings of [Schröter et al. \(2011\)](#); a temperature of 4000 K and surface gravity $\log(g) = 4.0$, produces the best agreement with the observed partial spectrum. That corresponds to a late K- or early M-type main sequence star.

3.3.5.2 Removal

In our α analysis, the strategy for removing the second source from visits A and C is to determine the average spatial shape of the source’s signal, and scale

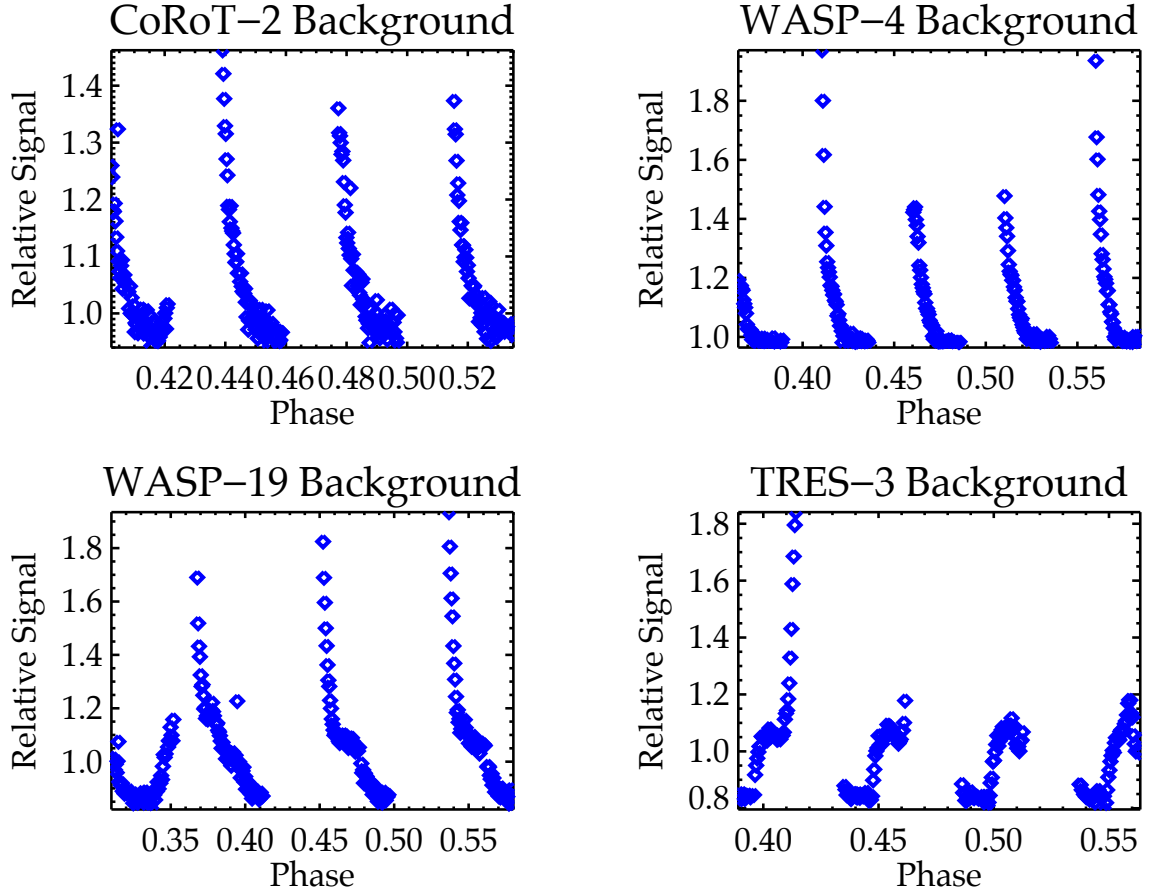


Figure 3.2 *Left*: The direct image of CoRoT-2 (brightest object, center of each image) and the infrared source nearby in visits A (*top*), B (*middle*), and C (*bottom*). *Right*: A vertical profile of the first-order spectrum resulting from a horizontal dispersion of the light to the right of the direct image for each of the three visits; the solid, black line is the original trace, while the dashed, red line is the trace after correction. The variation in degree of overlap of the spectral trace is due to variation in the orientation angle of the telescope between the visits, which changes the proximity of the second source’s spectrum to that of the target. The orientation angle was limited to the range $76^\circ < \text{ORIENT} < 166^\circ$ by telescope operation parameters, and the actual angles were 93.9° , 80.4° , and 90.7° , for visits A, B, and C.

and subtract it from each column of the spectral box. We fit a Gaussian plus a second-order polynomial baseline to the spatial profile at each column of the data. Averaging that fit over all exposures then approximates the signal from the second source for a given column, after scaling the average to represent the amplitude of the second source for each column. The original spectral trace – the plot of wavelength-integrated flux versus spatial pixel – appears in Figure 3.2, as well as the corrected spectral trace (overplotted), showing significant improvement.

For visit B, the task is more difficult. The peaks of the two sources are separated by just four pixels, compared to twelve and ten pixels for visits A and C, respectively. The overlap leaves too few points to use a fitting procedure to isolate and approximate the source. Instead, we use the descent of the PSF on the opposite side of CoRoT-2 from the overlap of the second source, and mirror the PSF column-by-column onto the side with overlap. We subtract the mirrored PSF, and fit a Gaussian column-by-column to the difference. Averaging that fit over all exposures, we approximate and remove the second source from each column for visit B.

3.4 Systematics: Characterization

Our data exhibit trends in the measured stellar intensity that are not manifestations of physical stellar or planetary phenomena. Instead, they represent tendencies of the detector to report signal counts that are different from what actually fell on a given pixel.

We note that instrument-related systematic errors in WFC3 exoplanetary spec-

trosopy are believed to be less severe than in NICMOS observations (Gibson et al., 2011; Crouzet et al., 2014; Deming et al., 2013; Swain et al., 2013). Nevertheless, instrument effects do exist in the WFC3 data, especially for observations taken before the advent of spatial scan mode (McCullough and MacKenty, 2012) such as ours. Some aspects of these instrumental effects were discussed by Swain et al. (2013). Berta et al. (2012) reached nearly the photon limit in their analysis of WFC3 G141 transit spectra of the super-Earth GJ1214b, as did Deming et al. (2013) for two giant transiting exoplanets with the implementation of the spatial scan mode. We will discuss the analysis of the Berta et al. (2012) work and how we modified it for more general purposes in §3.5.

We identify three primary manifestations of systematic error, and all are patterns in intensity as a function of time. The first is a continuous trend of the source’s white light curve lasting the entire length of a visit, during which the intensity gradually decreases with time (or increases, in one case). This “visit-long ramp” is linear in nature (to within the errors), and continuous between orbits. Its slope varies widely between observations, not only among the CoRoT-2 visits, but among all in our HST program. Its strict linearity and variation even when separately observing the same star places it clearly in the category of instrumental effects rather than stellar modulations, but the exact cause is an open question. The second systematic error feature is a decrease of intensity as a function of time, which repeats for every orbit. This effect is apparent in the pixels *not* illuminated by the source spectrum – including the pixels we use for the background subtraction – and is shown for the examples of CoRoT-2 and others in Figure 3.3. For most objects in the program, the

effect shows a smooth, exponential decrease in the signal for these pixels over the course of an orbit, though some observations show an effect in more of an "S"-shape instead. Removal of the background, as per the method described in 3.3.2, removes any discernible presence of this effect, which allows us to conclude first that the effect is isolated to the lowest-valued pixels, and second that we need not perform further tasks to eliminate this orbit-long feature, as the problem is solved by careful background definition and subtraction. We find no definitive cause, though we suspect it may be due to scattered light from the Earth's limb.

The third example of systematic error is an increase in intensity of the source's white light curve which occurs on a shorter time scale, over the course of several exposures, and which repeats three or more times in every orbit. We call this the "hook" (Deming et al., 2013) because of its characteristic shape, which is a steep jump for the first one to three exposures and then a flattening¹. The hook appears to a varying degree in all of the observations, and produces a significant distortion in the data. Examples of the hook within a single orbit of observations for four different objects are shown in Figure 3.4. The reset of this pattern corresponds with the time when the data stored in the WFC3 buffer are sent to the solid-state recorder on the spacecraft. This causes a short break in observations, and also resets the detector. Neither of the other two primary systematic effects appear to have any dependence on times of data transfer.

¹Some investigators call this effect a 'ramp', but we advocate different terminology so as not to confuse it with the visit-long ramp, and also to distinguish it from the Spitzer ramp.

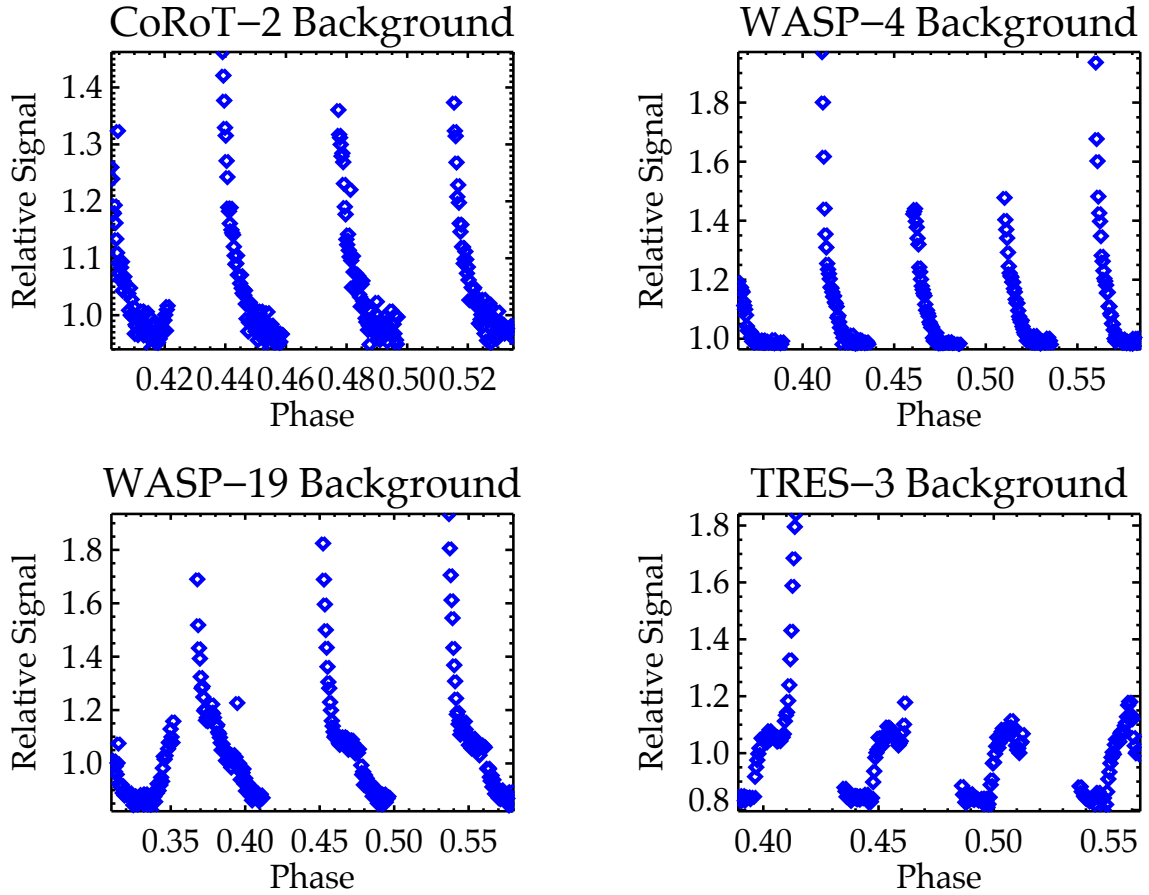


Figure 3.3 The normalized signal measured from the background pixels over the course of the observations. This systematic effect resets after each orbit of the telescope (between orbits there is a gap in time as HST passes behind the Earth). For most objects in our program, the effect is a smooth exponential decrease, as shown here for CoRoT-2 and WASP-4 in the upper panels. For some observations the shape is different, an irregular "S"-shape, as for WASP-19 and TRES-3 in the lower panels.

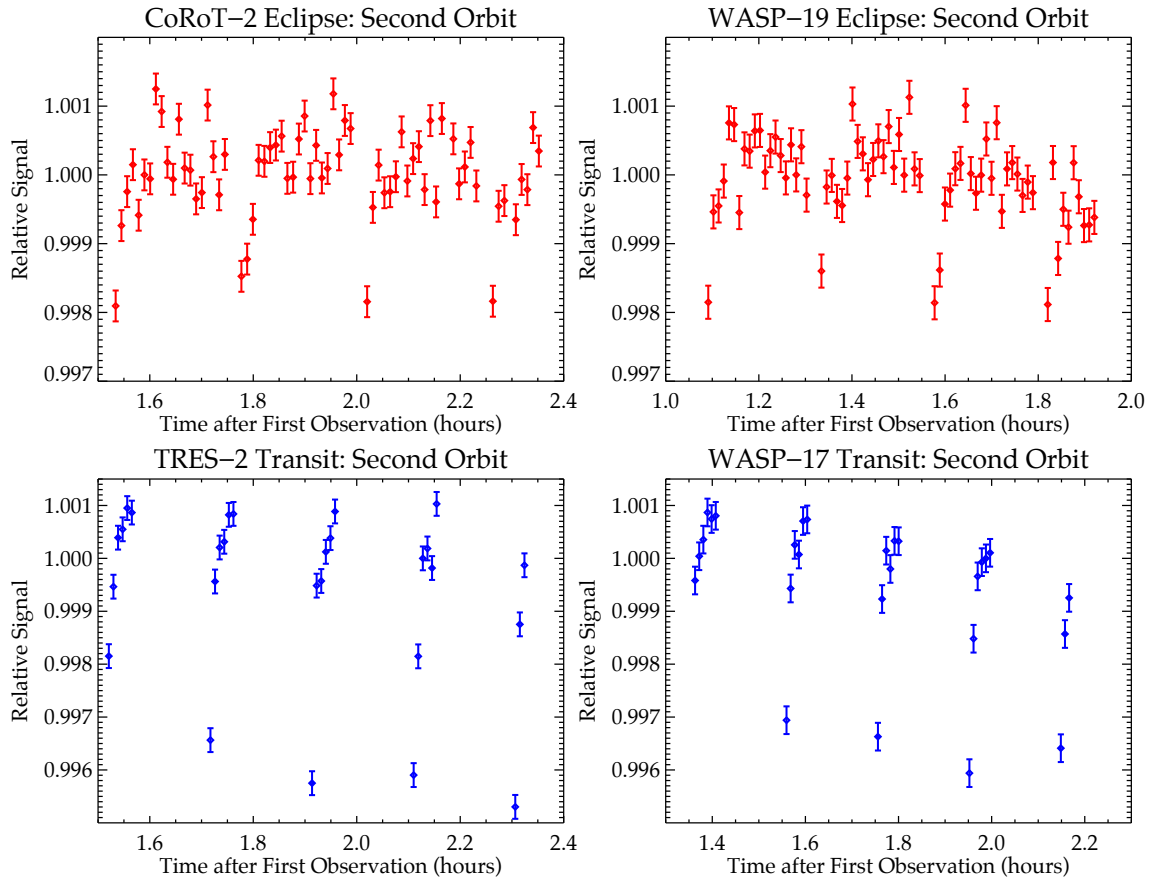


Figure 3.4 Four examples of the systematic hook pattern. WASP-19 and CoRoT-2 (*top*) were both observed on the smaller subarray, and have more exposures in the pattern, a more subtle pattern, and less time in between iterations. HAT-7 and TRES-2 (*bottom*) were both observed on the larger subarray, and have fewer exposures in the pattern, a more obvious pattern, and a much larger gap in time between the observations.

The hook pattern is of similar shape in all sets of observations in the program, but the parameters of its manifestation, e.g., length of time, number of exposures, number of iterations, vary from object to object. Figure 3.4 shows examples of the pattern in four different objects; the shape of the pattern is similar, but the amplitude of the hook and the time between buffer dumps (and thus the number of exposures and total time of each hook) varies. Swain et al. (2013) concluded that it was most significant for the 512×512 subarray. We concur that it is often prominent at 512×512 , and it is considerably steeper for longer-duration patterns on 512×512 , but we detect it in other subarrays also. The prominence of the pattern correlates with brightness of the star.

While the visit-long slope appears to be linear, both the orbit-long and hook effects are exponential in shape, and therefore each begins as a very strong effect and then becomes nearly indiscernible in the final exposures of each hook pattern.

There are further apparent systematic effects seen in the first orbit of every observation; they are most likely due to telescope settling and readjusting to a new pointing, and do not have a consistent pattern. Therefore we discard the first orbit once we begin applying corrections to the systematic effects for the purpose of calculating the wavelength-integrated transit depth, and the spectrum of the planet. Since the eclipse of CoRoT-2b is covered by three visits, loss of the first orbit is only a minor perturbation for our analysis.

3.4.1 Persistence Correction

One potential cause of the hook effect is detector persistence, the phenomenon in which trapped charge in an exposure is slowly released in following exposure(s) to produce a falsely increased signal detection (Smith et al., 2008). STScI publishes persistence models and even predictions of persistence for a given exposure based on the exposures prior to it. The predictions are for an additive effect, and the data product for a given exposure is an image array the size of the original exposure, but with each pixel value equal to the the predicted persistence, so the correction is simply to subtract the corresponding pixel values. The persistence is low for the first exposure, but jumps up quickly and remains at a higher value until the time of the data transfer, when it, too, resets. The additive correction as given by STScI do decrease the severity of the hook, but they do *not* entirely remove the hook, and we conclude that the hook is a combination of a additive and *multiplicative* effect. This will justify our methods of correction outlined and examined in the sections that follow. We have made the STScI persistence correction in our α analysis. Our β analysis ignores additive persistence, as do most WFC3 exoplanetary investigations published to date.

3.4.2 Pixel-by-Pixel Evaluation of the Hook

Berta et al. (2012) demonstrated that the hook is more prominent at high exposure levels. We have investigated the amplitude of the hook as a function of the per-pixel exposure level, and other parameters, and we seek quantitative

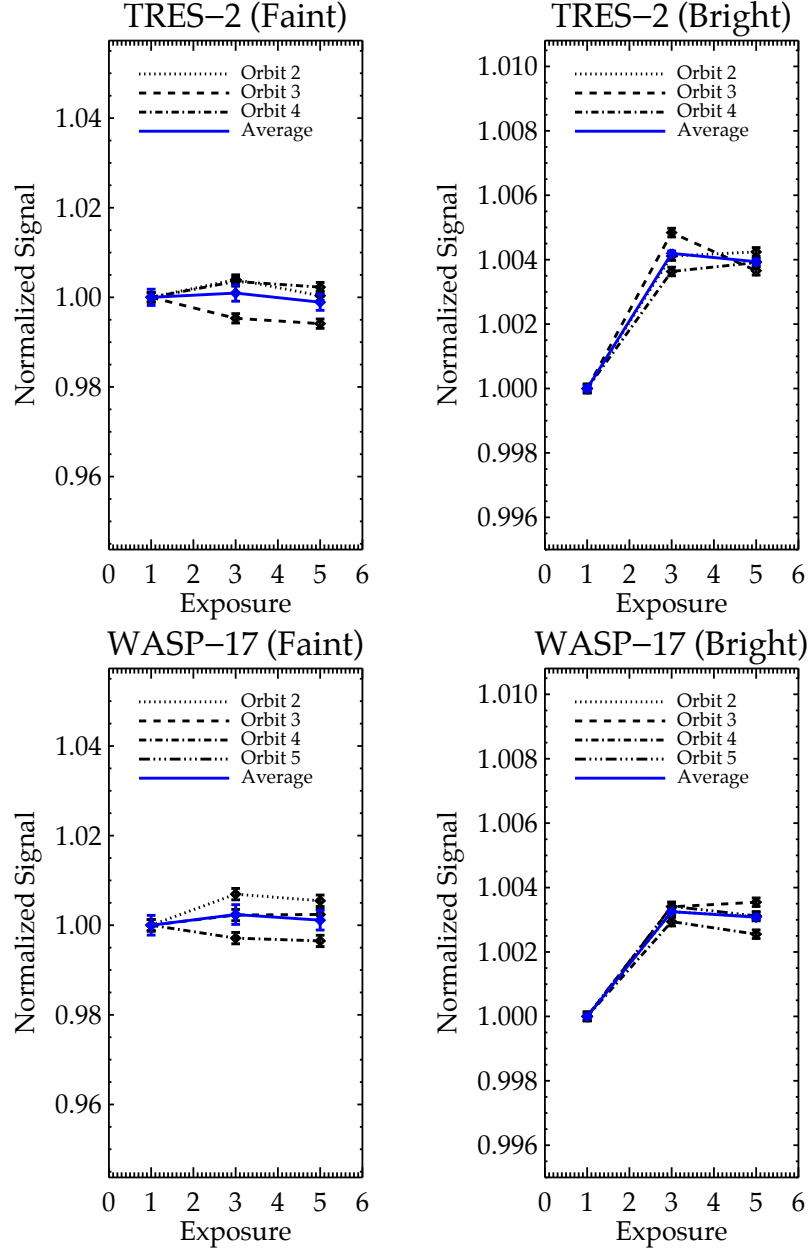


Figure 3.5 Examining the average shape of the hook pattern for two sets of observations. We calculated the total flux in the spectral box at the beginning, middle, and end of the pattern, averaged over all the iterations within an orbit, and then plotted the average normalized to the first average value. For each object shown, the pixels in the spectral box have been split in half about the median value: the faint half and the bright half, and then plotted separately. As is apparent with this split, the fainter pixels are not affected by whatever causes the pattern, while the brighter half are.

relationships. For each pixel, we average the change in signal level over the multiple iterations of the pattern within one orbit, and then examine the change as a function of time within the pattern, flux of the pixel, and location of the pixel on the detector.

The average shape of the hook for two objects in the program can be seen in Figure 3.5. The normalized signal is shown against the exposure number within the pattern. For each visit, the pixels have been split between those with flux below the mean and those with flux above the mean. This is done to confirm that the existence of the hook does indeed depend upon the flux of the pixel.

Figure 3.6 shows this dependence of the additive change on the flux of the pixels, where every pixel has been plotted by its initial flux and "jump" in electrons between the first exposure and the last exposure in the pattern. The jump is statistically insignificant below a certain original pixel value, but shows a reliable parabolic rise starting around 30,000 electrons. The scatter is nevertheless remarkably large, which ultimately means that we cannot depend on a unique quantitative relation to correct this effect.

In principle, the hook could be removed by using Figure 3.6 to predict the magnitude of the jump for a pixel given its initial flux in the first exposure of the pattern, and thereby correct each pixel in each image. We attempted such a correction, and it does remove the obvious appearance of the hook pattern, but it leaves the data with much more scatter than is acceptable, due to the wide variations seen in Figure 3.6.

We also examined the amplitude of the hook as a function of position on the

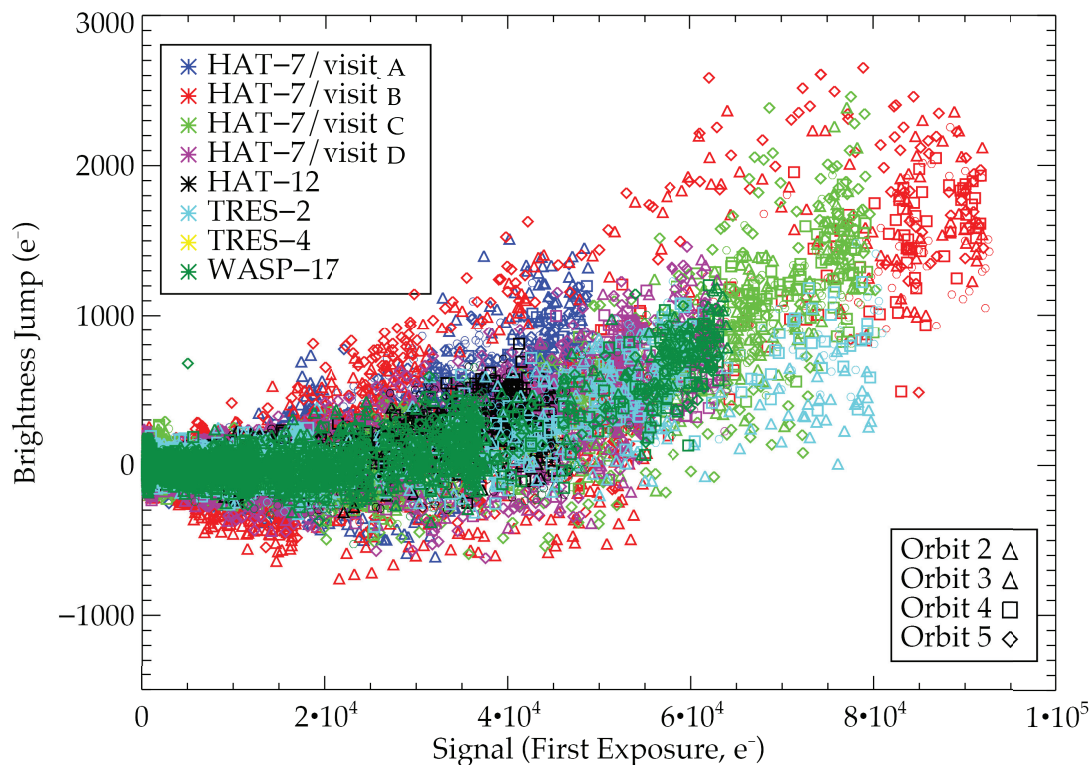


Figure 3.6 A quantification of an additive effect from the detector for a selection of objects. The hook pattern repeats multiple times in each orbit, and each visit has 4-5 orbits. For every orbit in every visit, coded by symbol and color, we have averaged the increase in measured flux from the first to the second-to-last exposure in each pattern for each pixel in the spectral box. This is plotted against the initial flux of each pixel in the first exposure of a hook. The increase is clearly dependent upon the flux level, and does not become apparent (on average) until a signal of about 30,000 electrons. The legend shows which visit corresponds to which color. The relation between initial flux and flux jump appears to be steeper for longer pattern times.

detector. We find no correlation in column (wavelength) space, but some correlation with the slope of the hook pattern and the row on the detector, i.e., how far a given row is from the spatial center of the spectrum. This correlation does seem to strongly depend on which subarray we used. Especially in the case of the 128×128 subarray, the slope of the trend is more positive for the rows of pixels below the central peak of the spectrum (in the direction perpendicular to dispersion), while the slope is less positive for those rows above the central peak. This correlation is weaker for the 512×512 subarray, but still discernible. Figure 3.7 shows the correlation for the smaller subarray by demonstrating the shift in the spatial center of the spectrum between the starting and ending frames of the hook. Our finding that the nature of the hook depends on the row of the spectrum may be a significant clue to the nature of this effect. Reading the detector involves addressing the pixels by row, and it is conceivable that the hook is related to the manner in which the detector is addressed and sampled. We conclude that the effect in Figure 3.7 cannot be explained by anything like telescope drift. The trend featured in Figure 3.7 is correlated with the hook and therefore the transfer of the detector buffer, a task performed with no relation to telescope motion.

3.5 White-Light Eclipse Curve

We wish to produce a time series of the wavelength-integrated (‘white light’) signal measured from CoRoT-2 in order to determine the amplitude and central phase of the secondary eclipse. This will yield the total signal from the planet over the G141 bandpass, while the spectrum that we calculate in Sec. 3.6 will distribute

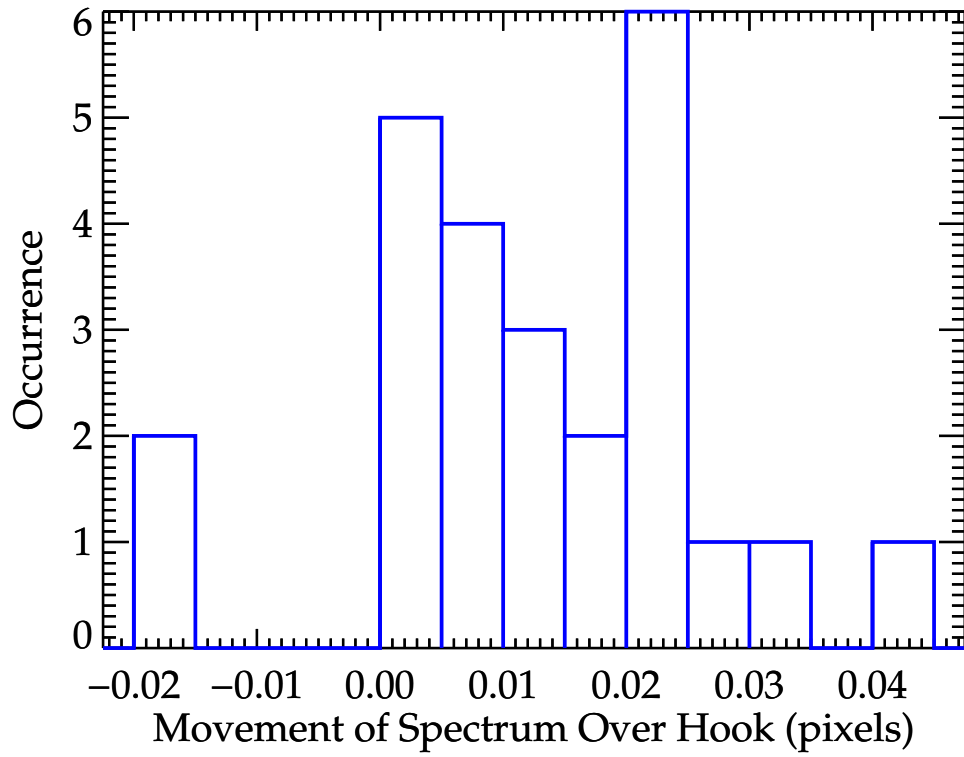


Figure 3.7 To measure any possible dependence of the hook effect on pixel row, we compared a Gaussian fit to the spectrum between the first and last observations of the hook for all iterations in the objects observed on the 128×128 subarray. We show here that the location of the maximum point of the spectrum (the peak of the Gaussian) typically moves, and typically moves in the same direction, over the course of the hook. This indicates that the hook pattern has a row dependence.

that signal as a function of wavelength. We begin with the light curves for the three visits shown in Figure 3.8, then we correct these light curves to remove the instrumental systematic effects, and we combine the three visits to form a single eclipse curve as a function of orbital phase.

[Berta et al. \(2012\)](#) successfully removed systematic effects from their dataset. The steps of their **divide-oot** method for correcting a transit/eclipse curve are as follows, assuming a five-orbit set of observations, with orbits three and four in transit:

1. Ensure that all orbits have the same number of exposures. The fifth orbit usually has fewer exposures than orbits two, three, and four, so simply repeat the last element to make up the difference. Since the hook pattern is flatter at its end, this is a reasonable approximation.
2. Create an average out-of-transit orbit by simply averaging orbits two and five.
3. Divide each orbit (two, three, four, and five) by the average orbit.
4. Remove the artificial elements that were added in the first step.
5. Fit a line to the second and fifth orbits, as there is still usually a hint of the visit-long ramp. Divide by the linear fit to normalize the data in units of the stellar flux.

This method should yield an acceptable eclipse curve with out-of-transit flux normalized to unity. Application of **divide-oot** to objects in our HST program 12181 proved successful only in some cases ([Ranjan et al., 2014](#)). A modification of

the method will be explained below.

3.5.1 Modified **divide-oot**

We observe CoRoT-2 in four orbits per visit, but each visit contains at most one orbit that is completely in-eclipse (when the planet does not contribute), and each visit contains the virtually unusable first orbit. For this reason and due to our significantly lower signal-to-noise ratio than for the [Berta et al. \(2012\)](#) planet’s observations – the GJ1214b transit depth is two orders of magnitude larger than the depth of the CoRoT-2b secondary eclipse in the same waveband and on the same grism – our CoRoT-2 data are not well-suited for the **divide-oot** method *per se*. Another issue with CoRoT-2 is the severity of the visit-long ramp, which causes trouble when trying to average pattern shapes before removing the ramp. Therefore, instead of dividing by an average *orbit*, we elect to divide by an average *pattern*, defined both by the occurrence of a buffer dump and through visual assessment, and we proceed as follows:

1. Identify the patterns that are out-of-eclipse. Divide the entire white-light curve by the median of the out-of-eclipse exposures from a single, early orbit (usually orbit 2). This normalizes the curve to unity.
2. Fit a line to the out-of-eclipse patterns, but exclude all points below intensity level 0.997. These outliers are due to the hook effect, and would bias the visit-long slope correction.
3. Divide by the fitted curve to re-normalize to unity.

4. Create an average pattern by averaging the out-of-eclipse patterns.
5. Divide each occurrence of the pattern in the entire white-light curve by the average pattern.

This creates a vast improvement in the data, with a significant reduction in the presence of systematic effects. We are also able to utilize the later patterns of the first orbit, rather than discarding it completely, as the problems presented by settling or other effects of unknown origin diminish significantly after one to two iterations of the pattern. An average pattern is plotted in the inset of Figure 3.8, and the corrected data are shown in comparison to our best-fit eclipse curve in Figure 3.9.

3.5.2 White-Light Eclipse Amplitude

With the corrected data in hand after applying our modified **divide-oot** procedure, we fit an eclipse curve using the data from our α analysis. We calculate the shape of the theoretical eclipse curve using expressions from Mandel and Agol (2002), with orbital parameters from Alonso et al. (2009), except for the orbital period where we adopt the updated value from Sada et al. (2012). In fitting the data, we vary only the central phase and amplitude of the eclipse, the latter by scaling the amplitude of the theoretical curve. We perform the fit using two χ^2 -minimization methods. First, we implement a Levenberg-Marquardt algorithm to vary the eclipse amplitude and central phase simultaneously, to find the global minimum in χ^2 . Second, we vary the central phase incrementally from 0.49 to 0.51 in steps of 10^{-5} . At

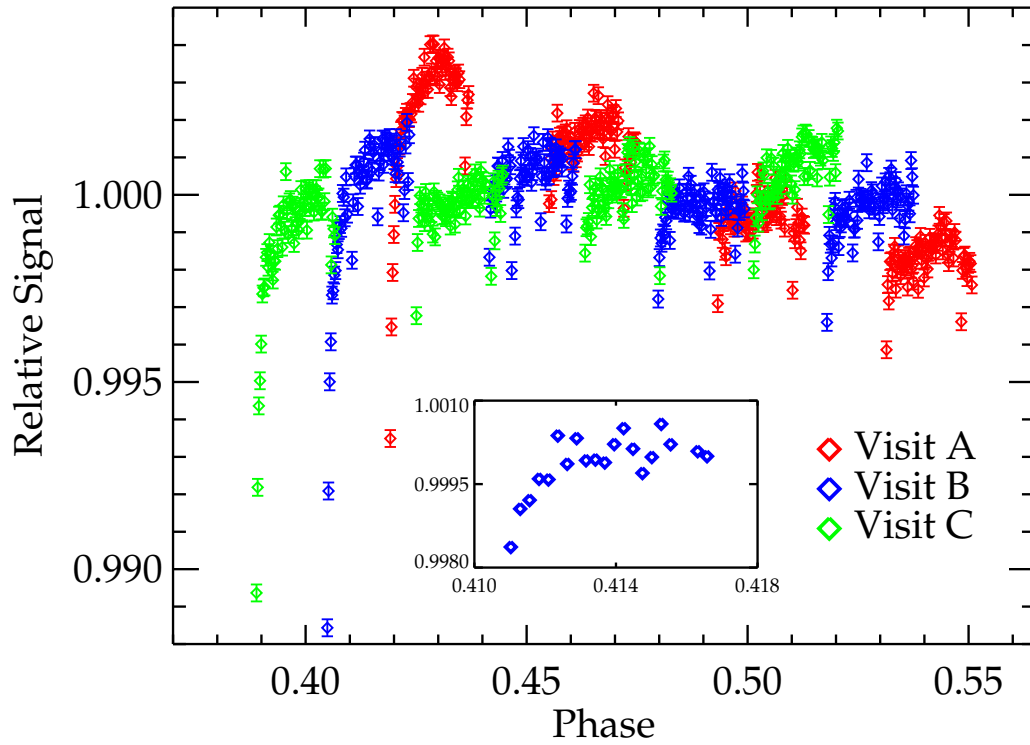


Figure 3.8 Phase plot of the wavelength-integrated flux from the three visits of CoRoT-2 before any corrections to the systematics have been applied. Visits A, B, and C are shown in red, blue, and green, respectively. *Inset:* An example of an "average pattern," of the characteristic hook shape, corresponding to visit 23 and calculated by the modified **divide-out** method described in §3.5.1. This pattern is calculated after removal of the linear visit-long ramp.

each step, we calculate the best-fit eclipse amplitude at that phase in closed form, using linear least-squares. Cycling through the range of trial central phases, we again find the global minimum χ^2 . Results from the two methods were in excellent agreement.

We find a best-fit eclipse depth of 395_{-45}^{+69} ppm (parts per million); the fit is shown in Figure 3.9. The reduced $\chi_{red}^2 = 6.60$; as it was calculated estimating the error to be Poissonian, the ideal scenario, this χ_{red}^2 value indicates that the achieved per-point scatter is 2.6 times the photon noise. The error level, and the appearance of Figure 3.9, suggests that red noise remains in the data, in spite of our modified **divide-oot** procedure. To verify the presence of red noise, we binned the residuals from the best-fit eclipse over N points per bin, and calculated the standard deviation of the binned points, σ_N . We solve for the slope of the relation between $\log(N)$ and $\log(\sigma_N)$ using linear least-squares. Poisson noise will produce a slope of -0.5 , whereas we find a slope of -0.33 ± 0.03 for the Figure 3.9 data, confirming the presence of red noise.

Given the presence of red noise in the white light eclipse data, we assign errors to the best-fit eclipse parameters (eclipse amplitude and central phase) using the residual permutation (“prayer-bead”) method (Bouchy et al., 2005; Gillon et al., 2007). Figure 3.10 shows histograms of the results for the best-fit amplitude and central phase, based on the residual permutation fits. For reference, we fit Gaussians to these histograms. A Gaussian is a reasonable approximation to the central phase histogram, but the eclipse amplitude histogram has a higher central peak, and lower wings, than does a Gaussian. Our adopted errors are equivalent to the $\pm 1\sigma$ points

in the histograms, in the sense that 15.8% of the histogram area lies beyond each quoted 1σ value (31.6% considering both ends of the range).

3.5.3 Eclipse Central Phase

Our best-fit eclipse is centered at a phase of 0.4998 ± 0.0030 . The light-travel time across the orbit is 28 seconds. The central phase for a circular orbit would be 0.50019, consistent with our result, within our errors. [Gillon et al. \(2010\)](#) found the eclipse to occur slightly earlier than expected for a circular orbit, at phase 0.4981 ± 0.0004 . ([Deming et al., 2011](#)) found a central phase of 0.4994 ± 0.0007 , weakly supporting the result from [Gillon et al. \(2010\)](#). The low signal-to-noise – due to the shallower secondary eclipse at shorter wavelengths – of the eclipse in the WFC3 bandpass contributes to a relatively large error level for the central phase (approximately 4 to 8 times larger than the Spitzer errors). Although we find good agreement with a circular orbit, we cannot exclude the result of [Gillon et al. \(2010\)](#) who concluded that the orbit is slightly eccentric.

3.6 Calculation of the Eclipse Spectrum

[Berta et al. \(2012\)](#) used his **divide-oot** method for GJ 1214b to derive the depth of transit as a function of wavelength, i.e., the transmission spectrum. In principle that method is applicable to exoplanetary spectra at secondary eclipse, but we use an alternate technique. We have at most one in-eclipse reference orbit (when the planet does not contribute) per visit. Moreover, CoRoT-2 is a relatively

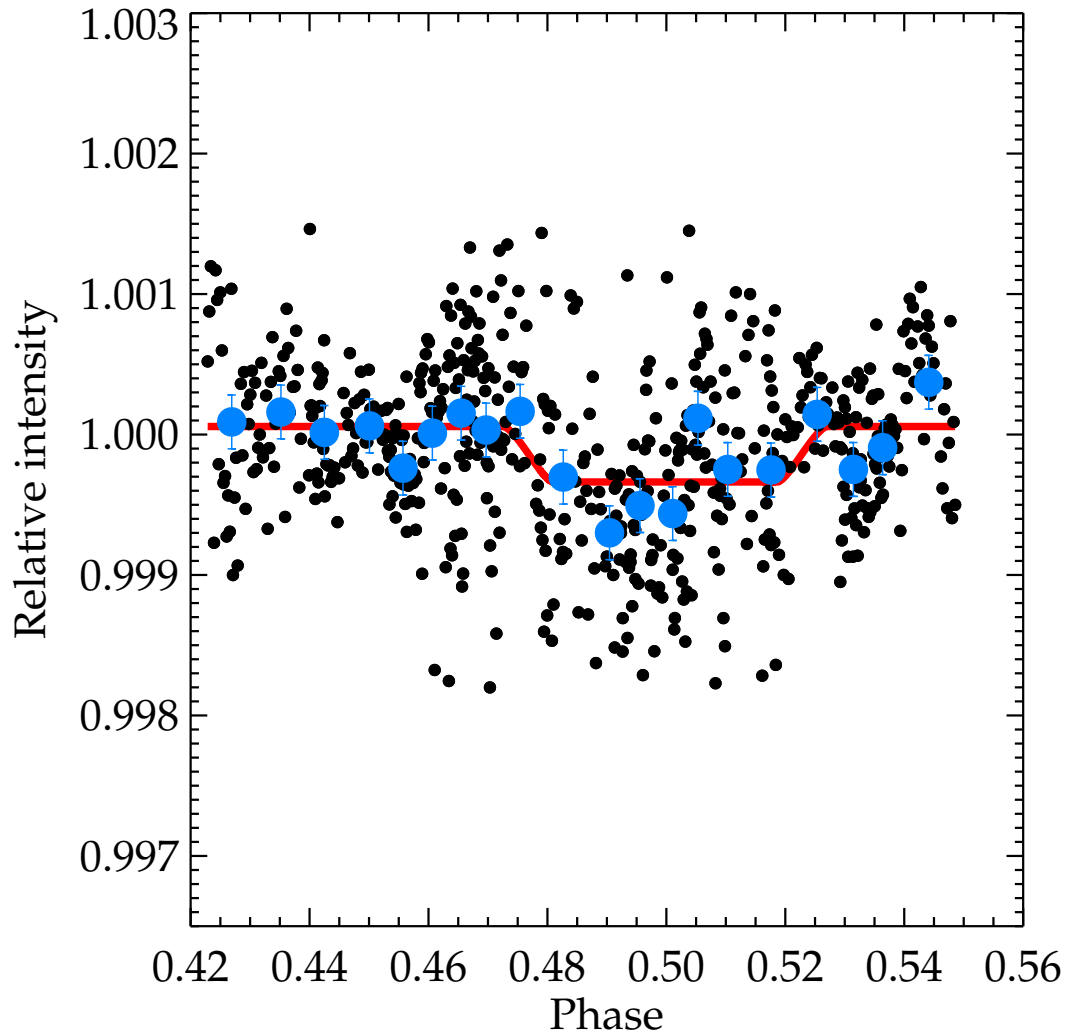


Figure 3.9 Wavelength-integrated light curve of CoRoT-2 after correction of the hook and visit-long ramps as described in section §3.5.1. The best-fit secondary eclipse curve is overplotted in red. The large points in blue represent averages over bins of 0.0063 in phase, about 15 minutes in time. The fit was performed on the actual data (black points); the binned data are shown merely for reference.

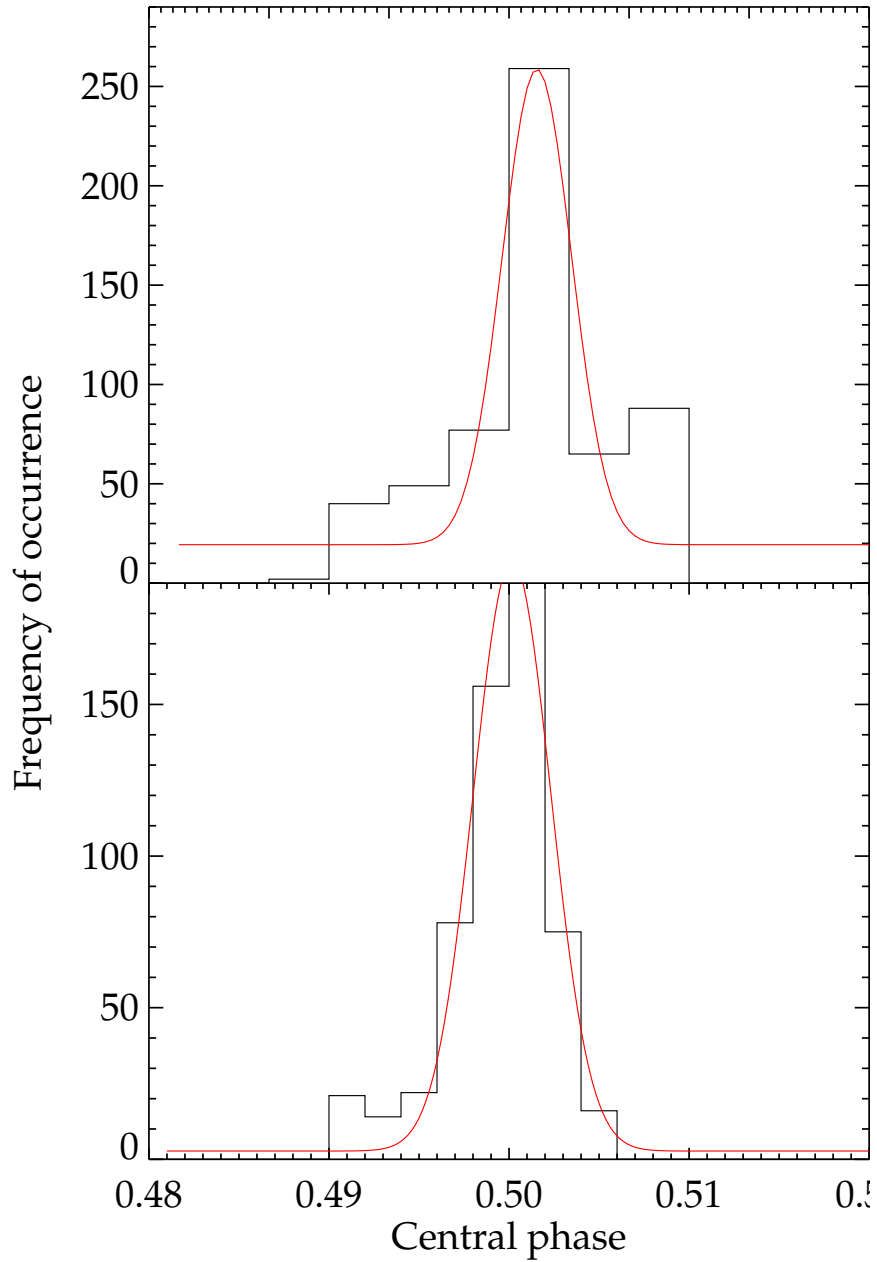


Figure 3.10 Error analysis for the amplitude and central phase of the white light eclipse. The frequency of occurrence is based on a total of 580 residual permutations. Upper panel: histogram of eclipse amplitudes in parts-per-million for the residual permutation error analysis of the eclipse amplitude. Lower panel: histogram from the residual permutation error analysis of the central phase of the eclipse.

faint star ($V=12.6$, $H=10.4$). In the faint-source limit, dividing single-wavelength data by a single reference orbit would increase the random noise in the quotient to an unacceptable degree, because we are photon-starved. To obtain the spectrum of the planet, we utilize the differential method described by [Deming et al. \(2013\)](#) and explained below. We apply this method to data from both our α and β data analyses, finding consistent results.

A by-product of this method is a time-dependent scaling factor obtained by fitting a template spectrum (see below). This scaling factor is an excellent proxy for the white light eclipse, and we find consistent results between the modified **divide-oop** and differential methods when calculating that white light eclipse. That comparison also served to verify that our α and β analyses produce consistent values for the white light eclipse depth.

3.6.1 Beyond **divide-oop**: the Differential Method

The differential method is intended to exploit the characteristics of the systematic hook pattern in order to cancel it, while also correcting for the effects of jitter in wavelength over time. The amplitude of the hook is a function of the flux level in the affected pixels (§3.4). The procedure of the differential method, in its simplest form, is to therefore extract the intensity in each column of each grism image, and divide that intensity by the wavelength-integrated intensity in the entire spectrum observed at that time. In other words, ratio the intensity in a given column on the detector (after subtracting the background, and integrating over rows) to the sum of

all columns, and we repeat this process for the grism image at each orbital phase ϕ . This ratio adds minimal noise, because the precision of the wavelength-integrated spectrum is much better than the precision of a single wavelength. Moreover, the ratio should be effective in removing the hook, as long as the wavelength used in the numerator is not too close to the edges of the grism response, where the intensity rolls-off to much smaller values, as does the hook (§3.4). The observed grism spectral intensity varies only modestly (Figure 3.1) over the 1.1-1.7 μm range of our analysis. Thus, dividing a single wavelength by the sum of all wavelengths is a comparison of similar intensity levels, so we expect much of the hook pattern to cancel, and this expectation is met by the actual data (see below).

The differential method also removes the white-light eclipse. Specifically, the eclipse shown on Figure 3.9, by summing over wavelengths, will identically cancel. However, wavelength-to-wavelength *variations* in the eclipse depth will be preserved. We call these differences *differential depths* and we derive them either positive or negative, by fitting to the wavelength-ratioed data. We then add the depth of the white-light eclipse, reconstructing the full emergent spectrum of the planet at eclipse.

In actual practice, the implementation of this differential method is more complex than the simple division implied above. We do not explicitly divide by a wavelength integral; we use an equivalent but more subtle procedure that we now describe.

We must account for possible wavelength shifts in each grism spectrum. Wavelength shifts have two effects. First, a shift of the spectrum changes the intensity in

a given column because the grism response varies with wavelength. Second, a shift in the spectrum changes the range of wavelengths sampled by a given column of the detector. We find that the wavelength shifts are of order 0.02-pixels, and they vary within an orbit, but tend to reset and exhibit a similar pattern in subsequent orbits. Given this magnitude of shifts, the second effect mentioned above - a perturbation to the wavelength assigned to a given column - has negligible effect. We therefore ignore the wavelength perturbations per se, and we use the wavelength scale from the calibration described in §3.3.3. However, the first effect (changes in grism response with wavelength) is important, and we deal with it as follows:

1. For each visit, form a “template” spectrum of the star alone by summing the in-eclipse (planet hidden) spectra. Denote this spectrum by S_x , where x is the column coordinate on the detector.
2. Fit the template to each individual spectrum by re-sampling, shifting (in steps of 10^{-4} pixels), and scaling S_x in intensity using linear least-squares. Perform this least-squares fit over a large range of shift values (± 0.1 -pixels) and choose the shift that exhibits the best fit as judged by the standard deviation of the ratio.
3. Each individual spectrum, P_x at orbital phase ϕ , matches a version of S_x with a scaling factor a : $aS'_x + b$. The prime marks the change in intensity due to the shift in x , and the zero-point constant b is negligibly small.
4. Form the ratio $R_x^\phi = \frac{P_x}{aS'_x + b}$.

An example of this basic process of shifting and fitting the template spectrum, for a randomly selected spectrum in visit C, is illustrated in Figure 3.11. However, our actual analysis adds an additional step in order to deal with the undersampling of the stellar spectrum as discussed by Deming et al. (2013). Between steps 3 and 4 above:

- 3.5. Smooth all of the spectra using a Gaussian kernel with FWHM = 4 pixels.

The choice of pixels (columns in wavelength) is dictated by the tradeoff between suppressing the undersampling, and preserving the spectral resolution.

The wavelength integrals of P_x and $aS'_x + b$ are closely equal because of the fitting process that matches them. Moreover, the shape of S_x is constant over a visit, i.e., its value at any single wavelength, relative to its wavelength integral, is constant. Hence the point-by-point division described above is conceptually equivalent to dividing a single wavelength (equivalently, x -value) in P_x by the wavelength integral of P_x . However, our procedure has the advantage that we do not have to re-sample any spectra wherein the potential signal is present, or where the reference stellar spectrum is changing. Hence we introduce no extra noise in this process, while also correcting for wavelength jitter in the spectrum.

3.6.1.1 The Spectrum of CoRoT-2b Using the Differential Method

Performing the procedure described above yields a set of ratio values R_x^ϕ for each visit. We now combine visits as follows:

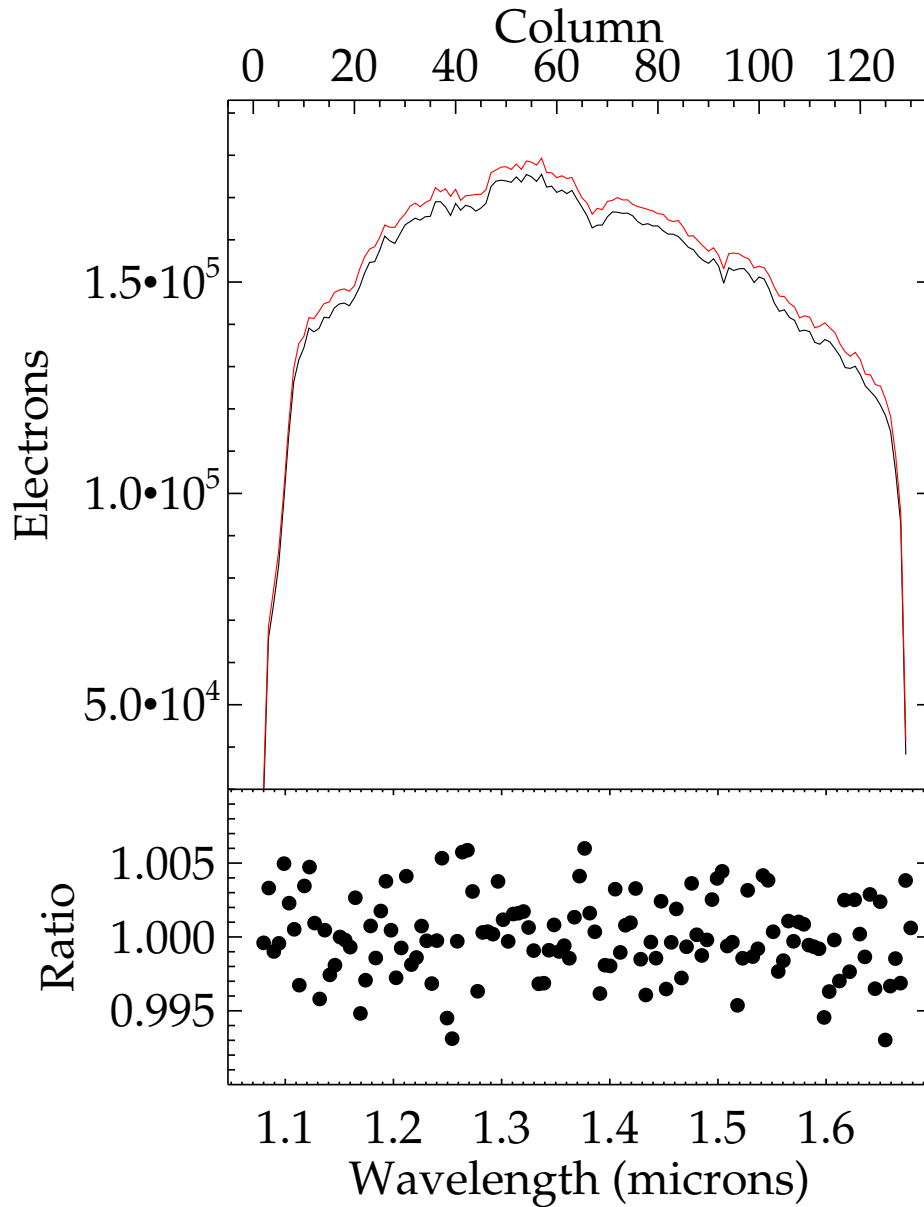


Figure 3.11 Top panel: Spectrum of the star + planet (black line) at a randomly selected time during visit A, compared with a best-fitting 'star only' spectrum (red line) constructed as an average of all of the in-eclipse spectra during visit A. (These spectra are prior to the smoothing that we employ.) The star-only spectrum was shifted in wavelength and scaled in intensity to provide the best fit to the star+planet spectrum (see text, however for this figure an additional 2% shift in intensity was added so that the two lines do not overlap). Bottom panel: ratio of the star+planet spectrum to the shifted and scaled star-only spectrum. The scatter (0.00245) is dominated by the photon noise of the spectrum in the numerator of the ratio.

1. For each column of the detector x , fit a straight line to the R_x^ϕ , where the independent variable in the linear fit is phase ϕ , and then divide by that line.

Dividing each visit by the linear fit removes any slight slopes that are present in each visit (as described by [Berta et al., 2012](#) and §3.4) and places all three visits on a common scale.

2. Fit an eclipse curve to the combined R_x^ϕ at each x , holding the central phase fixed at 0.5 for the eclipse fit, solving only for the depth.
3. Use the wavelength calibration to associate a wavelength with each column x ; R_x^ϕ becomes R_λ^ϕ .

The wavelength scale is sufficiently similar for each of the visits that we associate visit-averaged wavelengths with each x . The upper panel of [Figure 3.12](#) shows the result of fitting an eclipse curve to the visit-combined R_λ^ϕ at a randomly-selected wavelength. Because the white-light eclipse has been removed by the process used to generate the R_λ^ϕ , the differential eclipse depth at individual wavelengths can be either positive or negative depending on whether the intensity of the exoplanetary spectrum is greater or less at that wavelength compared to the average over the band defined by the grism response. Note that the scatter in the individual points on [Figure 3.12](#) is large compared to these differential eclipse depths. However, the precision of the differential eclipse depths is much better than the single-point scatter in R_λ^ϕ , and we also average adjacent wavelengths to derive spectral structure in the exoplanetary spectrum (see below).

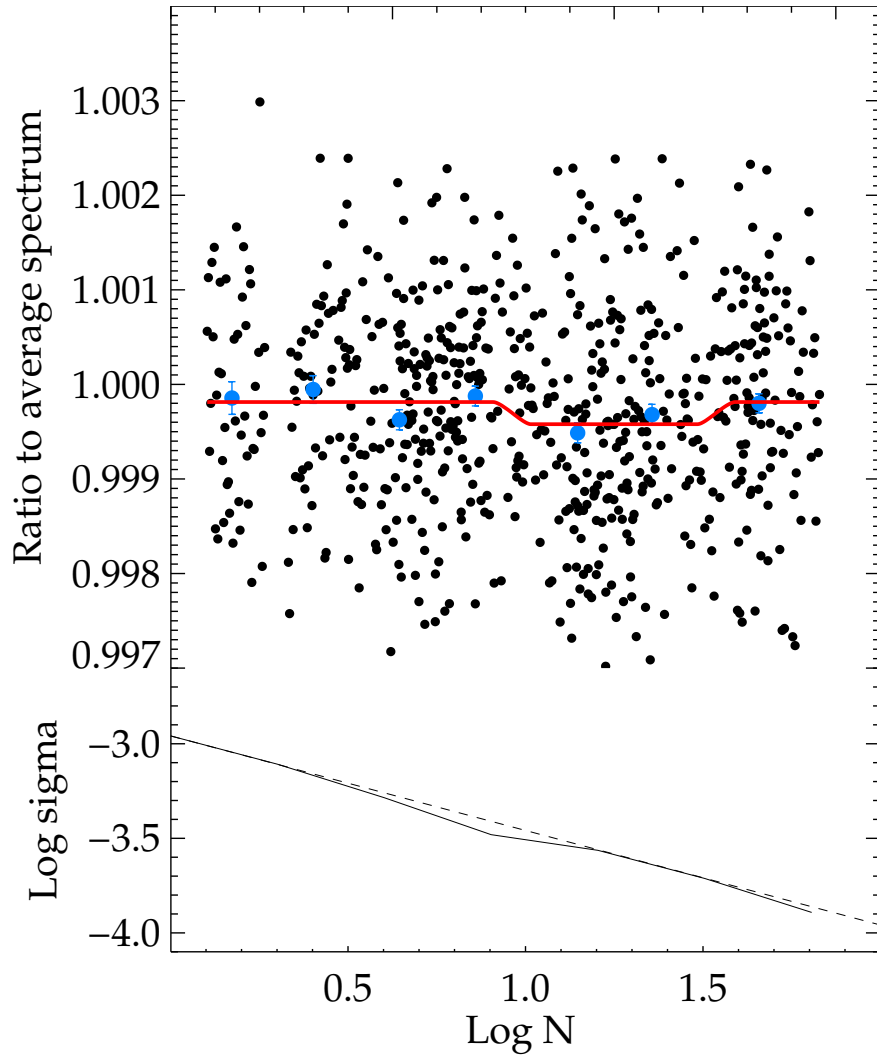


Figure 3.12 Top panel: Differential eclipse at a single randomly-selected wavelength ($\lambda = 1.551 \mu\text{m}$). Bottom panel: Log of the observed dispersion (solid line) for bins of N points, versus $\log N$. The dashed line shows the relation expected for an inverse square-root dependence, as per photon noise.

As the final step,

4. We add the white-light eclipse depth (0.000495, §3.5.2) to the differential eclipse depths, and thereby derive the planet-to-star contrast versus wavelength.

This emergent spectrum of the planet is illustrated on Figure 3.13, from both our α - and β -analyses. The upper panel shows the values for individual wavelengths, i.e., single columns of the detector, and the lower panel bins the results in bins of width $0.05 \mu\text{m}$ (4 columns).

3.6.1.2 Errors

We have estimated the errors on the differential eclipse depths using two methods. For both methods, we remove the fitted differential eclipse and examine the properties of the point-to-point scatter (Figure 3.12, top) for each wavelength. First, we bin these points using bin widths of 2, 4, 8, 16, 32 and 64 points, and we calculate the scatter in those binned values. For Poisson noise, we expect that the scatter as a function of bin size $\sigma(N)$ will decrease as $N^{-0.5}$. An example of the measured relation at a single randomly-chosen wavelength is shown in the lower panel of Figure 3.12, where the dashed line is an extrapolation from the single-point scatter using an exponent of -0.5 , and the solid line is what we calculate from the actual data. These differential data are nearly photon-limited at almost all wavelengths, and $\sigma(N)$ decreases very close to $N^{-0.5}$. We write $\sigma(N) = a\sigma(1)N^b$ and we solve for a and b . We then use that relation to calculate the expected precision for the ag-

gregate in-eclipse points and the aggregate out-of-eclipse points, and we propagate those errors to calculate the error on the differential eclipse depths.

As a check on the above error calculation, we also derive the precision of the differential eclipse directly using the residual-permutation method (Bouchy et al., 2005). Removing the best-fitting differential eclipse, we permute the residuals sequentially and add them back to the best-fit eclipse curve to make new data. Fitting to these re-cast data for all possible permutations (580 of them), we calculate the dispersion in the resultant differential eclipse depths. On average, we find that this produces excellent agreement with the first method described above. For our final spectrum and errors, we bin the results - and propagate the errors - to the same resolution (4 columns, $0.05 \mu\text{m}$) that we used as a smoothing kernel in the wavelength jitter correction.

Figure 3.13 shows the exoplanetary spectrum from our analyses at single-column resolution (top panel, only α results for illustrative purposes), and binned to a wavelength resolution of $0.05 \mu\text{m}$ (bottom panel). The error bars on the α binned spectrum in Figure 3.13 are 77 ppm on average, which is 25% greater than the photon noise. From our β -analysis, the binned spectrum is similar, and the errors average to 73 ppm (18% greater than the photon noise). The values of our binned spectra, and errors, are listed in Table 3.2.

Table 3.2. Observed Eclipse Spectra for CoRoT-2b

Wavelength (μm)	α Spectrum	Error	β Spectrum	Error
1.125	334.6	67.4	248.6	86.0
1.169	272.4	83.7	366.7	109.6
1.218	339.4	119.3	309.0	83.2
1.278	344.2	72.0	313.5	60.5
1.324	338.9	64.7	279.9	56.8
1.369	403.9	77.1	376.2	60.1
1.424	454.5	59.8	480.9	65.5
1.475	320.3	93.5	304.8	80.3
1.525	438.3	62.6	454.6	63.4
1.574	548.7	61.3	632.1	61.9
1.619	382.2	82.2	414.0	73.8

Note. — Values are in parts-per-million.

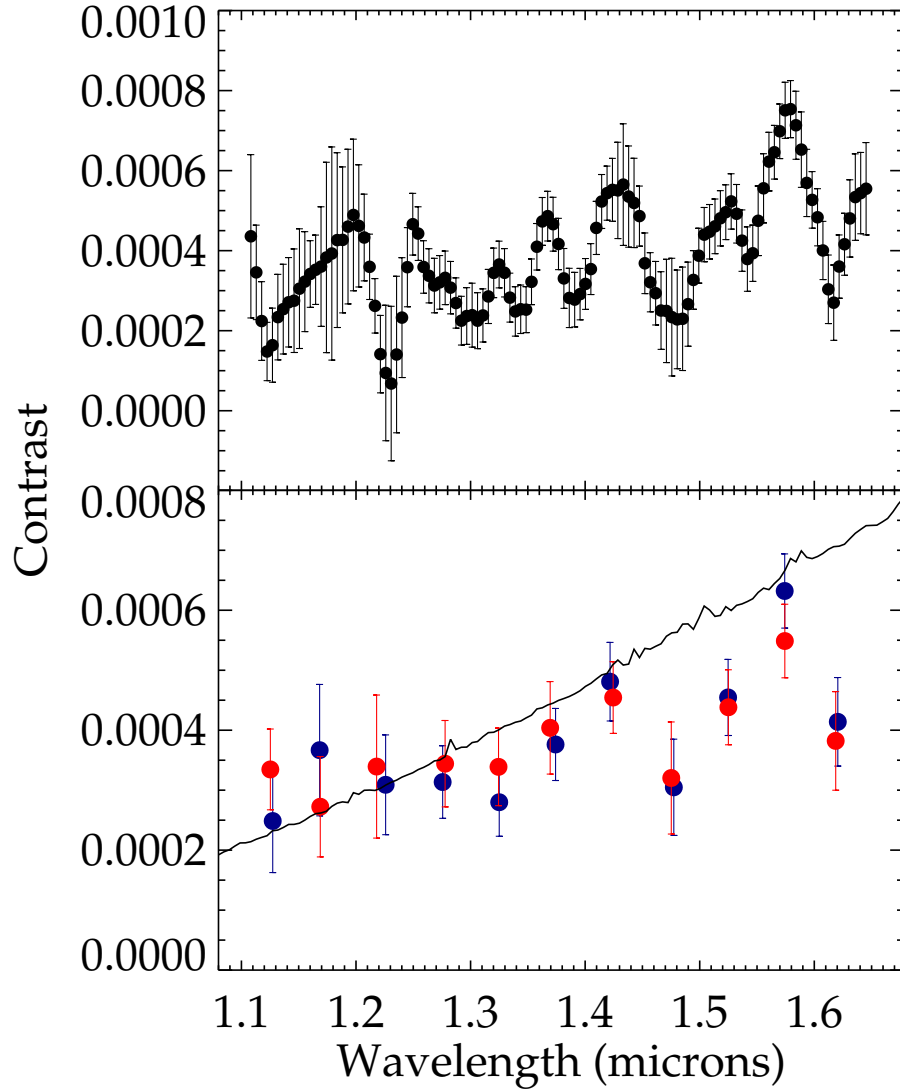


Figure 3.13 Top panel: Eclipse depth (as planet/star contrast) versus wavelength for the eclipse of CoRoT-2. Results from each detector column are plotted (from our α analysis), so the smoothing used in the wavelength shift process creates the appearance of autocorrelation. Bottom panel: Spectra of CoRoT-2b from our α (red points) and β analysis (blue points), binned to $0.05 \mu\text{m}$ (4 column) resolution. The line is a 1788K blackbody for the planet.

3.7 Implications for the Atmosphere of CoRoT-2b

No single model for the atmosphere of the planet fits all of the available data to within the errors. The observed properties of the planet’s atmosphere include: 1) the optical eclipse observed by the *CoRoT* mission (Alonso et al., 2009; Snellen et al., 2010b), 2) a ground-based eclipse near $2\ \mu\text{m}$ (Alonso et al., 2010), 3) the overall level, general slope with wavelength, and lack of obvious or known spectral features seen in our WFC3 data, and 4) eclipses in 3 Spitzer bands (Gillon et al., 2010; Deming et al., 2011). Figure 3.14 shows these data in comparison to several modeled spectra: a best-fit blackbody, conventional solar abundance models (Burrows et al., 2001, 2008a,b, 2010), and a carbon-rich model (Madhusudhan and Seager, 2009, 2010; Madhusudhan, 2012). Although none of these are ideal fits to the data, each model has characteristics that account for some observed properties of the planet, as we now discuss.

3.7.1 A Blackbody Spectrum?

The lower panel of Figure 3.13 includes the contrast produced by a best-fit blackbody for the planet compared to the results from our α and β analyses, and Figure 3.14 plots that blackbody in comparison to the totality of existing eclipse data. We adopt a Kurucz model for the star ($T_{\text{eff}}=5750$, $\log(g)=4.5$), yielding a best-fit blackbody temperature of $1788\pm 18\text{K}$ for the planet in our WFC3 band, from our α -analysis. This blackbody temperature gives acceptable agreement with the infrared eclipse results at longer wavelength (Figure 3.14). The 1788K blackbody -

derived from the WFC3 data alone - misses the ground+Spitzer eclipse amplitudes by an average of about 1.8σ . However, a blackbody spectrum for the planet does not produce the best *slope* over the WFC3 band, as we now discuss.

Our observed WFC3 spectrum for CoRoT-2b has two striking features: 1) it slopes slightly upward with increasing wavelength, and 2) it shows little to no evidence for water absorption or emission in the $1.4\ \mu\text{m}$ band. Statistically, the first question to resolve is whether the simplest possible fitting function can account for our spectrum. The simplest function is a single value in contrast, i.e. a flat line at the average contrast level. For our α analysis spectrum (red points on Figure 3.13) the χ^2 of the best-fit flat line is 12.8 for 10 degrees of freedom, so our α analysis accepts a flat line as representing the planet's contrast across the WFC3 band. For our β analysis (blue points on Figure 3.12), the flat line χ^2 is 28.6, rejecting the flat line at $> 99\%$ confidence. So our β analysis indicates a stronger and more significant upward slope than does our α analysis. That is the single largest difference between our α and β analyses, that are otherwise very consistent, with all points overlapping within their error bars (Figure 3.13). Both of our WFC3 analyses reject the best-fit blackbody slope for the planet, but only at about the 93% confidence level. The χ^2 values are 17.0 and 17.8 (10 degrees of freedom) for our α and β spectra, respectively. On the other hand, the blackbody is obviously consistent with the weakness of water absorption in the WFC3 band.

We checked that our results are not affected by inadequate corrections for detector non-linearity at the high fluence levels of our data. We repeated the β

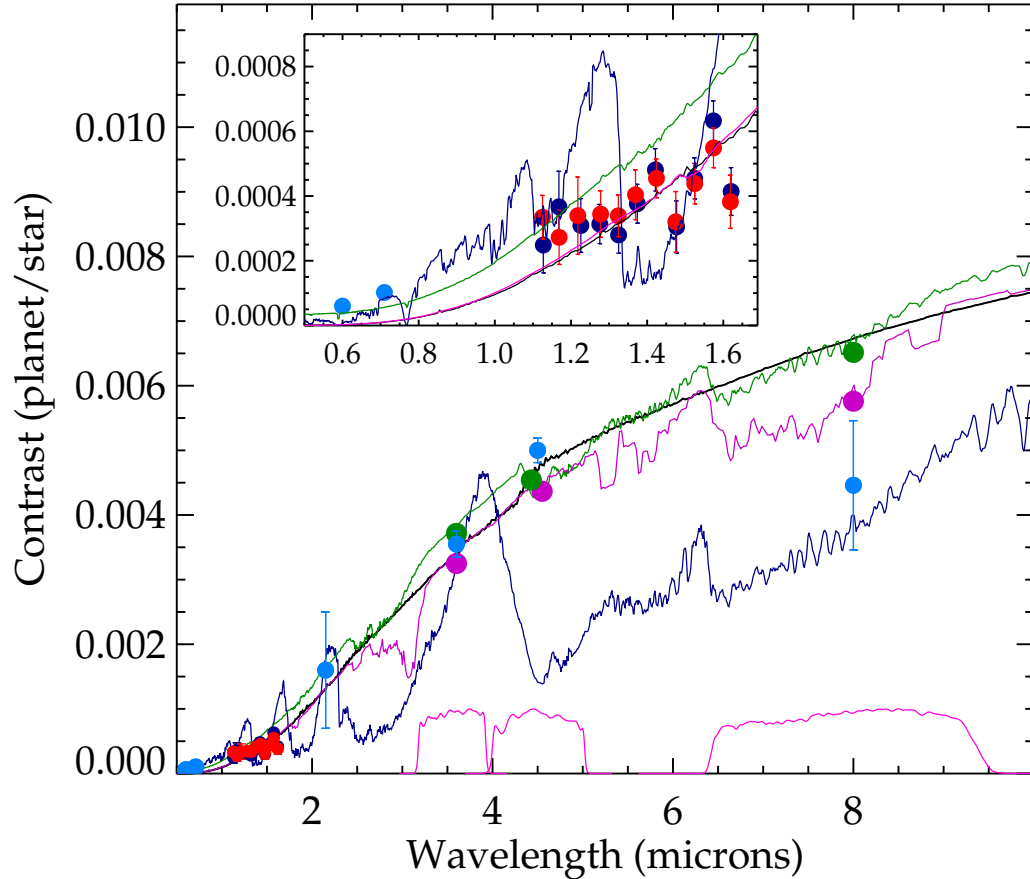


Figure 3.14 Our WFC3 results for CoRoT-2b shown in the context of ground-based $2\mu\text{m}$ results (Alonso et al., 2010), the Spitzer results from Deming et al. (2011), and the optical eclipse depths from Alonso et al. (2009). The black line is an 1788K blackbody for the planet, and the dark blue line is a solar abundance clear atmosphere Burrows model previously used to interpret the Spitzer data (Deming et al., 2011). The green line is the solar abundance Burrows model with additional continuous opacity (see text). The magenta model is from Madhusudhan and has equal carbon and oxygen abundances. All of the models lack temperature inversions (see text). The inset shows our WFC3 results, from both our α (red points) and β (blue) analyses. Note that the error in the overall level of the WFC3 points (Sec. 5.2) is much greater than the relative errors on individual points.

analysis omitting the last (fourth) sample of the exposure, and using only the first 3 samples, where the fluence level ($\sim 47,000$ electrons) is well within the linear regime. That modified version of the β analysis shows little difference from the β spectrum shown on Figs. 3.13 & 3.14 (but, with larger errors due to the lower fluence levels).

The slope of the planet's spectrum across the WFC3 band is relevant to the interpretation of the eclipse amplitude observed in the optical by CoRoT (Alonso et al., 2009; Snellen et al., 2010b). If a 1788K blackbody agreed with the slope of our observed spectrum, it would be reasonable to extrapolate that blackbody to judge the magnitude of the thermal emission from the planet at optical wavelengths. A blackbody of 1788K would produce negligible thermal emission in the optical, and we would conclude that the optical eclipses are due to reflected light. However, given that the observed slope across the WFC3 band does not decline as strongly as a 1788K blackbody, it remains possible that the optical eclipses are due to thermal emission. That could happen, for example, if temperatures on the star-facing hemisphere of the planet were spatially inhomogeneous. Hotter regions having a small filling factor, combined with cooler regions of larger filling factor, could in principle produce the observed slope across the WFC3 band, and account for the optical eclipses, while still remaining consistent with the observed contrast at wavelengths exceeding $2\ \mu\text{m}$.

In order to probe the viability of our speculation concerning temperature inhomogeneities, we performed exploratory fits (not illustrated) using two different blackbody temperatures and filling factors on the star-facing hemisphere of the planet. We find a good fit to our WFC3 and the CoRoT data using $T_1 = 1500\text{K}$ and

$T_2 = 3600\text{K}$, with filling factors of 0.96 and 0.04, respectively. This combination matches the level of the contrast in the CoRoT bands as well as the contrast level and wavelength dependence of our WFC3 results, but it significantly underestimates the contrast in the Spitzer bands (by about 0.001). Recent hydrodynamic simulations of hot Jupiter atmospheres show brightness temperature variations as large as a factor of two on the star-facing hemisphere of HD189733b (Dobbs-Dixon and Agol, 2013). Since that planet is less strongly irradiated than CoRoT-2, the temperatures found by our exploratory fits seem plausible. Nevertheless, we do not here attempt to model the atmosphere of CoRoT-2 using a self-consistent 3-dimensional approach (temperature varying with depth and with horizontal coordinate). Higher quality data, such as we anticipate from the James Webb Space Telescope, may justify such an approach in the future.

3.7.2 Limit on WFC3 Spectral Features

Both our α and β spectra agree that a straight line (contrast increasing linearly with wavelength) gives a good account of our results across the WFC3 band: the χ^2 values for a linear fit (9 degrees of freedom) are 6.1 and 13.7 for our α and β spectra, respectively. These values leave little room for absorption or emission by water vapor at $1.4\ \mu\text{m}$. In order to specify a limit on the degree of water absorption or emission, we scale and fit a Burrows model to the data, using the model shown in blue on Figure 3.14. In order to make the limit responsive to the modulation caused by the actual water absorption (as opposed to the slope of the continuum),

we allow for a linear baseline difference as a function of wavelength. We construct 10,000 trial data sets, adopting the error at each binned wavelength from our β -analysis, and we fit the model plus a linear baseline to each trial data set using linear regression. Based on the distribution of fitted amplitudes, we find an 85 ppm 3σ limit on the amplitude of water absorption or emission, measured at the bandhead at $1.38\ \mu\text{m}$. This limit assumes that the shape of the water absorption is the same as in the Burrows model. The 3σ limit of 85 ppm is significantly less than the already weak water absorption seen during transmission spectroscopy of the giant planets XO-1b and HD 209458b (Deming et al., 2013), WASP-19 (Huitson et al., 2013; Mandell et al., 2013), and HAT-P-1b (Wakeford et al., 2013). This conclusion is significant, as can be seen by reference to one conventional solar abundance Burrows model (Burrows et al., 2001, 2008a,b, 2010) illustrated as the dark blue line on Figure 3.14. This model is not intended as a fit to the WFC3 data, but it was invoked by Deming et al. (2011) in an attempt to account for the Spitzer observations. Although it misses the $4.5\ \mu\text{m}$ Spitzer point, Deming et al. (2011) discussed the possibility of circumplanetary carbon monoxide emission in that band, due to tidal stripping by the star. However, this model produces a much larger spectral modulation in the WFC3 band than is seen in our observed spectra.

3.7.3 Solar Abundance Model Atmospheres

CoRoT-2b is an unusual planet, and the Spitzer data have been particularly difficult to understand, as discussed by Deming et al. (2011) (but, see Madhusud-

han, 2012). The relatively high contrast at 3.6- and 4.5 μm seems to require a hot continuum, allowing little if any molecular (principally water) absorption. Simultaneously, the lower contrast at 8 μm requires absorption to a significant degree. We here explore the potential for conventional solar abundance model planetary atmospheres to account for the totality of the CoRoT-2b eclipse data.

The weakness of absorption features can be produced in a solar abundance model by adding continuous opacity by small particle scattering and/or absorption. That could dampen features in the emergent spectrum at short wavelengths, but a reduced scattering cross-section with increasing wavelength could allow greater spectral contrast at 8 μm (mentioned by Deming et al., 2011). If the temperature remains nearly constant as a function of pressure/altitude in the planet’s atmosphere, that would also suppress any absorption or emission features in the emergent spectrum. Figure 3.14 shows the contrast from a Burrows model (Burrows et al., 2001, 2008a, 2010) having three additional sources of opacity not present in a clear atmosphere. This model is shown in green on Figure 3.14, and has redistribution parameter $P_n = 0.1$ (Burrows et al., 2008a). The additional opacity sources are first, a high altitude optical (0.4-1.0 μm) absorber of opacity $0.2 \text{ cm}^2 \text{ g}^{-1}$. Second, an absorbing haze opacity of $0.04 \text{ cm}^2 \text{ g}^{-1}$ uniformly distributed at all pressures and wavelengths, and third, a scattering opacity of $0.08 \text{ cm}^2 \text{ g}^{-1}$ also uniformly distributed at all pressures and wavelengths. The scattering opacity acts to increase the reflected light, but not increasing the thermal emission. Note that in principle we could include a wavelength dependence to the opacity of the broadly distributed hazes, but we prefer to keep this *ad hoc* opacity as simple as possible.

The uniformly distributed hazes damp the spectral modulation in the WFC3 bandpass to an acceptable degree, but the model misses the overall WFC3 contrast level, being too high by 161 ppm. Like all single-spatial-component models, its slope across the WFC3 band is larger than our data. Given the error level of our white light eclipse (395_{-45}^{+69} ppm), the overall contrast difference is significant at 2.3σ , which is the single largest problem with this model. On the other hand, the scattering opacity increases the contrast in the optical to the point where it underestimates the *CoRoT* eclipse amplitude by less than 2σ . Also, among the models we've tested, it does the best job of reproducing the long wavelength eclipse amplitudes (1.5σ on average).

The aggregate eclipse data are ambiguous concerning the possibility of a thermal inversion in the dayside atmosphere of CoRoT-2b. As discussed in [Madhusudan \(2012\)](#), the lower brightness temperature in the $8\ \mu\text{m}$ Spitzer bandpass compared to the brightness temperatures in the shorter wavelength channels (except $4.5\ \mu\text{m}$) suggests a temperature profile decreasing outward in the atmosphere. If that gradient is flatter than radiative equilibrium models predict, it will help to account for the lack of strong spectral features. On the other hand, the solar abundance radiative equilibrium model (green line on Figure 3.14) achieves good agreement with the $4.5\ \mu\text{m}$ Spitzer eclipse depth by incorporating $0.2\ \text{cm}^2\text{g}^{-1}$ of extra optical-wavelength opacity at low pressures (~ 1 mbar) close to where radiation in the $4.5\ \mu\text{m}$ band is formed ([Burrows et al., 2007](#)). Indeed, that model shows a temperature rise of about 75 Kelvins, near 0.2 mbars. But due to the more widely distributed absorbing haze, the temperatures in this model at high altitude are al-

ready hundreds of Kelvins over the values they would have in a clear atmosphere. To the extent that this model is preferred, or that a flattened temperature gradient counts as a weakly-inverted atmosphere, then CoRoT-2b could be claimed to have a temperature inversion. However, this evidence for an inversion is weaker than for HD 209458b (Burrows et al., 2007; Knutson et al., 2008), and is ambiguous in the sense that the atmosphere could be heated without satisfying a strict definition of inversion (temperature increasing with height). Knutson et al. (2010) hypothesized that planets orbiting active stars will not have strong atmospheric temperature inversions, because the absorbing species that causes the inversion (e.g., Hubeny et al., 2003; Fortney et al., 2008) may be destroyed by the enhanced UV flux from stellar activity. CoRoT-2a is an active star (Guillot and Havel, 2011), and lack of a strong thermal inversion in CoRoT-2b would support the Knutson et al. (2010) hypothesis.

3.7.4 A Carbon-rich Model Atmosphere

An alternate way to reduce the spectral modulation by water vapor in the WFC3 bandpass is to reduce the equilibrium water vapor mixing ratio, for example by increasing the carbon abundance relative to oxygen. This also helps to decrease absorption in the 3.6- and 4.5 μm bands (although methane does contribute some absorption at 3.6- μm), while preserving absorption at 8 μm via the 7.8 μm methane band. We used the methodology described by Madhusudhan and Seager (2009) and Madhusudhan and Seager (2010) to find a possible carbon-rich match to the aggregate data for this planet (except for the optical eclipses). Madhusudhan (2012)

discussed CoRoT-2b and was able to fit the pre-WFC3 data by varying the C/O ratio to various degrees. The magenta line on Figure 3.14 is a model with an enhanced carbon abundance (C/O=1), and having a non-inverted atmosphere with modest thermal contrast (700K increase in temperature from upper boundary to the optically thick photosphere). The enhanced carbon abundance weakens the water absorption, but allows sufficient absorption near $8\mu\text{m}$ to account for that Spitzer point to within $\sim 1\sigma$. The average agreement with the ground+Spitzer eclipses is 1.9σ , not quite as good as the blackbody and the solar abundance model. On the other hand, the carbon-rich model does the best job – of the atmospheric models, i.e., beyond just a linear fit – of reproducing the WFC3 spectrum ($\chi^2 = 16.1$ for 10 DOF), and in particular it agrees essentially perfectly with the amplitude of the WFC3 white-light eclipse. It does not require additional haze opacity.

3.7.5 Reprise of the Model Atmosphere Comparisons

We here summarize the main conclusions from comparing the aggregate eclipse data for this planet with emergent spectra from different models. We tested a blackbody, as well as more sophisticated solar abundance and carbon-rich models. No model fits all of the data. The limit on spectral modulation due to water absorption in the WFC3 band is our main observational result. Given the lack of clear and unequivocal molecular absorption features in the WFC3 and other bands, emergent spectra more sophisticated than a blackbody are unproven. A blackbody spectrum gives an acceptable fit to the data except for the optical eclipses as seen by *CoRoT*. A

blackbody spectrum fits the slope over the WFC3 band poorly, but multi-component blackbodies due to spatial inhomogeneities on the star-facing hemisphere have the potential to help account for the observations, including the optical eclipses as seen by *CoRoT*, especially if extra scattering opacity increases toward short wavelengths. Note that the absorbing and scattering hazes invoked in our solar abundance model are qualitatively similar to extra absorption and scattering opacity inferred for the archetype planet HD 189733b (Pont et al., 2013; Evans et al., 2013).

Although a blackbody spectrum reasonably accounts for the infrared eclipse data, it is not a model of the planet’s atmosphere *per se*. Instead, the planetary atmosphere can mimic a blackbody via the presence of extra continuous opacity that damps the observed thermal contrast, or due to a high carbon abundance that weakens the bands of the principal molecular absorber (water vapor). In either case, extra scattering opacity at optical wavelengths could help to account for the amplitude of the optical eclipses. We find only weak evidence for a strong temperature inversion, but extra absorbing opacity in the solar abundance model would perturb the temperature profile in a manner similar to a temperature inversion, but less extreme.

3.8 Summary

We observed the Very Hot Jupiter CoRoT-2b in secondary eclipse using three visits by the WFC3 G141 grism on HST. Even without utilizing the new spatial scan mode, we obtained spectra with errors approaching the photon noise limit. We

characterized the instrument-related systematic effects present in the data. We find a time-dependent variation in the background intensity, a visit-long slope, slopes associated with each orbit, and we investigate the ‘hook’ effect that occurs after data transfers. We explored the behavior, dependencies, and how best to account for these effects in data analyses. In particular, we defined the amplitude of the hook effect versus the exposure level in electrons (Figure 6).

We measure the thermal emission from the planet in the 1.1-1.7 μm band, but we find no spectral features to a 3σ limit of 85 ppm. We used a differential method to derive the spectrum and cancel the systematic errors (Deming et al., 2013), obtaining results close to photon-limited. No model fits all available eclipse data for this planet to within the errors. We consider solar abundance and carbon-rich spectral models, as well as a simple blackbody spectrum, to account for the eclipse data. The spectral models do not clearly surpass the blackbody spectrum in terms of the quality of the fit. The slope of the data within the WFC3 bandpass is less than given by all of the models, including the best-fit blackbody. There is weak and ambiguous evidence that the atmospheric temperature structure is inverted, but a reduced temperature gradient may be present, and may help to mimic the quasi-blackbody nature of the emergent spectrum. Extra atmospheric continuous opacity is a strong possibility to account for the lack of spectral features in the WFC3 band. If that opacity has a scattering component, it can help to account for the optical eclipse amplitude of this planet as observed by CoRoT. Spatial inhomogeneities in temperature on the star-facing hemisphere may also help to account for the optical eclipse and the slope of the spectrum in the WFC3 band.

Chapter 4: Searching For Rapid Orbital Decay of WASP-18b

Abstract

The WASP-18 system, with its massive and extremely close-in planet, WASP-18b ($M_p = 10.3M_J$, $a = 0.02$ AU, $P = 22.6$ hours), is one of the best known exoplanet laboratories to directly measure Q' , the modified tidal quality factor and proxy for efficiency of tidal dissipation, of the host star. Previous analysis predicted a rapid orbital decay of the planet toward its host star that should be measurable on the time scale of a few years, if the star is as dissipative as is inferred from the circularization of close-in solar-type binary stars. We have compiled published transit and secondary eclipse timing (as observed by WASP, TRAPPIST, and Spitzer) with more recent unpublished light curves (as observed by TRAPPIST and HST) with coverage spanning nine years. We find no signature of a rapid decay. We conclude that the absence of rapid orbital decay most likely derives from Q' being larger than was inferred from solar-type stars, and find that $Q' \geq 1 \times 10^6$, at 95% confidence; this supports previous work suggesting that F-stars, with their convective cores and thin convective envelopes, are significantly less tidally dissipative than solar-type stars, with radiative cores and large convective envelopes.

4.1 Introduction

The discovery of WASP-18b (Hellier et al., 2009; Southworth et al., 2009), with its large mass ($10.3 M_J$) and small orbit (22.6 hours) (see Table 4.1 for other parameters), elicited one primary question: how could it exist? A planet of that mass and proximity should raise a substantial tidal distortion (tidal bulge) in the central star. Because the star is not a perfectly elastic body, and because the planet orbits more quickly than the star rotates, the tidal bulge would lag behind the planet, causing the planet’s orbital motion to accelerate and the orbit to shrink (Goldreich and Soter, 1966). Hellier et al. (2009) calculated a 0.65 Myr future lifetime for the planet, assuming that the star is as dissipative as is inferred from the circularization of close solar-type binary stars (Meibom and Mathieu, 2005; Ogilvie and Lin, 2007). The estimated age of the star is a few hundred million years (Bonfanti et al., 2016; Hellier et al., 2009) to 2 Gyr (Southworth et al., 2009); finding a planet with a lifetime that is such a small fraction of the system’s age is extremely improbable. Hamilton (2009) discusses several alternative explanations, ranging from an overestimation of the decay rate (due to unmodeled nuances of tidal physics leading to an underestimation of the tidal Q’ parameter) to a non-tidal mechanism holding the planet in place (e.g. influence of another body in the system). Barker and Ogilvie (2009) investigate the efficiency of tidal dissipation in the convective envelopes of F-stars, which have both convective cores and convective envelopes; G stars, on which most studies of exoplanetary tidal decay focus (e.g. Jackson et al. 2009; Birkby et al. 2014), have radiative cores and thicker convective envelopes. The

[Barker and Ogilvie \(2009\)](#) calculations reveal that tidal dissipation within F stars is generally much less efficient than within G-stars, and therefore that planetary tidal decay around stars like WASP-18 would be imperceptibly low over a decadal timespan ([Barker and Ogilvie, 2010](#); [Barker, 2011](#)). If, however, tidal dissipation within WASP-18 behaved as is usually inferred for solar-type stars, [Birkby et al. \(2014\)](#) predict that its transit should occur progressively earlier at each observation, accumulating to a measurable shift of nearly six minutes over ten years. This is the largest predicted shift of any planet, making the WASP-18 system possibly the best known laboratory for direct measurements of the stellar tidal Q' parameter. [Maciejewski et al. \(2016\)](#) potentially measured the tidal decay of WASP-12b, but [Hoyer et al. \(2016\)](#) ruled out the orbital decay of WASP-43b proposed by [Jiang et al. \(2016\)](#).

In this Letter, we bring together published measurements of transit and secondary eclipse timing from discovery ([Hellier et al., 2009](#)), *Spitzer* ([Nymeyer et al., 2011](#); [Maxted et al., 2013](#)), and ground-based TRAPPIST ([Maxted et al., 2013](#)) observations, and new analyses of unpublished archival (HST), and recent TRAPPIST data. We place strong limits on the maximum rate of the system's orbital decay and discuss the implications.

Table 4.1. WASP-18 parameters used for this analysis.

Parameter	Value	Average	Reference
The Star: WASP-18			
Radius (R_{\odot})	1.29 ± 0.16		Doyle et al. 2013
		1.22 ± 0.11	
T_{eff} (K)	1.15 ± 0.02		Bonfanti et al. 2016
	6400 ± 100		Hellier et al. 2009
	6400 ± 75	6322 ± 72	Doyle et al. 2013
$\log g$	6167 ± 7		Bonfanti et al. 2016
	4.4 ± 0.15		Hellier et al. 2009
	4.32 ± 0.09	4.32 ± 0.10	Doyle et al. 2013
Age (Gyr)	4.39 ± 0.01		Bonfanti et al. 2016
	< 2.0		Southworth et al. 2009
	$0.5 - 1.5$		Hellier et al. 2009
M_* (M_{\odot})	0.9 ± 0.2		Bonfanti et al. 2016
	$1.281^{+0.052}_{-0.046}$		Southworth et al. 2009
	1.24 ± 0.04	1.25 ± 0.04	Triaud et al. 2010
	1.22 ± 0.03		Enoch et al. 2010
The Planet: WASP-18b			
P (days)	$0.94145299 \pm 8.7 \times 10^{-7}$		Hellier et al. 2009
a (AU)	$0.02047^{+0.00028}_{-0.00025}$		Southworth et al. 2009
		$0.02034^{+0.00026}_{-0.00023}$	
	$0.02020^{+0.00024}_{-0.00021}$		Triaud et al. 2010
	86 ± 2.5		Hellier et al. 2009

Table 4.1 (cont'd)

Parameter	Value	Average	Reference
i ($^{\circ}$)		$83.3^{+1.9}_{-2.0}$	
		$80.6^{+1.1}_{-1.3}$	Triaud et al. 2010
M_p (M_J)		$10.43^{+.30}_{-.24}$	Southworth et al. 2009
		$10.11^{+.24}_{-.21}$	Triaud et al. 2010

4.2 New Observations

4.2.1 TRAPPIST

The TRAnsiting Planets and PlanetesImals Small Telescope-South (TRAPPIST-S, [Jehin et al. 2011](#); [Gillon et al. 2011](#)) is a ground-based, 60-cm robotic telescope based at the La Silla Observatory used to study both exoplanets and small bodies in the Solar System. TRAPPIST observed two WASP-18b photometric transits in the fall of 2015 in the broad-band Sloan-z filter, centered at $0.9134 \mu\text{m}$.

4.2.2 *Hubble Space Telescope*

The *Hubble Space Telescope* (HST) observed WASP-18b in 2014 in spatial scan mode ([Deming et al., 2013](#)) over its full phase (PID 13467, PI Bean), including one full transit, one full secondary eclipse, and one extra eclipse ingress. All observations were made with the Wide Field Camera 3 (WFC3) G141 infrared grism, covering

1.1 - 1.7 μm . While the primary deliverable from such observations is the spectrum, we sum over wavelength to extract a photometric light curve. To maximize observing efficiency, the scan reverses direction, rather than taking the time to reset to the starting point, at the end of each scan. This introduces a non-constant offset requiring separate analysis of the forward and reverse scans.

4.3 Analysis: Deriving the new White Light Curves

Table 4.2 includes the transit and secondary eclipse times used in this analysis. We describe here how we generated white light curves and transit fits to the new TRAPPIST and HST data.

4.3.1 TRAPPIST Light Curves

We reduce our TRAPPIST data in the methods described by Gillon et al. (2012). We calculated the best-fit transit curve for each observation using the TRAPPIST MCMC procedure (Gillon et al. 2009 and references therein), executing the Mandel and Agol (2002) algorithm to find the new best-fit light curve parameters. We generated the curve plotted in Figure 4.1 with the BATMAN procedure (Kreidberg, 2015), given those orbital parameters.

Table 4.2. WASP-18 Full Observation Summary

Facility	Date	Original Reference(s)	Orbit	BJD (TDB)
WASP	May - December 2006	Hellier et al. (2009)	0	$2454221.48163 \pm 0.00038$
Spitzer	December 20, 2008	Nymeyer et al. (2011) Maxted et al. (2013)	636.5	2454820.7168 ± 0.0007
Spitzer	December 24, 2008	Nymeyer et al. (2011)	640.5	2454824.4815 ± 0.0006
		Maxted et al. (2013)	640.5	2454824.4815 ± 0.0006
Warm <i>Spitzer</i>	January 23, 2010	Maxted et al. (2013)	1061.5	2455220.8337 ± 0.0006
Warm <i>Spitzer</i>	January 24, 2010	Maxted et al. (2013)	1062	2455221.3042 ± 0.0001
Warm <i>Spitzer</i>	August 23, 2010	Maxted et al. (2013)	1285.5	2455431.7191 ± 0.0003
Warm <i>Spitzer</i>	August 24, 2010	Maxted et al. (2013)	1286	2455432.1897 ± 0.0001
TRAPPIST	September 30, 2010	Maxted et al. (2013)	1327	2455470.7885 ± 0.00040
TRAPPIST	October 2, 2010	Maxted et al. (2013)	1330	2455473.6144 ± 0.00090
TRAPPIST	December 23, 2010	Maxted et al. (2013)	1416	2455554.5786 ± 0.00050
TRAPPIST	January 8, 2011	Maxted et al. (2013)	1433	$2455570.5840^{+0.00045}_{-0.00048}$
TRAPPIST	November 11, 2011	Maxted et al. (2013)	1758	2455876.5559 ± 0.0013
HST	April 22, 2014	This work	2840.5	2456895.6773 ± 0.0006
HST	April 22, 2014	This work	2841	2456896.1478 ± 0.0008
TRAPPIST	August 20, 2015	This work	3223	$2457255.7832^{+0.00030}_{-0.00029}$
TRAPPIST	October 21, 2015	This work	3291	$2457319.8010^{+0.00039}_{-0.00038}$

Note. — Transit (whole number cycles) and secondary eclipse (half-integer cycles) central times used and/or calculated in this work. Orbit corresponds to number of orbits since the discovery ephemeris, and BJD (TDB) is the best-fit time for the center of the transit or secondary eclipse.

4.3.2 HST White Light Curves

As has been studied extensively (e.g. [Sing et al. 2016](#)), the HST WFC3 camera, while improved over its predecessor NICMOS, has persistent systematic errors that seem to be a function of incident flux ([Wilkins et al., 2014](#)), with three distinctive effects: a visit-long ramp, an orbit-long ramp, and a “hook” within orbits ([Berta et al., 2012](#); [Wilkins et al., 2014](#)). We reduce the WFC3 data and mitigate systematics in a modified divide-out method – a method of averaging out all three systematic effects ([Wilkins et al., 2014](#); [Deming et al., 2013](#)), including the correction to the STScI wavelength calibrations found in [Wilkins et al. \(2014\)](#). To fit the transit, we use the non-linear, fourth-order limb darkening coefficients from [Claret \(2000\)](#) in the [Mandel and Agol \(2002\)](#) light curve models, and derive “prayer-bead” error bars as in [Gillon et al. \(2009\)](#). To fit the secondary eclipse, we use the same procedure in the limit of no limb darkening, such that the shape is that of a trapezoid. We analyze the forward and reverse scans independently, as mentioned in § 4.2, due to a non-linear offset between the two; the final timing results agree and are thus shown as an average in the table.

4.4 Results: Transit Timing Evolution over Nine Years

We have compiled all published transit and secondary eclipse observations of WASP-18b and added them to the new observations obtained by HST and TRAPPIST to produce a data set spanning more than nine years. The full data set is found in Table 4.2. Published light curve solutions came from four observing campaigns:

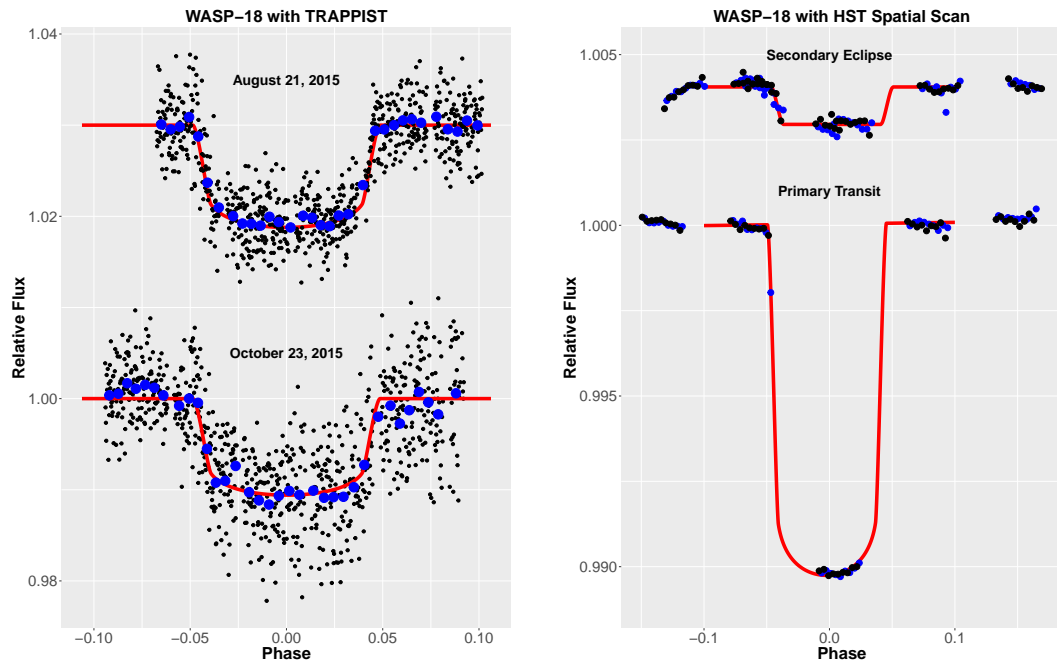


Figure 4.1 *Left*: Two new transits of WASP-18 by its planet observed by TRAPPIST in 2015. The data are plotted in black, binned points in blue, and the best-fit transit curve in red. The August observation is offset in y for visualization purposes. *Right*: New transit and secondary eclipse of WASP-18 by its planet observed by HST in 2014. The data are plotted in black and blue (forward and reverse scans), the best-fit transit curve in red.

WASP: The Wide-Angle Search for Planets (WASP) Project (Pollacco et al., 2006) announced the discovery and initial orbital solution of WASP-18b as observed in transit by the WASP-South Survey and in radial velocity with the CORALIE spectrograph (Hellier et al., 2009), and confirmed with the Danish 1.5m telescope at ESO (Southworth et al., 2009). The Southworth et al. (2009) ephemeris was later found to be erroneous (Southworth et al., 2010); we use only the Hellier et al. (2009) ephemeris.

Spitzer: Nymeyer et al. (2011) observed two secondary eclipses of WASP-18b via the *Spitzer* Exoplanet Target of Opportunity Program with the Infrared Array Camera (IRAC, PID 50517). The first secondary eclipse was observed in the 3.6 μm and 5.8 μm channels on December 20, 2008, the second in the 4.5 μm and 8.0 μm channels on December 24, 2008. Maxted et al. (2013) reanalyzed the Nymeyer et al. (2011) points.

Warm Spitzer: Maxted et al. (2013) observed two full phases of WASP-18b's orbit with warm *Spitzer*, one with the 3.6 μm channel on January 23, 2010, and the other with the 4.5 μm channel on August 23, 2010.

TRAPPIST: In addition to the unpublished, new transit curves presented as part of this work, TRAPPIST also observed WASP-18b five times in transit in late 2010 and early 2011, also in the Sloan-z' filter Maxted et al. (2013).

To search for tidal decay, we study the correlation between the number of orbits since discovery ephemeris and transit (or eclipse) arrival time. In the case of no orbital evolution, this correlation would be linear, and the slope of the line would be the planetary orbital period. We allow for the possibility of decay by including

a second-order term that is dependent on the rate of any orbital evolution. We first perform a multivariate linear regression and find a plausible fit ($\chi^2_{RED} = 1.07$). To explore the trade-off between the linear and quadratic terms of the fits, we also perform a Markov Chain Monte Carlo (MCMC) quadratic fit using *emcee* (Foreman-Mackey et al., 2013); the results of both fits, which are in excellent agreement, are in Figure 4.2. With *emcee*, we find the period $P = 0.94145287^{+6.56 \times 10^{-7}}_{-6.59 \times 10^{-7}}$ days, in agreement with the Hellier et al. 2009 $P = 0.94145299 \pm 8.7 \times 10^{-7}$ days. If WASP-18 were as tidally dissipative as is inferred from the circularization of solar-type close binary stars, there should be a definitive deviation from linear behavior, i.e., the quadratic term should be nonzero. We measure an upper limit for the magnitude of the quadratic term, and we therefore find no confirmation of rapid tidal decay for the WASP-18 system. Indeed, as discussed in the next section, we should not have expected to find evidence of rapid decay.

4.5 Discussion: Implications of the Absence of Rapid Tidal Decay

Without strong evidence of a rapidly decaying orbit suggested by Hellier et al. (2009); Birkby et al. (2014), we turn instead to the predictions of Barker and Ogilvie (2009, 2010); Barker (2011); Lanza et al. (2011). We first briefly review the discussion of these predictions as they apply to WASP-18, and then calculate a constraint on the Q' of WASP-18.

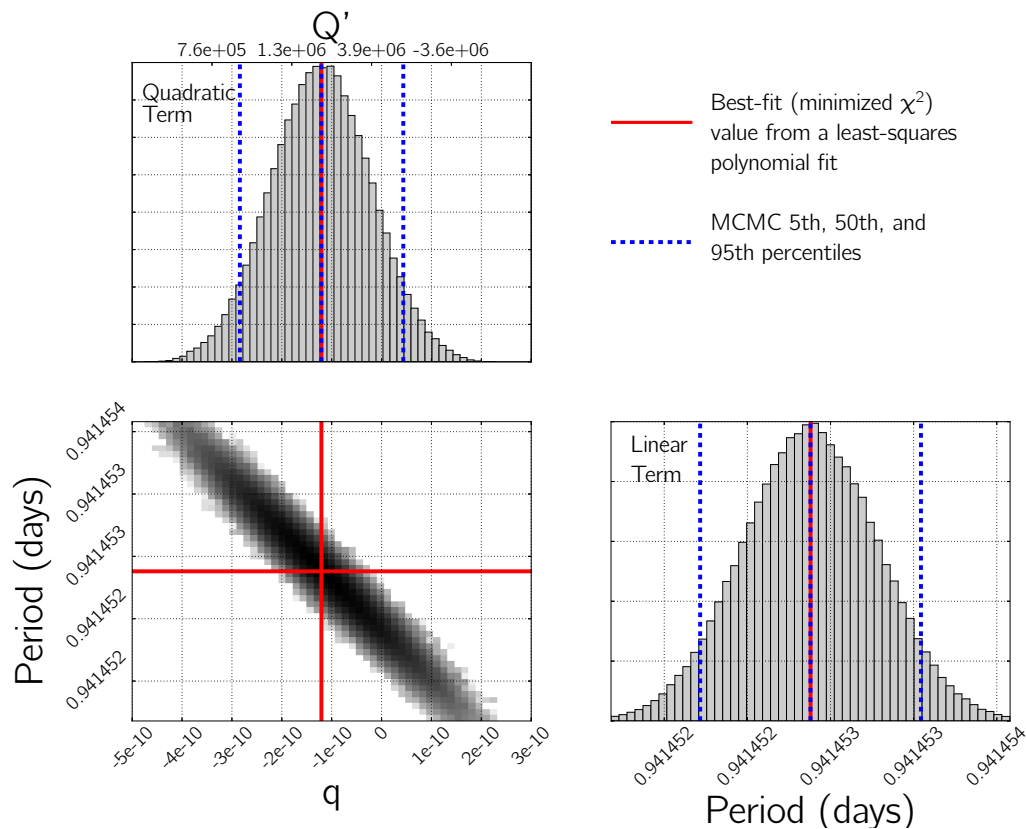


Figure 4.2 MCMC posterior probability distributions for the linear and quadratic parameters of the quadratic fit, q (proportional to $-1/Q'$), and p (orbital period), with 5th, 50th, and 95th percentiles marked by the dashed lines. We leave the less important intercept term off of this corner plot, for clarity. Overplotted in red are the best-fit values from the least-squares polynomial fit (minimizing χ^2). The two methods agree on the value of the period and they both find only an upper limit for the magnitude of the quadratic term (corresponding to a lower limit on Q' , see top axis of the q plot).

4.5.1 Tidal Dissipation in G vs. F Stars

Tides raised within a central star by a planetary companion are dissipated within the star and angular momentum is transferred between the stellar spin and planetary orbit in the process (e.g. [Ogilvie 2014](#)). For short-period planets (orbiting sub-synchronously rotating stars), like WASP-18b, that also have approximately circular orbits, tidal dissipation in the star causes the planet to lose angular momentum and spiral inward, because the tidal bulge raised in the star lags the planet when the planet’s orbital period is less than the star’s rotational period (i.e. $P_{orb} < P_{rot}$). This is the opposite of the Earth-Moon system, in which the Moon recedes from the Earth because the bulge leads the Moon (since $P_{orb} > P_{rot}$). The rate of change of the orbit depends on the efficiency of tidal dissipation within the host star; this is where stellar structure becomes important.

The tide in the star is often decomposed into two contributions: an equilibrium tide and a dynamical tide (e.g. [Zahn 1977](#)). Dissipation of both components is expected to become less efficient in stars slightly more massive than the Sun (i.e. F stars). While we often generalize Sun-like stars (typically defined as $0.5M_{\odot} \lesssim M_{*} \lesssim 1.3 M_{\odot}$) to have radiative cores and convective envelopes and more massive stars to have the opposite, development of convective cores and radiative envelopes is actually a continuum. WASP-18, for example, is a $1.2\text{-}M_{\odot}$ F6 star, and, according to MESA stellar structure models ([Paxton et al., 2011](#)), should have a convective core within the innermost 6% of the stellar radius, and a convective envelope in the outer 15%; it is therefore intermediate between an solar-mass and high-mass star.

For tidal dissipation, therefore, an F star like WASP-18 is not "sun-like."

We quantify the efficiency of tidal dissipation using the tidal quality factor, Q , defined as (Goldreich, 1963):

$$Q \equiv \frac{\text{energy stored in tidal distortion}}{\text{energy dissipated in one cycle}} = 2\pi E_0 \left(\oint -\dot{E} dt \right)^{-1}, \quad (4.1)$$

where E_0 is the maximum energy stored in the tidal bulge and \dot{E} , intrinsically negative, is the energy dissipated in one tidal period. We use the modified Q (i.e. Q') convention throughout this Letter:

$$Q'_{*,0} \equiv \frac{3Q}{2k_2}, \quad (4.2)$$

where k_2 is the tidal Love number. Q' is almost certainly not a single constant number for all stars (even of the same spectral type), but is instead a complicated function of the stellar mass, structure, rotation, and tidal periods, as well as the planetary properties (e.g. Ogilvie 2014). Q' is the Q of an equivalent homogeneous body ($k_2 = 3/2$). A large Q' corresponds to weak or inefficient tidal dissipation, and a smaller Q' corresponds to strong or efficient dissipation. We investigate here the Q' of the star (WASP-18), not the planet (WASP-18b); the planet's tidal Q' is relevant for its own tidal evolution, and leads to synchronization of its rotation and circularization of its orbit.

The equilibrium tide is dissipated within the convective envelope of the star by the effective viscosity of convective turbulence (Zahn, 1966; Goldreich and Nicholson, 1977); however, the effective viscosity may be significantly reduced in the case of a short-period planet (Penev and Sasselov, 2011; Ogilvie and Lesur, 2012). In addition, in F stars, the outer convection zone is thin and of very low mass, so it

is expected to be much less dissipative than in G-stars; the effective tidal Q' could be as high as 10^{11} (Barker and Ogilvie, 2009) for a star like WASP-18 at the tidal frequencies of interest. Dissipation in the convective core of an F star is also likely weak (e.g. Zahn 1977).

The dynamical tide primarily consists of internal gravity (g-mode) waves that are tidally excited at the convective-envelope-radiative-core boundary and propagate inwards to the center of the star. These waves are thought to be damped by radiative diffusion or nonlinear effects. If they can reach the center, they become geometrically focused and, if the planet exciting them is sufficiently massive – like WASP-18b – they may reach sufficiently large amplitudes such that they break, leading to significantly enhanced tidal dissipation (Goodman and Dickson, 1998; Ogilvie and Lin, 2007; Barker and Ogilvie, 2010; Barker, 2011). This process deposits angular momentum into the star, thereby removing angular momentum from the planet’s orbit; the star’s rotation gets faster (“spin-up”), while the planet’s orbit shrinks. If WASP-18 were Sun-like, WASP-18b would be sufficiently massive to cause wave breaking, and we would expect the planet to rapidly spiral into its star. However, in the case of an F-star like WASP-18, the convective core prevents the tidally-excited gravity waves from reaching the center where they would be focused, so that they may never reach such large amplitudes to break, though they may be subject to weaker nonlinear effects (eg. Barker and Ogilvie 2011; Weinberg et al. 2012; Essick and Weinberg 2016). The dissipation would be significantly reduced, save for select resonant tidal frequencies, so that we would expect the planet to remain in the orbit in which it was discovered (Barker and Ogilvie, 2009). Furthermore,

the lingering thin outer convective envelope in an F star of WASP-18’s mass would inhibit radiative damping of the waves near the top of the radiative zone (relative to more massive A-stars). The dissipation that [Valsecchi and Rasio \(2014\)](#) find for WASP-71 may be moderately higher than we would expect in WASP-18 precisely because it is a more massive (1.5 versus $1.2 M_{\odot}$) star, and therefore has a thinner outer convective envelope than WASP-18, but what they obtain is still very weak.

Were a resonance present, Q' could indeed be very low, and therefore the star could be quite dissipative. However, the above arguments and those of, e.g. [Lanza et al. \(2011\)](#); [Barker and Ogilvie \(2009\)](#), support a high- Q' , generally minimally-dissipative scenario for a star like WASP-18.

4.5.2 Estimating the Tidal Q' for WASP-18

When a planet transits its host star, we have a convenient time point from which to measure any changes in the orbit, which we infer through a shift in the transit (or secondary eclipse) arrival time. [Birkby et al. \(2014\)](#) show that the expected shift can be reduced to:

$$T_{shift} = - \left(\frac{27}{8} \right) \left(\frac{M_p}{M_*} \right) \left(\frac{R_*}{a} \right)^5 \left(\frac{2\pi}{P} \right) \left(\frac{1}{Q_*'} \right) T^2, \quad (4.3)$$

where M_p/M_* is the planet-to-star mass ratio (for WASP-18, $M_p/M_* = 0.007843$), R_*/a is the stellar-radius-to-semi-major-axis ratio (for WASP-18, $R_*/a = 0.2789$), T is the elapsed time, and P is the orbital period of the planet. Therefore, in a quadratic fit of the form

$$t = qT^2 + pT + c, \quad (4.4)$$

where the linear coefficient p corresponds to the period of the planet’s orbit, the quadratic term is defined by Equation 4.3. Rearranging, we find that Q' depends on the quadratic coefficient q as:

$$Q' = - \left(\frac{27}{8} \right) \left(\frac{M_p}{M_*} \right) \left(\frac{R_*}{a} \right)^5 \left(\frac{2\pi}{P} \right) \left(\frac{1}{q} \right) \quad (4.5)$$

We fit for the coefficients in Equation 4.4, and thus the period and Q' , as discussed in § 4.4 and shown in Figure 4.2.

Equation 4.3 makes clear that a planet must be close-in and massive (relative to the radius and mass of the host star), its orbital period must be short, and it must orbit a star with a favorable Q' , in order to produce any discernible shift in time. Currently, in the NASA Exoplanet Archive, only eight confirmed planets have both masses larger than $1.0 M_J$ and orbital periods of roughly one day or less. The addition of recently-announced KELT-16b (Oberst et al., 2016) makes nine. Of those, one is around a pulsar and four (WASP-18b, KELT-16b, WASP-12b, and WASP-103b) are around stars more massive than $1.2 M_\odot$ and therefore likely possessing convective cores that preclude tidal wave breaking at the center. Of the remaining four, WASP-43b has already demonstrated no rapid tidal decay (Hoyer et al., 2016), but WASP-19, WTS-2, and K2-22 all orbit stars less massive than the sun, and may be reasonable testbeds for dissipation within a star with a larger convective envelope and a smaller radiative core; Birkby et al. (2014) has already suggested that WTS-2 should have a barely-discernible shift for $Q'=10^6$ (17 s over 16 years).

Equation 4.3 assumes a stellar obliquity of zero and neglects tidal dissipation

in the planet, assuming its orbit to be circularized and its spin to be synchronized and aligned with the orbit. The canonical value of Q' is 10^6 , as derived for stars from measurements of the orbits of binary star systems (e.g. [Meibom and Mathieu 2005](#)) and for Solar System giant planets from the orbits of their satellites ([Zhang and Hamilton, 2008](#))).

We return to Figure 4.2, as we can now interpret the findings for q (and therefore Q') physically. The 95th percentile posterior probability distribution for q is effectively zero; given that $Q' \propto \frac{1}{q}$, this means we only can definitively extract a lower limit, $Q' \geq 1 \times 10^6$, taken at the 5th percentile of the q distribution. Continued monitoring of this system should further constrain WASP-18's Q' , and it follows from the discussion above that we will continue to find an increasing lower limit, i.e. no evidence of rapid tidal decay.

4.6 Conclusion

We have combined previously published and new data to find no conclusive evidence of rapid tidal decay of the orbit of WASP-18b, supporting predictions of little to no tidal decay for a short-period planet around an F star ([Barker and Ogilvie, 2009, 2010; Barker, 2011](#)), given our current understanding of the physics of tidal dissipation in F stars. We find for WASP-18 that $Q' \geq 1 \times 10^6$ at 95% confidence. Further observations of WASP-18b and similar monitoring of planets like WASP-19b, WTS-2b, and K2-22b would add tighter observational constraints on stellar Q' for various stellar types, and allow us to further probe the mechanisms of stellar

tidal dissipation.

Acknowledgements

The authors thank the referee for a careful eye and helpful insights. TRAPPIST is a project funded by the Belgian Fund for Scientific Research (F.R.S.-FNRS) under grant FRFC 2.5.594.09.F, with the participation of the Swiss National Science Foundation (SNF). L.D. acknowledges support of the F.R.I.A. fund of the F.R.S-FNRS. M. Gillon and E. Jehin are F.R.S.-FNRS Research Associates. AJB was supported by The Leverhulme Trust through the award of an Early Career Fellowship.

Chapter 5: The *HST* Infrared Transmission Spectrum of Hot Neptune HATS-7b

5.1 Introduction

The Hubble Space Telescope (HST) was not designed for exoplanet characterization; not only had no exoplanet discovery been confirmed at launch, but also, there was no expectation that characterization of the first discoveries, if and when they came, could be characterized for decades at least, because the expectation was based on the solar system planetary architecture. Instead, the last two decades have brought on thousands of discoveries (~ 3500 as of August 2017), and many of those planets have been tantalizingly in reach of instrumentation never designed with them in mind. Giant transiting planets orbiting incredibly close to their host stars have opened up an entirely new phase space of study, allowing us to pursue now what we thought would not come for decades.

The first years of transit spectroscopy with the Hubble Space Telescope (HST) were fraught with challenges, as the NICMOS instrument in particular displayed significant systematics at the levels of the very small variations caused by exoplanet atmospheres, with conflicting results coming from the same data (e.g. HD 189733 b:

Swain et al. 2008; Gibson et al. 2011, 2012; Waldmann et al. 2013). The installation of the Wide-Field Camera 3 (WFC3) in 2009 brought new, but improved, systematics to the next generation of observations, which, with nontrivial effort, yielded spectra that were more robust (e.g., Berta et al. 2012; Mandell et al. 2013; Line et al. 2013a; Ranjan et al. 2014; Wilkins et al. 2014), but surprising: the expected near-infrared water absorption feature was either missing or weak in all WFC3 observations. The third wave of HST spectroscopy was ushered in by the revival of an old observing mode: spatial scan (McCullough and MacKenty, 2012). After the first application of the new observing mode was announced, achieving near-photometric precision (Deming et al., 2013), it has become the standard for near-infrared transiting exoplanet spectroscopy, in both transmission (primary transit) and emission (secondary eclipse). We now see different groups using different analyses consistently reproducing the same results, (e.g., GJ 1214b: Berta et al. 2012; Kreidberg et al. 2014, HD 209458b: Deming et al. 2013; Tsiaras et al. 2016), and comparison studies are now possible Sing et al. (2016), though numbers remain small.

However, to near-photometric precision, many spectra still are flat and featureless, or with weaker-than-expected water absorption. Water is a valuable diagnostic of exoplanetary atmospheres. In hydrogen-rich atmospheres and hydrogen-depleted, low (< 1) carbon-to-oxygen-ratio atmospheres, water is the dominant reservoir for oxygen (Hu and Seager, 2014). Water abundance is therefore a useful proxy for oxygen abundance, which can reveal the formation location of the planet within the protoplanetary disk (Öberg et al., 2011). The HST WFC3 infrared G141 grism centers on a strong water absorption band at $1.4 \mu\text{m}$, and water is the only ab-

sorber expected in any abundance in planetary atmospheres in the grism wavelength coverage, so there should be no confusion as to the source of any detected absorption. The absence of strong absorption could point to unexpectedly high mean-molecular-weight atmospheres (these so-called “water worlds,” therefore have dense, small-scale-height atmospheres with weak absorption in transmission, e.g. [Bean et al. 2010](#); [Miller-Ricci and Fortney 2010](#)), or to the presence of high-altitude aerosols (i.e. clouds and/or hazes). The precision of the GJ 1214b measurement did enable elimination of the water world scenario, pointing squarely at aerosols, although the specific nature of those particles is still challenging to constrain until necessary laboratory data becomes available ([Fortney et al., 2010](#)).

Only a handful of known exoplanets are both smaller than Jupiter and within reach of the near-infrared WFC3 grism; those that HST has observed are listed in [Table 5.1](#); of these, only two (HAT-p-11b [Fraine et al. 2014](#) and HAT-p-26b [Wakeford et al. 2017a](#)) show water absorption, while the other planet’s spectra are effectively flat. The detection of water on each planet yielded significant insights into the natures of their atmospheres, especially because the HST spectra could be coupled with infrared spectrophotometry from *Spitzer*.

HATS-7b ([Bakos et al., 2015](#)), discovered by the transit survey of the ground-based HATSouth network ([Bakos et al., 2013](#)) is a super Neptune (or sub-Saturn) of mass $38 M_{\oplus}$ ($0.12 M_J$) and radius $6.2 R_{\oplus}$ ($0.56 R_J$), orbiting around a metal-rich ($[\text{Fe}/\text{H}] = +0.25$) K-dwarf star every 3.1 days (0.04 AU). The planet’s bulk density, 0.83 g/cm^3 , is not much higher than that of Saturn, although, as [Petigura et al. \(2017\)](#) find, and [Figure 5.1](#) hints, there seems to be little to no correlation between

the size and mass of sub-Saturns (defined as having radii between 4.0 and 8.0 R_{\oplus}). Along with the discovery data, [Bakos et al. \(2015\)](#) determined that the star, HATS-7, is quiet, as they only found minimal detections of either Calcium HK activity or RV jitter.

[Petigura et al. \(2017\)](#) did see a strong correlation between planet mass and the metallicity ($[\text{Fe}/\text{H}]$) of the host star, inferring that metal-rich stars, with their corresponding metal-rich protoplanetary disks, are generally able to form larger planets via core accretion, because the disk would have had a larger supply of solid material to form larger solid cores, which in turn would be able to accrete more gas. This could explain HATS-7b’s large radius and resultant low bulk density, but there is a degeneracy: giant planets irradiated at flux levels above approximately $2 \times 10^8 \text{ erg s}^{-1} \text{ cm}^{-2}$ ([Miller and Fortney, 2011](#); [Demory and Seager, 2011](#)) (for HATS-7b, $\langle F \rangle \sim 3 \times 10^9 \text{ erg s}^{-1} \text{ cm}^{-2}$) can be subject to radius inflation mechanisms. Further, the [Petigura et al. \(2017\)](#) findings rely only on knowing the bulk density of the planet, and then inferring bulk planet metallicity from the tight correlation between the two parameters for Solar System planets (e.g., [Fortney et al. 2007](#)). However, this correlation is based only on the Solar System, and therefore has not been thoroughly tested or explored in the vast phase space opened up by exoplanet discoveries, and may be particularly inapplicable to gas giants that have migrated, and now orbit in a highly irradiated environment. [Thorngren et al. \(2016\)](#) found correlations between planet mass and both planet heavy element mass and the planet-to-star metal enrichment ratio, but that study was again limited to planets of low irradiance, and had to make many assumptions about the differentiation

of planetary interiors. Case studies of individual planets, wherein heavy metal abundances can actually be measured, can break the degeneracies and reduce the uncertainties on these types of calculations.

In the solar system, we see the classes of ice giants (Neptune and Uranus) and gas giants (Saturn and Jupiter) as separate and distinct HATS-7b’s mass ($0.12 M_J$) places it just below the break in the

mass-density correlation for exoplanets, which corresponds to the point in planet formation at which accretion of more material starts to further compress the atmosphere, increasing the planet’s density, where before increasing mass had resulted in lower density, as the planet would have been accreting H-rich gas that extended the atmosphere (Weiss et al., 2013). This is the transition point between ice giants (like Neptune and Uranus) and gas giants (like Saturn and Jupiter) that is still poorly understood, and has no analog in our own Solar System.

In this chapter, we present the transmission spectrum in broadband optical, near-infrared ($1.1 - 1.7 \mu\text{m}$), and infrared (3.6 and $4.5 \mu\text{m}$) light and use it to perform the first atmospheric characterization of sub-Saturn (or super Neptune) HATS-7b.

5.2 Observations

The transit observations of HATS-7b used in this chapter are summarized in Table 5.2.

The *Hubble Space Telescope* (*HST*) observed the transit of HATS-7b across its star twice in 2016 (PID 14260, PI Deming) in spatial scan mode (McCullough and

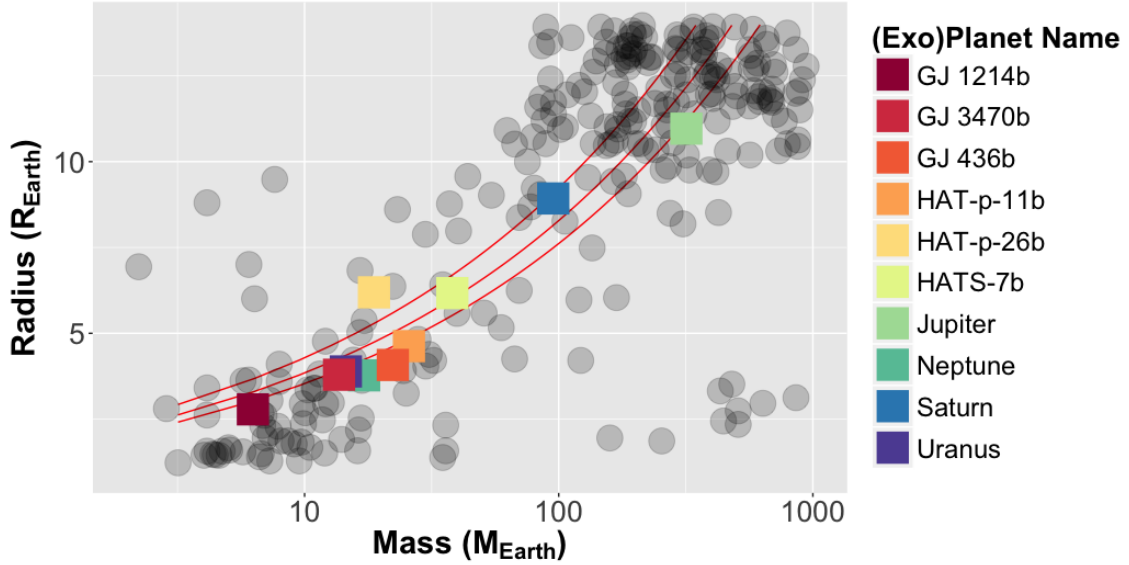


Figure 5.1 The mass radius diagram of exoplanets for which both parameters are known, with the six HST-observed sub-Saturn-to-mini-Neptune-sized exoplanets GJ 436b, HAT-P-11b, HAT-P-26b, GJ 1214b, GJ 3470b, and HATS-7b, as well as the Solar System giants plotted in color over the general population of planets. Lines of constant density are drawn in red, corresponding to 0.69, 1.0, and 1.27 g/cm³ (Saturn, water, and Uranus, respectively).

[MacKenty, 2012](#); [Deming et al., 2013](#)). All observations were made with the Wide Field Camera 3 (WFC3) G141 infrared slitless grism, covering 1.1 - 1.7 μm .

In addition, the *Spitzer Space Telescope* observed two more transits of HATS-7b in 2016 (PID 13044, PI Deming), one each in the warm mission IRAC filters, 3.6 and 4.5 μm . *Spitzer* suffers from its own systematics, particularly an intra-pixel effect, requiring specialized data analysis. Therefore, Drake Deming did the analysis to produce the *Spitzer* results used in this thesis, using the pixel-level decorrelation (PLD) that he developed ([Deming et al., 2015](#)). A full description of the analysis will be in the journal submission version of this chapter.

Finally, this *HST* program has a collaboration with the KELT ([Pepper et al., 2007, 2012](#)) follow-up network, which allows us to refine the orbital parameters better

than we could with HST alone, given the insufficient temporal sampling of the light curve. The orbital parameters derived from observations with the ground-based telescopes is in Table 5.4

5.3 HST Data Reduction

The details of the HST data are listed in Table 5.3. Much of our reduction process follows that of previous work (Wilkins et al., 2014), but we review it briefly here, and highlight any differences or updates. We have opted to work only with the penultimate data product of the HST `calwf3` pipeline, the `ima` files, rather than the final data product, the `flt` files.

5.3.0.1 Wavelength Solution and Wavelength-Dependent Flat Field

In previous work, we used the G141 wavelength solutions of Kuntschner et al. (2009) with empirically-derived correction factors after we saw misalignment between the G141 sensitivity curve and our data (Wilkins et al., 2014). This solution worked, but was unsatisfying. Further, as (Tsiaras et al., 2016) points out, did not account for the 0.5° -tilt of the dispersion. Tsiaras et al. (2016) also describe a far more detailed process for calculating the position on the trace, though their final spectrum was not significantly different from the first analysis of Deming et al. (2013). In late 2016, STScI released not only updated coefficients, but also a new, simpler way of calculating the necessary parameters to find the wavelength solution (Pirzkal et al., 2016). We use the updated solutions (found in the WFC3 configu-

ration file `G141.F139M.V4.32.conf`¹ to calculate the wavelength corresponding to each pixel on each data frame. As before, we start from the direct image, taken with the F139M filter immediately prior to beginning the observation. The direct image tells us where the target is on the detector (at least at the start of an observation), which sets the reference point for the wavelength solution. We do that by fitting a two-dimensional Gaussian to the PSF of the star on the direct image, and setting the reference coordinate equal to the center of that Gaussian. Neither the direct image nor the spatially scanned spectra are necessarily on the full (1024×1024) WFC3 infrared detector array; for exoplanet observations, they usually are not. The calibration data are all based on the full detector array, though *without* the five-pixel bias frame (i.e., 1014×1014). As [Tsiaras et al. \(2016\)](#) notes, the x-coordinate offset, δx_{star} (and, in parallel, δy_{star}) would be:

$$\delta x_{star} = (507 + 0.5L) + \Delta x_{off} + \Delta x_{ref} \quad (5.1)$$

where L is the length of the subarray (because each subarray is nominally at the center of the full array), Δx_{off} is the difference between x_{off} values² of the F140W filter (used to calculate wavelength solution) and the direct image filter, and the difference in chip reference pixels for the direct image frame from the spectrum frame, Δx_{ref} , is

$$\begin{aligned} \Delta x_{ref} = & (\text{CRPIX1}_{\text{spectrum}} + \text{POSTARG1}_{\text{spectrum}}) - \\ & (\text{CRPIX1}_{\text{direct image}} + \text{POSTARG1}_{\text{direct image}}) - 5.0, \end{aligned} \quad (5.2)$$

where `CRPIX1` (`CRPIX2`) is the FITS header keyword for the x(y)-coordinate of the chip reference pixel, and `POSTARG1` (`POSTARG2`) is the x(y)-coordinate of the observer-

requested offset (default is zero, but can be particularly useful for spatial scan mode observations to, for example, keep the scan from running off the edge of the detector in one or both directions). The 5.0 term is a final accounting of the bias frame not used in deriving the calibration parameters.

The Pirzkal et al. (2016) wavelength solution indeed modifies the previous structure, but not dramatically, and only for the better, in terms of clarity. Upon calculating the new reference coordinates corresponding to the location of the star on the detector, we can calculate the wavelength solution using a new set of coefficients found in the appropriate configuration file. In our procedure, we generate a wavelength solution for the full array (1014×1014), and then subset it by the correct coordinates (again using the offset equation above) for a two-dimensional array of the same number of pixels as the spectral data frame. Each pixel at coordinate x'_i, y'_i (where ' denotes a coordinate in the full-frame coordinate system) has an associated wavelength, λ_i . First, we need the displacement from the reference pixels (x'_{star}, y'_{star}), also known as the path length, which can be calculated analytically:

$$\Delta p = (x'_{star} - x'_i) \times m, \tag{5.3}$$

where

$$m = \sqrt{1 + (a_{1,0} + a_{1,1}x'_{star} + a_{1,2}y'_{star} + a_{1,3}x'^2_{star} + a_{1,4}x'_{star}y'_i + a_{1,5}y'^2_i)^2} \tag{5.4}$$

where the $a_{1,n}$ coefficients correspond to the DYDX_A.1 coefficients (“A” refers

²http://www.stsci.edu/hst/wfc3/analysis/grism_obs/calibrations/wfc3_g141.html

²<http://www.stsci.edu/hst/observatory/apertures/wfc3.html>

to the first dispersion order) in the configuration file. Finally, we can use Δp and the DLDP_A_0 and DLDP_A_1 coefficients (denoted l in this chapter) to calculate the wavelength at a given pixel, λ_i , with

$$\lambda_i = l_{0,0} + l_{0,1}x'_{star} + l_{0,2}y'_{star} + l_{0,3}x'^2_{star} + l_{0,4}x'_{star}y'_{star} + l_{0,5}y'^2_{star} + \Delta p(l_{1,0} + l_{1,1}x'_{star} + l_{1,2}y'_{star} + l_{1,3}x'^2_{star} + l_{1,4}x'_{star}y'_{star} + l_{1,5}y'^2_{star}). \quad (5.5)$$

With the wavelength solution set, we just need to take the latest flat field file and use the coefficients therein to calculate the flat field in the same manner as [Wilkins et al. \(2014\)](#), using a normalized wavelength coordinate. Before dividing out the flat field, we do use a cubic interpolation to tilt the scan data 0.5° on the data frame before the flat is applied.

As an aside: if an observation is taken on a larger subarray, the zeroth-order spectrum is visible on the data frame, and can be used instead of a direct image for the wavelength calibration, using the coefficients of [Bohlin et al. \(2015\)](#). This allows direct measurement of potential drift or shifts of the target placement on the detector throughout the observation, as the zeroth-order spectrum is virtually a point source, for which a centroid can be found.

5.3.0.2 Background Subtraction

We define the background as a box of pixels well above the spectral scan. To perform a background subtraction, for each frame, we plot a histogram of the pixel values within the box, perform a nonlinear least-squares Gaussian fit, and define the background as the mean value of the best-fit Gaussian. We assume that the background (sky) level is independent of location on the detector (and therefore

wavelength) and thus subtract that derived background value uniformly across the scan.

5.3.0.3 Sample-up-the-ramp

The WFC3 infrared detector has no mechanical shutter, but performs non-destructive reads as an exposure accumulates, thereby allowing the observer to see any anomalous behavior (e.g., non-linearity) during the course of the exposure. In spectral scanning mode, the observer sees the progress of the scan across the detector. Assembling images from these non-destructive reads, rather than just using the final readout, is called “sampling up the ramp.” STScI provides the sample reads in the [SCI] extensions of the `ima` data files; they also provide `flt` files where the sample-up-the-ramp process has already been done, along with some other final calibration steps of the `calwf3` pipeline. Our sample-up-the-ramp algorithm (Deming et al., 2013) applies the following procedure for each fifteen-sample exposure:

1. Read in the data and headers of the last (fifteenth, `frame1`) and next-to-last (fourteenth, `frame2`) readouts.
2. For each frame, separately: rotate frame by 0.5° using a cubic interpolation, divide out the wavelength-dependent flat field, and subtract a background (following the strategy above).
3. Subtract `frame2` from `frame1` to get a difference frame, `dframe`, made up of only the data collected between the two samples.

4. Sum the pixels of `dframe` by row to get a one-dimensional array along the y-axis.
5. Fit a Gaussian to this collapsed difference frame, finding the location of the peak. Round this to an integer.
6. Return to `dframe`, and after choosing a half-window size, set all rows of data more than that half-window size above or below the integer row number you just found to zero. This usually requires some iteration to find an optimal window size, which will ultimately be a function of the speed of the scan and brightness of the source. We use a half-window size of 10 rows for our mask here.
7. For this iteration, start a new frame, `xframe`, that consists of the masked `dframe`. Repeat all of the steps, iterating through all of the samples in each exposure (next is fourteenth and thirteenth reads, then thirteenth and twelfth, and so on). Add the masked `dframe` from each iteration to the `xframe` initiated in the first iteration.
8. Upon reaching the first sample, `xframe` holds the fully sampled-up-the-ramp image for that exposure. Move on to the next one.

5.3.0.4 Bad Pixels

Early stages in the `calwf3` pipeline perform various bad pixel corrections in preparation of the `ima` files. We do one additional sweep for any bad pixels by

searching for any individual pixels that deviate more than 4σ away from their median value both temporally and spatially, and replace them with a median. We correct fewer than ten pixels in either frame.

5.4 Results: Extracting the HST White Light Curve and Spectrum

Multi-visit transit observations can be combined to increase the sampling of the light curve and/or to increase the signal-to-noise ratio for any potential spectroscopic features. However, challenges arise not just with the presence of the now well-studied systematics, but additionally because procedures for correcting the systematics (which need to be done separately for each dataset) are inevitably interwoven with the procedures for extracting usable data (which would be ideally done on the combined data as much as possible).

The *HST* systematics are generally similar in presentation, can vary significantly in magnitude between observations, for myriad reasons, only some of which are understood. The phenomena observed in the HST exoplanet light curves fall into three categories: visit-long slopes, orbit-long slopes, and intra-orbit “hooks.” We know that the systematics are dramatically reduced when the peak flux levels remain below approximately 30,000 electrons, and the intra-orbit hook corresponds to dumps of the detector buffer, when the data stored in the WFC3 buffer are sent to the solid-state recorder on the spacecraft (Wilkins et al., 2014). It is tempting to assume these are simply an occurrence of persistence, the slow release of trapped electrons after observation of particularly bright objects (Smith et al., 2008). How-

ever, this cannot be simple persistence; it has neither the progenitor nor evolution we would expect for persistence. Persistence can be a concern on the *HST*/WFC3 detector, which is why STScI provides persistence correction data; these do little to affect the systematics we observe.

Efforts to develop a physical understanding of the systematic effects (e.g., [Berta et al. 2012](#); [Wilkins et al. 2014](#); [Zhou et al. 2017](#)) have not made much headway, relying on toy models that do not truly reach the physics and that do not improve the results, as variants of `divide-out` ([Berta et al., 2012](#)) analyses and the advent of spatial scan have enabled near-photon-limit precision, anyway (e.g., [Deming et al. 2013](#); [Kreidberg et al. 2014](#); [Knutson et al. 2014b](#)). In particular, spatial scan alleviates the worst of the systematics by reducing the incident flux on individual pixels, which reduces the amplitude of the hook, and also limits it to a single iteration each orbit, as the spreading of the light across the detector allows the instrument to wait until an orbit concludes for a buffer dump.

For these HATS-7b data, we refined a hybrid approach to extracting both the white light curve and spectrum of the planet while also correcting for the systematics. The process is iterative, using the better fits found later in the pipeline to improve the data extracted earlier. Anything systematic can vary from visit to visit, but anything astrophysical should not; therefore, the data are separated and merged together multiple times throughout the process. As is typical, we first calculate a white light curve, which is the integrated broad-band light observed over time, and then we use that to extract the slight variations in the transit depth over wavelength to assemble a spectrum.

To fit the *HST* white light transit curve, we follow a similar procedure as Todorov et al. (2012), and as we have followed in previous works (Deming et al., 2013; Wilkins et al., 2014), which is to fit only for central phase and transit depth $((R_p/R_{star})^2)$, holding fixed all other planetary and stellar parameters to the values in the last column of Table 5.4, calculated using our ground-based observations. Because HST necessarily has large gaps in time over the course of the transit as the satellite passes behind the Earth and can no longer see the target, it does not sample the transit ingress and egress sufficiently to constrain orbital parameters nearly so as well as the amateur ground-based observations can.

Upon calibrating and cleaning the data as described in 5.3, we first (1) *calculate a preliminary light curve, not corrected for any systematics*: we take the cleaned data cube, draw a box around the scanned spectra, and sum up the pixels within the box for each data frame (34 frames for each visit). As usual, we see far worse effects on the first few frames, so we temporarily drop the first orbit, and then (2) *carry out a divide-out-style correction to the light curve*, using the second and fifth orbits to generate an average orbit hook and also fitting and dividing out a linear trend.

With this preliminary corrected light curve, we (3) *execute the first-round transit model fit to the light curves separately*. Our fitting procedure is to generate 800 transit curves shifted progressively in phase by 0.00001 (~ 2.7 s) with the optical planet-to-star radius, at a temporal resolution much higher than the observed light curve, interpolate the high-resolution, shifted transit curve onto the observed light curve observed phase array, and perform a multiple linear regression fit of phase, the shifted transit curve, and the data. We select a best-fit transit curve by finding

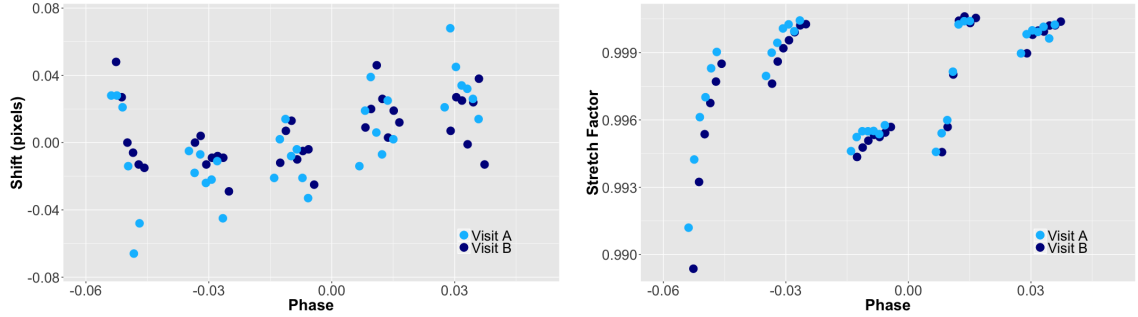


Figure 5.2 Result of the shift-and-fit procedure discussed in §5.4

the minimum $\chi_{squared}$

Next, we (4) perform the spectral shift-and-fit procedure detailed in Deming et al. (2013) separately on the data from each visit. We use the five exposures just before first contact and the five exposures just after last contact, summing each of the ten two-dimensional scans along the scan axis, and then averaging them together to make a “template spectrum.” We shift this template spectrum from by -1 to +1 pixels, by increments of $1/1000^{th}$ pixel, and then again perform a multiple linear regression and minimization of χ^2 . We save the residuals between the best-fit shifted-and-scaled template and the data, because in those is where the transmission spectrum lies. The best-fit shifts and scale factors are plotted in Figure 5.2. Notice the scale factor in particular: it traces the trend of the systematics, and not by coincidence: by comparing each spectrum against an average template, we are, in effect, performing a variant in the spirit of `divide-out`, but more sensitive to the change of the hook over the course of the visit (far more severe in the first orbit, then a more gradual improvement from orbit 2 to orbit 5).

At this point, we return to the (uncorrected) light curves. We (5) use the

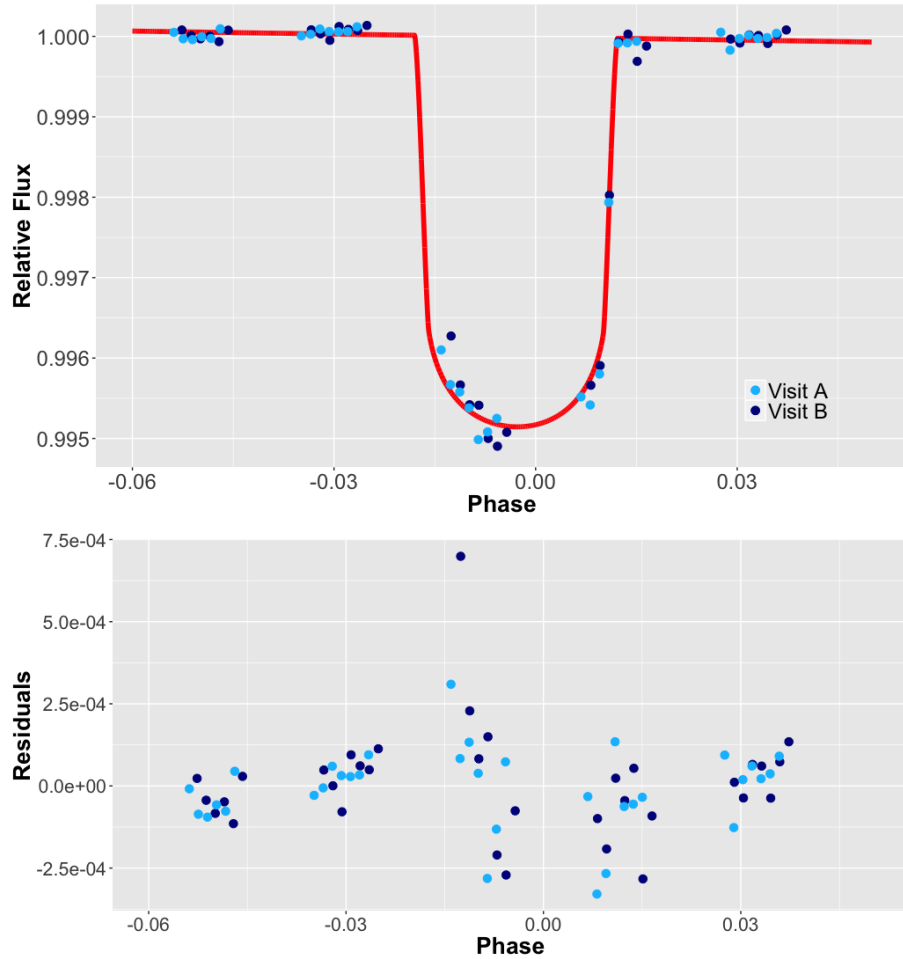


Figure 5.3 HATS-7 HST corrected white light curve and residuals.

scale values directly to separately correct the white light curves, averaging orbits 1, 2, and 5 by their respective scale factors, and orbits 3 and 4 by weighted averages of the orbits 2 and 5 scale factors. Now, we can finally (6) combine the data, normalizing them against one another, and repeat the process of fitting the transit curve to the combined white light data. We find a much better white-light fit, as shown in Figure 5.3, and are able to use all of the first orbit points.

We (7) estimate the errors on the best-fit transit depth and central phase via residual permutation (also referred to in the literature as “prayer bead”), in the

style described by [Southworth \(2008\)](#); [Winn et al. \(2008\)](#) (though see [Cubillos et al. \(2017b\)](#) for limitations on the method). This method, as its name implies, relies on permuting the residuals – the differences between the best-fit model and the data – but circularly, such that they retain their order, thereby retaining the influence of time-dependent systematics. We iterate over the number of data points (in this case, 68 total exposures in the light curve), moving the last error into the first position each time, and create a new, synthetic light curve by adding the permuted residuals back to the model fit (recall that the real data is the model fit plus the un-permuted residuals). We then re-fit a transit curve, again finding best-fit values for the transit depth and central phase, as described above. As a brief example, let us consider if we had just four data frames with residuals $[\text{resid}_A, \text{resid}_B, \text{resid}_C, \text{resid}_D]$, and a best-fit model that had the values $[\text{fit}_A, \text{fit}_B, \text{fit}_C, \text{fit}_D]$, we would iterate four times:

$$\textit{Iteration 1: Data} = [\text{fit}_A, \text{fit}_B, \text{fit}_C, \text{fit}_D] + [\text{resid}_D, \text{resid}_A, \text{resid}_B, \text{resid}_C]$$

$$\textit{Iteration 2: Data} = [\text{fit}_A, \text{fit}_B, \text{fit}_C, \text{fit}_D] + [\text{resid}_D, \text{resid}_A, \text{resid}_B, \text{resid}_C]$$

$$\textit{Iteration 3: Data} = [\text{fit}_A, \text{fit}_B, \text{fit}_C, \text{fit}_D] + [\text{resid}_D, \text{resid}_A, \text{resid}_B, \text{resid}_C]$$

$$\textit{Iteration 4: Data} = [\text{fit}_A, \text{fit}_B, \text{fit}_C, \text{fit}_D] + [\text{resid}_A, \text{resid}_B, \text{resid}_C, \text{resid}_D]$$

The final iteration returns back to the original data. While much of our data analysis takes place in IDL, using the [Mandel and Agol \(2002\)](#) algorithm for transit curves, we switch to the faster BATMAN ([Kreidberg, 2015](#)) algorithm in Python for the residual permutation. See [Figure 5.4](#).

The best-fit, binned values for the *HST* spectrum, along with the Spitzer spectrophotometry, are printed in [Table 5.5](#).

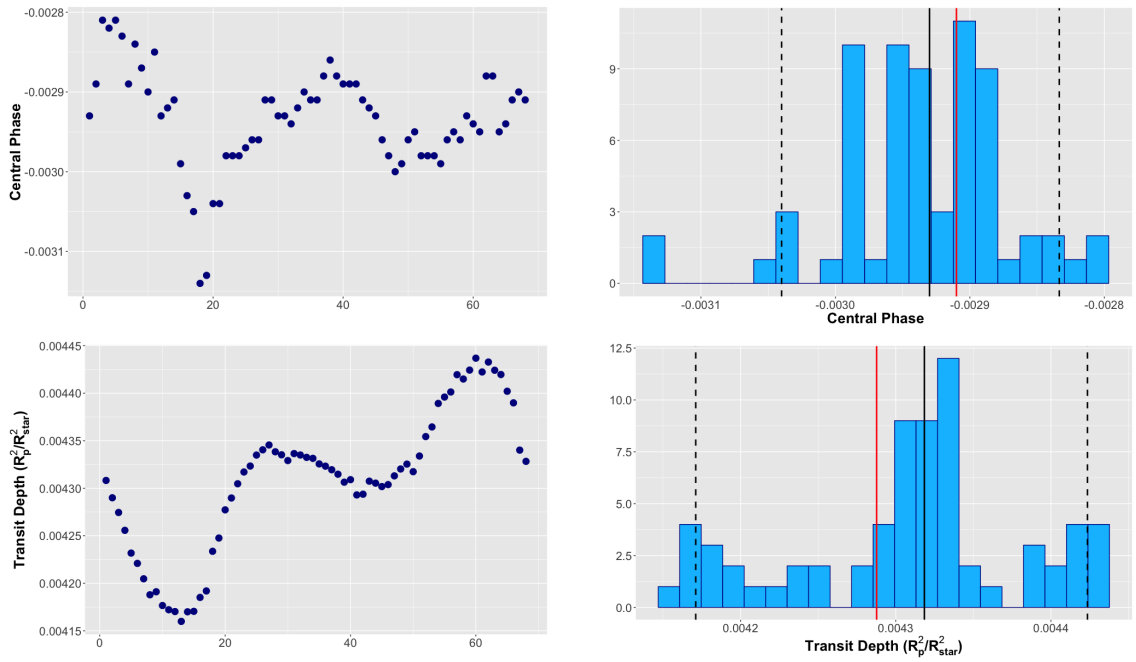


Figure 5.4 Results of the prayer-bead permutation of the residuals for the transit central phase (*top*) and depth (*bottom*), with the best-fit values plotted as a function of permutation (*left*) and as a histogram (*right*). On the histograms, the best-fit value is marked by a red line, and the 5th, 50th, and 95th quantiles (2σ) are marked with black dashed lines.

5.5 Discussion

When a planet transits its host star, the starlight is filtered through the limb of the atmosphere at a radius corresponding to a chord of optical depth $\tau \sim 1$ (e.g., [Heng 2017](#)). The transit radius therefore varies with wavelength; in absorption lines, the transit radius would be large, as more starlight is absorbed by the atmosphere. We would expect an absorption feature to be a few pressure scale heights deep (e.g., [Seager et al. 2009](#); [Encrenaz 2014](#)), where we define the scale height, H_0 , as

$$H_0 \equiv \frac{kT}{\mu_m m_H g}, \quad (5.6)$$

which is the the e-folding distance for pressure in an isothermal, constant-mean-molecular-weight atmosphere, where k is the Boltzmann constant, T is the temperature, μ_m is the mean molecular weight, m_H is the mass of hydrogen, and g is the surface gravity. The amplitude of absorption, A , is then

$$A = 5 \times \frac{2R_p H_0}{R_{star}^2} \quad (5.7)$$

where R_p and R_{star} are the planet's and star's radii, respectively. If we estimate the planet's temperature as its equilibrium temperature,

$$T_{eq} = T_{eff,star} \sqrt{\frac{R_{star}}{a}} (f'(1 - A_B))^{1/4}, \quad (5.8)$$

and make the following assumptions:

1. Bond Albedo ($A_B = 0.03$),
2. correction factor $f' = 2/3$ (no heat redistribution to the dark hemisphere),

and

3. mean molecular weight $\mu = 2.3$ (H/He-dominated envelope),

then, using the parameters of Table 5.4, we find a scale height $H_0 = 41.4$ km, corresponding to an amplitude of $A = 5.1 \times 10^{-4}$ (510 ppm). Of the above assumptions, none are more suspect and consequential if wrong than the mean molecular weight, which could more than an order of magnitude higher for a hydrogen-depleted atmosphere, which would in turn reduce the scale height and absorption amplitude by the same factor. Further, this assumes a clear atmosphere, free of condensates, which has proven to be an unsafe assumption in the realm of transit spectroscopy.

However, we need not be too pessimistic: we unequivocally detect water absorption in the transmission spectrum of HATS-7b. We discuss potential implications of our detection by first comparing it with other featured sub-Saturn spectra, and then exploring radiative transfer models that could explain what we observe.

5.5.1 Comparing to other sub-Saturn Spectra

To contextualize our result and perhaps draw some qualitative conclusions about its implications, we compare the spectra of HAT-p-26b (Wakeford et al., 2017c) and HAT-p-11b (Fraine et al., 2014) to our measured spectrum of HATS-7b in Figure 5.5. We have converted each spectrum in Figure 5.5 to their respective scale heights, assuming $A_B = 0.03$ and $\mu = 2.3$ (H/He-rich) and setting the zero point to their respective *HST* white-light depths. Several contrasts immediately present themselves: it does, in fact, look like we are not only seeing absorption (recall that higher values correspond to absorption in a transmission spectrum),

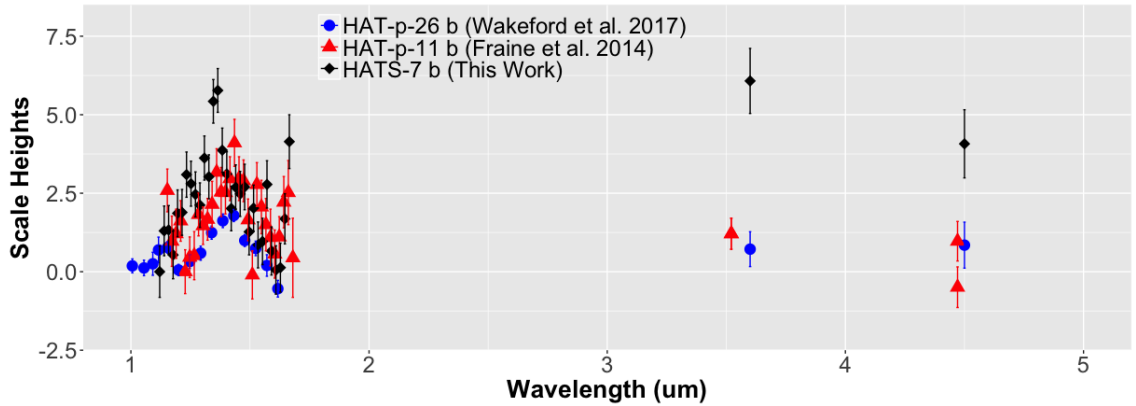


Figure 5.5 The *HST* and *Spitzer* spectra of HATS-7b, HAT-p-11b, and HAT-p-26b, the only sub-Saturns with statistically significant water absorption.

but also a stronger feature than either previous sub-Saturn. Further, HATS-7b's absorption feature peaks just blue-ward (at shorter wavelength) than we might have expected the water feature in a solar-abundance, clear atmosphere should peak at $1.41 \mu\text{m}$, while the feature in the HATS-7b spectrum peaks around $1.35 \mu\text{m}$. This would likely require a cooler temperature, as the lines that make up the blue side of the $1.4 \mu\text{m}$ feature complex are fewer, but have much higher line strengths. At lower temperatures (or perhaps in the circumstance of clouds), only the strong lines would come through. Suppression of CO could be a consequence of abundance differences, but could also be explained by temperature, as CH_4 becomes the favored carbon reservoir over CO at lower temperatures. We can also infer that there is little vertical mixing in this planet, as CO is not being dredged up from the interior, as has been invoked to explain the overabundance of CO in Jupiter's atmosphere.

5.5.2 A Forward Model of the Atmosphere of HATS-7b

To model the detected transmission spectrum of HATS-7b, we use `ExoTransmit`, an open-source, fast, and modular radiative transfer model (Kempton et al., 2017). `ExoTransmit` was optimized for the modeling of super-Earth to giant planets, though is viable for a broad swath of exoplanetary mass, radius, and temperature phase space. The code uses isothermal temperature/pressure profiles (though allows a user to input one’s own T/P profile), because transmission spectroscopy is generally not sensitive to vertical gradients in temperature. `ExoTransmit` allows for a wide variety of condensates, including unusual molecules perhaps only found in the extreme environment close to a host star; for example, Mbarek and Kempton (2016) found graphite clouds to be a significant carbon sink in some atmospheres, and that chemistry is included in `Exotransmit`.

As a first step, we apply a preliminary retrieval with an STScI-provided forward model routine based on the CHIMERA (Line et al., 2013b) code and subsequent cloud enhancements (Line and Parmentier, 2016; Batalha and Line, 2017), which provides a first look at the rough region of phase space a best-fit model would occupy. We then turn to the `ExoTransmit` code to build a four-dimensional grid of models, spanning temperature (500 - 1300 K, increments of 100 K), metallicity (1, 10, 50, 100, and 1000x solar), Rayleigh scattering factor (0.0, 1.0, 10.0, 100.0x), and height of a uniform cloud deck of grey opacity (0.1 mbar, 1 mbar, 10 mbar, 1 bar, and 1.0 bar). As discussed above, we know that we are looking for a model that allows for strong water absorption and suppresses the CO feature at $4.5 \mu\text{m}$. We compare

several scenarios, all clear (cloud-free) atmospheres, in Figures 5.6, 5.7, 5.8, and 5.9. We further show an example of one grid’s goodness-of-fit as measured by the χ^2 statistic in Figure 5.10. We can see that the extreme, super-solar metallicities cannot describe the data, nor can a high (>1) C/O atmosphere; the likelihood of either extreme has been a point of contention in the exoplanet community (see Deming and Seager 2017 for a review). Instead, this preliminary analysis points toward a low C/O ratio, perhaps even subsolar, and a metallicity between 1 - $100\times$ solar; the atmosphere’s mean molecular weight must be close to our assumed H/He-rich lower bound, because we see such deep absorption. Low metallicity and C/O ratio both point toward a formation close to the central star, making HATS-7b more of a sub-Saturn than a super-Neptune, in contrast to the findings of Bakos et al. (2015).

We also see that the temperature should be considerably less than that of our assumed equilibrium temperature, $T_{eq} \sim 1065$ K. The models seem to favor a temperature in the range 500 - 700 K. Such a low temperature could simply be a consequence of observing the atmosphere at the limb; if the night side of the planet is truly cold, with little recirculation of heat from the day side, we could just be probing an intermediary temperature between the two extremes. A lower temperature could also be caused by a higher albedo; we assumed $A_B = 0.03$, but a significantly higher albedo could help explain the discrepancy.

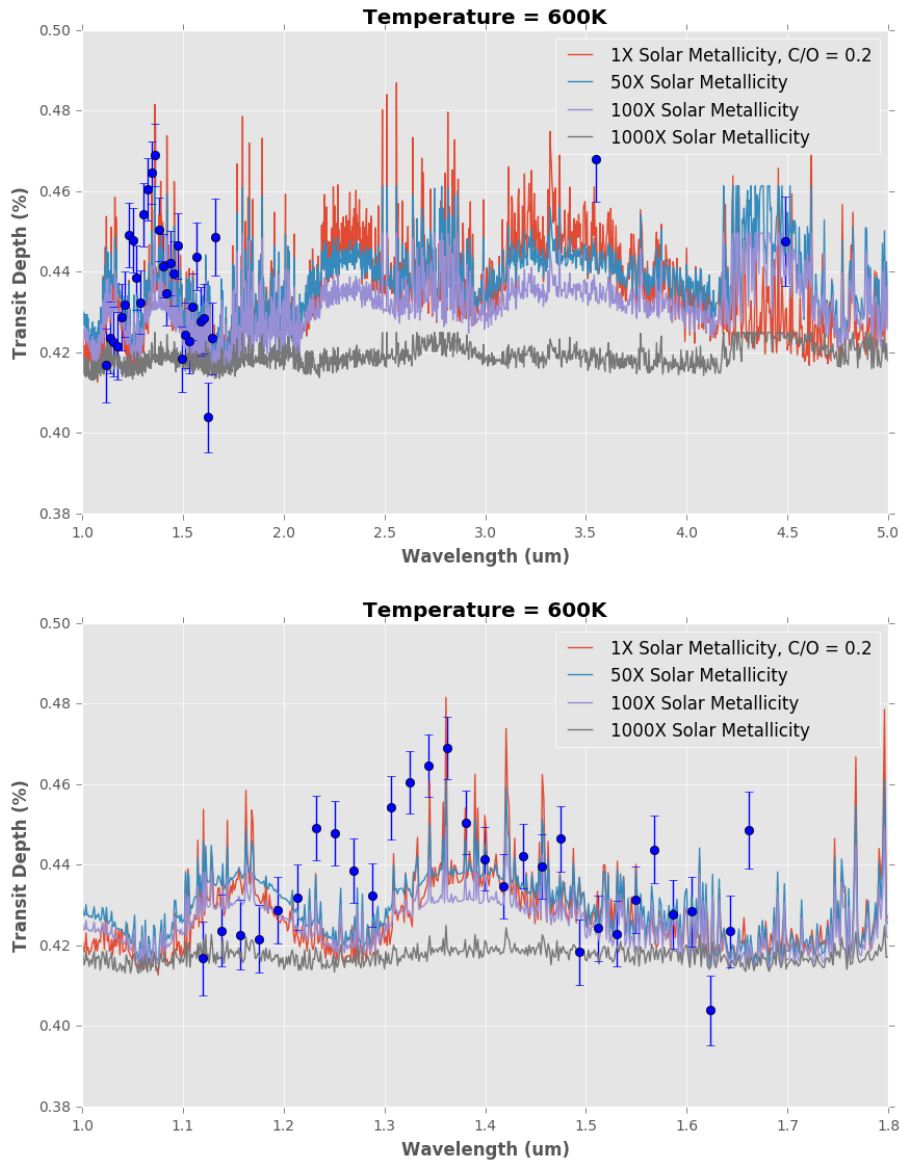


Figure 5.6 With the data overplotted in blue circles, four transmission spectrum models, all at a (relatively) warm 600 K, but different metallicities. Higher metallicity does increase the supply of absorbing species (i.e. molecules), but it also has a trade-off with scale height, and eventually, as we see here at 1000 \times solar abundance, where the mean molecular weight (μ) the lower scale height corresponds to much smaller features. The top panel includes the Spitzer points, while the bottom panel is zoomed in to the HST waveband.

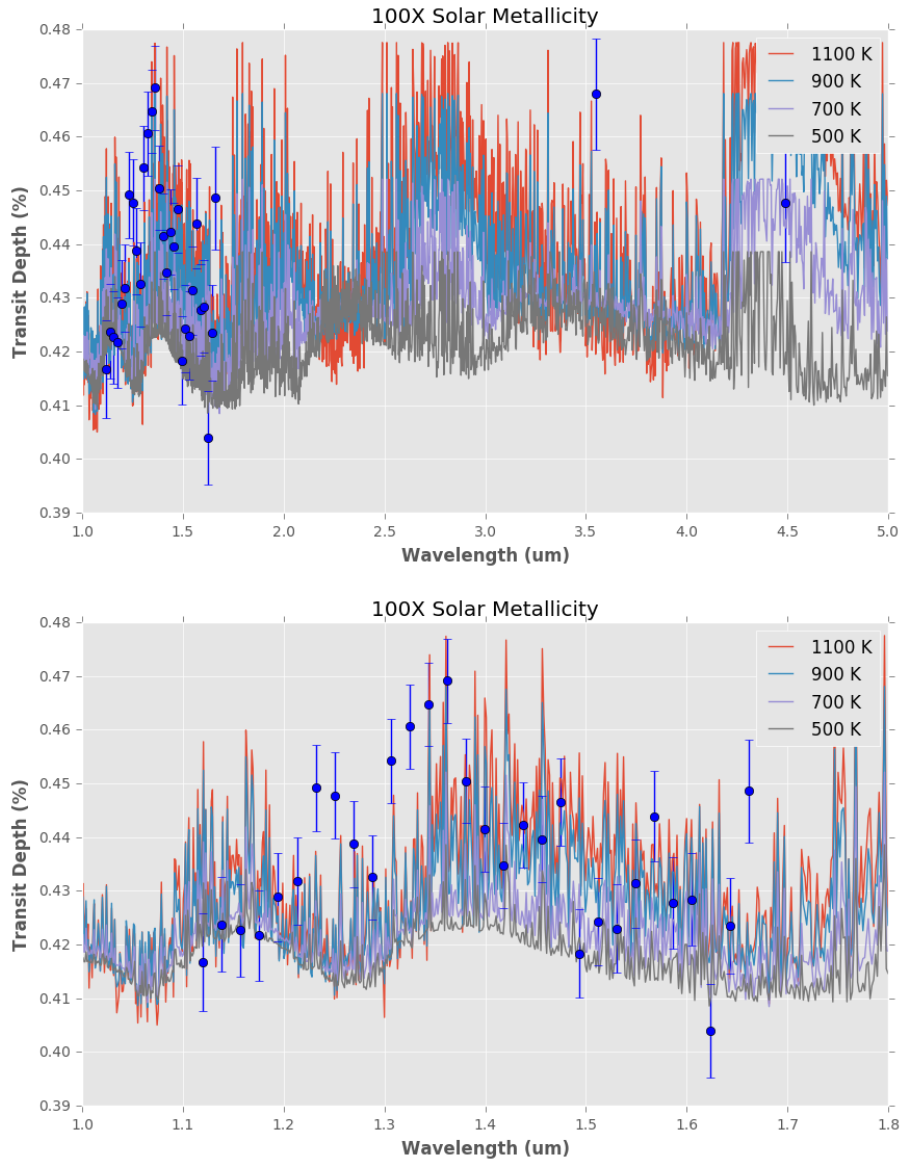


Figure 5.7 Same as Figure 5.6, but with the metallicity held constant at $100\times$ solar, and varying the temperature. Lower temperatures do indeed suppress the CO feature, but they also impact the prominence of the H₂O feature, as a reduced temperature reduces the scale height.

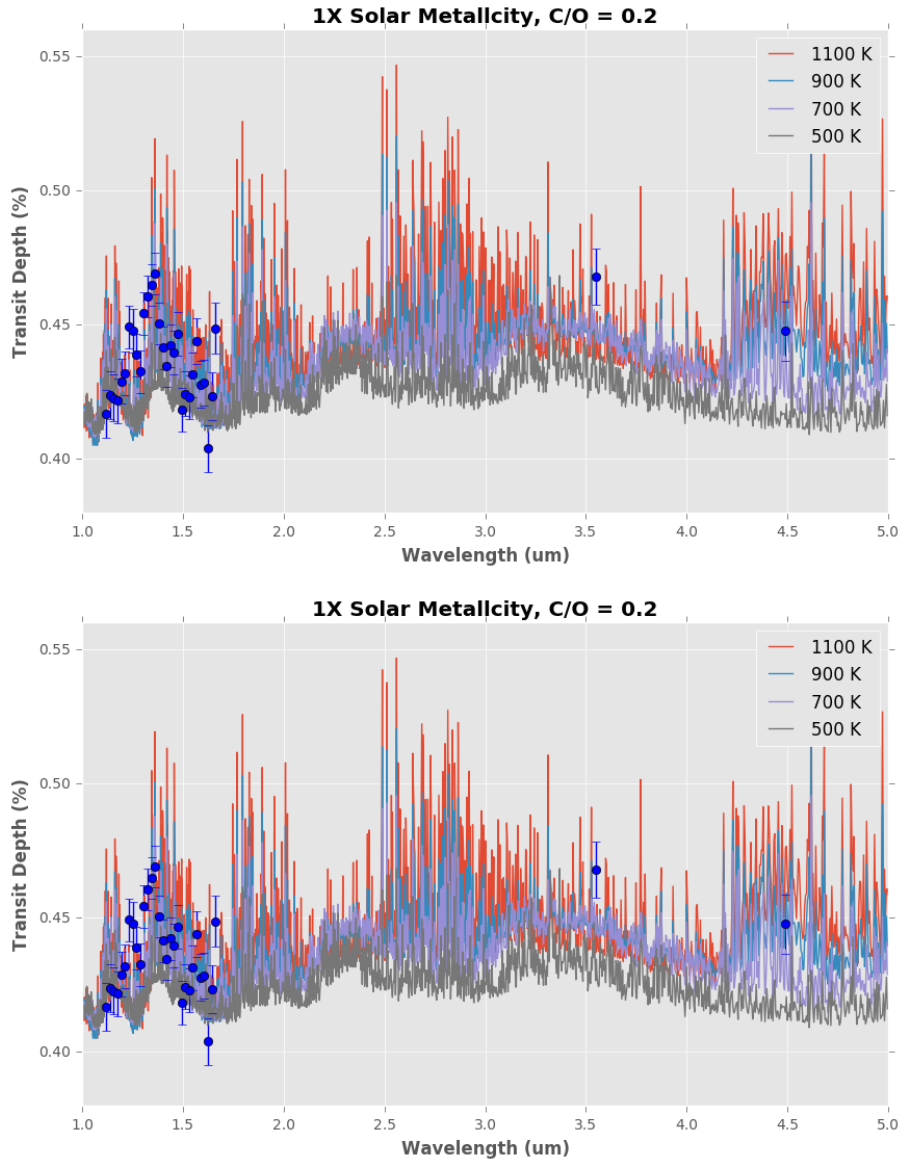


Figure 5.8 Same as Figures 5.6 and 5.7, but with the metallicity held constant at $1\times$ solar and the C/O ratio held constant at 0.2 (the solar value is approximately 0.5), and varying the temperature. Lower temperatures do indeed suppress the CO feature, but they also impact the prominence of the H₂O feature, as a reduced temperature reduces the scale height.

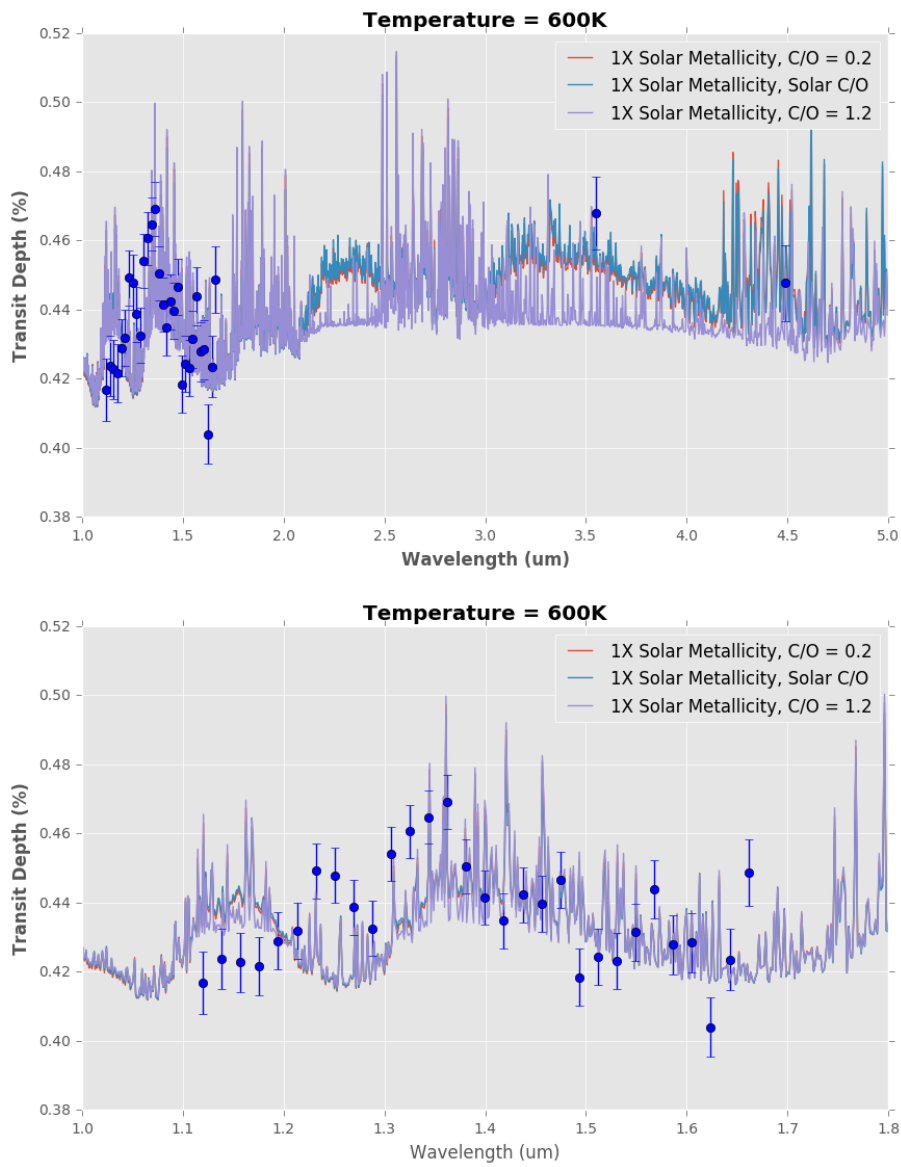


Figure 5.9 Same as Figures 5.6, 5.7, 5.8, but with the metallicity held constant at $1 \times$ solar, the temperature also held constant at 600K, and varying the C/O from 0.2, solar (0.5), and 1.2.

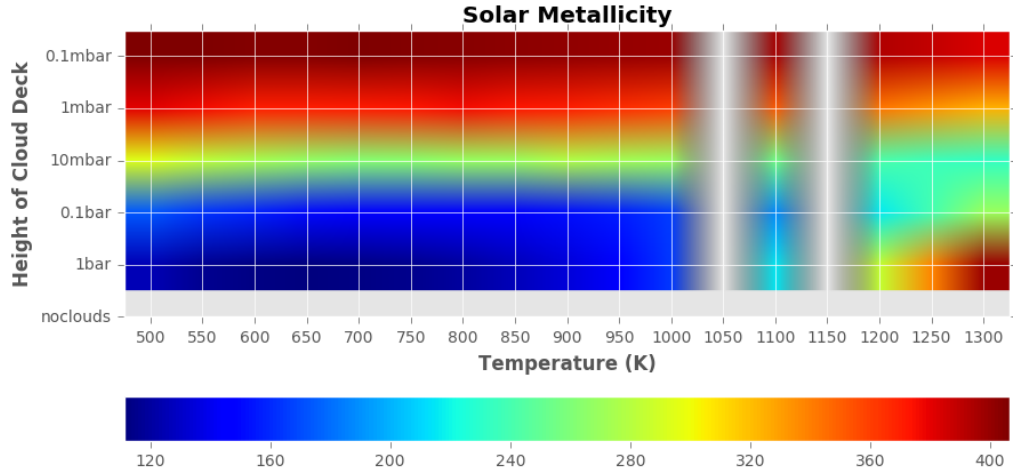


Figure 5.10 χ^2 goodness-of-fit measurement of the Exotransmit model spectra with various cloud heights and temperatures. While the grid is still coarse, we see evidence here that the planet probably does not have a high cloud layer, and that the spectrum is somewhat independent of temperature.

5.6 Conclusion

We have definitively detected water absorption in the atmosphere of HATS-7b, a hot sub-Saturn and valuable probe into the transition between ice- and gas-giant atmospheres. The absorption feature is clearly shaped in such a way as to imply a lower-than-expected temperature, and, in combination with mid-infrared *Spitzer* data, points toward a low- μ , low-C/O, and low-metallicity atmosphere, but more detailed modeling is required to constrain it further.

Observations of planets in the diverse class of sub-Saturns are essential to understanding planet formation and the still not well understood transition between ice giants and gas giants in our own Solar System. In particular, HATS-7b is joined by two other very similar (in mass and radius) planets orbiting very similar stars (in metallicity, temperature, and stellar type), HATS-8b (Bayliss et al., 2015) and

WASP-139b (Hellier et al., 2017). Comparing the spectra of these three similar planets, in similar environments, should yield more definitive insight into the range of possibilities for the atmospheres of hot super-Neptune planets, which occupy a transitional phase space not observable in our own Solar System (mass and size between the two pairs of ice giants and gas giants).

More generally, ground-based surveys have been the primary discoverers of exoplanets capable of spectroscopic follow-up, because they target bright, nearby stars; those planned and currently in operation will surely continue to provide a supply (e.g. the recently-announced sub-Saturns HATS-43b and HATS-46b Brahm et al. 2017), but the Transiting Exoplanet Survey Satellite (TESS, Ricker et al. 2014), launching in the spring of 2018, is estimated to find ~ 1700 planets around nearby, bright stars, the majority of which will be smaller than Saturn (Sullivan et al., 2015). Such planets will be prime targets for HST and JWST follow-up characterization.

5.7 Acknowledgements

Some of the data presented in this thesis were obtained from the Mikulski Archive for Space Telescopes (MAST). STScI is operated by the Association of Universities for Research in Astronomy, Inc., under NASA contract NAS5-26555. Support for MAST for non-HST data is provided by the NASA Office of Space Science via grant NNX09AF08G and by other grants and contracts.

Table 5.1. The HST Sub-Saturns

Planet Name	Discovery	HST Characterization
GJ 1214b	Charbonneau et al. (2009)	Berta et al. (2012) Kreidberg et al. (2014)
HAT-p-26b	Hartman et al. (2011)	Wakeford et al. (2017a)
GJ 436b	Butler et al. (2004)	Knutson et al. (2014a)
HAT-p-11b	Bakos et al. (2010)	Fraine et al. (2014)
GJ 3470b	(Bonfils et al., 2012)	Ehrenreich et al. (2014)
HATS-7b	Bakos et al. (2015)	This work

Table 5.2. HATS-7 Summary of Transit Observations

Observatory	Filter (Wavelength)	Date
HST/WFC3 (Visit A)	G141 (1.1 - 1.7 μm)	2016-03-17
HST/WFC3 (Visit B)	G141 (1.1 - 1.7 μm)	2016-03-20
Warm Spitzer/IRAC	3.6 μm	2016-11-01
Warm Spitzer/IRAC	4.5 μm	2016-11-04

Table 5.3. HATS-7 HST Observation Details

	Visit A	Visit B
Subarray	SQ256SUB	SQ256SUB
Number of samples (NSAMP)	15	15
Sample integration time	22.35 s	22.35 s
Number of Exposures	34 ^a	34
Scan rate	0.02''/sec	0.022''/sec

^aBoth visits took 38 frames, but four were shorter scans taken at the very end of orbits, and therefore cut off early as HST went behind the Earth.

Table 5.4. HATS-7 System Parameters

Parameter	Discovery Value (Bakos et al., 2015)	This Work
The Star: HATS-7		
R_{star} (R_{\odot})	$0.815^{+0.049}_{-0.035}$	$0.768^{+0.022}_{-0.017}$
T_{eff} (K)	4985 ± 50	4975^{+48}_{-49}
$\log g_{star}$ (cgs)	4.545 ± 0.045	$4.596^{+0.013}_{-0.021}$
M_{star} (M_{\odot})	0.849 ± 0.027	$0.847^{+0.042}_{-0.041}$
[Fe/H]	+ 0.25	+ 0.256 \pm 0.078
The Planet: HATS-7b		
P (days)	$3.1853150 \pm 5.4 \times 10^{-6}$	$3.1853228 \pm 6.1 \times 10^{-6}$
a (AU)	0.040124 ± 0.00043	$0.04008 \pm 6.6 \times 10^{-4}$
R_p (R_J)	$0.563^{+0.046}_{-0.034}$	$0.550^{+0.020}_{-0.014}$
e	< 0.170	TBA
i ($^{\circ}$)	87.92 ± 0.75	$89.35^{+0.45}_{-0.68}$
M_p (M_J)	0.12 ± 0.012	0.119 ± 0.015
T_0 (days)	$2456528.29697 \pm 0.00058^a$	$2457366.03691^{+0.00095}_{-0.00096}$
T_{eq} (K)	1084 ± 32^b	1050^{+16}_{-13}
$\log g_p$ (cgs)	2.968 ± 0.076	$2.984^{+0.056}_{-0.064}$
$\langle F \rangle$ ($\text{erg s}^{-1} \text{cm}^{-2}$)	$3.12^{+0.42}_{-0.42} \times 10^8$	$2.76^{+0.17}_{-0.13} \times 10^8$

^aThe Bakos et al. (2015) reported times are in BJD calculated directly from UTC, without correction for leap seconds.

^bThe Bakos et al. (2015) calculated planet equilibrium temperature assuming $A_B = 0$ and that flux is re-radiated from the full planet surface.

Table 5.5. HATS-7 Observed Transmission Spectrum

(μm)	$\Delta\lambda$	(R_p^2/R_{star}^2)	$(\Delta R_p^2/R_{star}^2)$
1.1197493	0.018671	0.0041676353	0.00022709446
1.1384203	0.018671	0.0042370760	0.00021988859
1.1570912	0.018671	0.0042267045	0.00021597675
1.1757622	0.018671	0.0042164990	0.00021102364
1.1944331	0.018671	0.0042882563	0.00020716208
1.2131041	0.018671	0.0043188610	0.00020337119
1.2317750	0.018671	0.0044917121	0.00020054474
1.2504459	0.018671	0.0044775123	0.00019956969
1.2691169	0.018671	0.0043867379	0.00019948598
1.2877878	0.018671	0.0043249993	0.00019754332
1.3064588	0.018671	0.0045418130	0.00019578697
1.3251297	0.018671	0.0046054104	0.00019505682
1.3438007	0.018671	0.0046472557	0.00019353591
1.3624716	0.018671	0.0046906376	0.00019432143
1.3811426	0.018671	0.0045046283	0.00019647824
1.3998135	0.018671	0.0044145955	0.00019768741
1.4184844	0.018671	0.0043472928	0.00019824179
1.4371554	0.018671	0.0044219174	0.00019879137
1.4558263	0.018671	0.0043957565	0.00020007006
1.4744973	0.018671	0.0044647908	0.00020232486
1.4931682	0.018671	0.0041834015	0.00020455347
1.5118392	0.018671	0.0042426826	0.00020468667

Table 5.5 (cont'd)

(μm)	$\Delta\lambda$	(R_p^2/R_{star}^2)	$(\Delta R_p^2/R_{star}^2)$
1.5305101	0.018671	0.0042295157	0.00020424201
1.5491811	0.018671	0.0043136175	0.00020624797
1.5678520	0.018671	0.0044384711	0.00021054874
1.5865229	0.018671	0.0042776020	0.00021386801
1.6051939	0.018671	0.0042837474	0.00021505402
1.6238648	0.018671	0.0040391067	0.00021795709
1.6425358	0.018671	0.0042347465	0.00022288181
1.6612067	0.018671	0.0044857380	0.00023876771
3.55	0.74	0.004679	1.04×10^{-4}
4.49	1.02	0.004476	1.4×10^{-4}

Bibliography

- R. Alonso, M. Auvergne, A. Baglin, M. Ollivier, C. Moutou, D. Rouan, H. J. Deeg, S. Aigrain, J. M. Almenara, M. Barbieri, P. Barge, W. Benz, P. Bordé, F. Bouchy, R. de La Reza, M. Deleuil, R. Dvorak, A. Erikson, M. Fridlund, M. Gillon, P. Gondoin, T. Guillot, A. Hatzes, G. Hébrard, P. Kabath, L. Jorda, H. Lammer, A. Léger, A. Llebaria, B. Loeillet, P. Magain, M. Mayor, T. Mazeh, M. Pätzold, F. Pepe, F. Pont, D. Queloz, H. Rauer, A. Shporer, J. Schneider, B. Stecklum, S. Udry, and G. Wuchterl. Transiting exoplanets from the CoRoT space mission. II. CoRoT-Exo-2b: a transiting planet around an active G star. *A&A*, 482:L21–L24, May 2008. doi: 10.1051/0004-6361:200809431.
- R. Alonso, T. Guillot, T. Mazeh, S. Aigrain, A. Alapini, P. Barge, A. Hatzes, and F. Pont. The secondary eclipse of the transiting exoplanet CoRoT-2b. *A&A*, 501: L23–L26, July 2009. doi: 10.1051/0004-6361/200912505.
- R. Alonso, H. J. Deeg, P. Kabath, and M. Rabus. Ground-based Near-infrared Observations of the Secondary Eclipse of CoRoT-2b. *AJ*, 139:1481–1485, April 2010. doi: 10.1088/0004-6256/139/4/1481.
- S. M. Andrews and J. P. Williams. High-Resolution Submillimeter Constraints on Circumstellar Disk Structure. *ApJ*, 659:705–728, April 2007. doi: 10.1086/511741.
- E. Asphaug and W. Benz. Density of comet Shoemaker-Levy 9 deduced by modelling breakup of the parent 'rubble pile'. *Nature*, 370:120–124, July 1994. doi: 10.1038/370120a0.
- G. Á. Bakos, G. Torres, A. Pál, J. Hartman, G. Kovács, R. W. Noyes, D. W. Latham, D. D. Sasselov, B. Sipócz, G. A. Esquerdo, D. A. Fischer, J. A. Johnson, G. W. Marcy, R. P. Butler, H. Isaacson, A. Howard, S. Vogt, G. Kovács, J. Fernandez, A. Moór, R. P. Stefanik, J. Lázár, I. Papp, and P. Sári. HAT-P-11b: A Super-Neptune Planet Transiting a Bright K Star in the Kepler Field. *ApJ*, 710:1724–1745, February 2010. doi: 10.1088/0004-637X/710/2/1724.
- G. Á. Bakos, Z. Csubry, K. Penev, D. Bayliss, A. Jordán, C. Afonso, J. D. Hartman, T. Henning, G. Kovács, R. W. Noyes, B. Béky, V. Suc, B. Csák, M. Rabus, J. Lázár, I. Papp, P. Sári, P. Conroy, G. Zhou, P. D. Sackett, B. Schmidt,

- L. Mancini, D. D. Sasselov, and K. Ueltzhoeffer. HATSouth: A Global Network of Fully Automated Identical Wide-Field Telescopes. *PASP*, 125:154, February 2013. doi: 10.1086/669529.
- G. Á. Bakos, K. Penev, D. Bayliss, J. D. Hartman, G. Zhou, R. Brahm, L. Mancini, M. de Val-Borro, W. Bhatti, A. Jordán, M. Rabus, N. Espinoza, Z. Csubry, A. W. Howard, B. J. Fulton, L. A. Buchhave, S. Ciceri, T. Henning, B. Schmidt, H. Isaacson, R. W. Noyes, G. W. Marcy, V. Suc, A. R. Howe, A. S. Burrows, J. Lázár, I. Papp, and P. Sári. HATS-7b: A Hot Super Neptune Transiting a Quiet K Dwarf Star. *ApJ*, 813:111, November 2015. doi: 10.1088/0004-637X/813/2/111.
- I. Baraffe, G. Chabrier, J. Fortney, and C. Sotin. Planetary Internal Structures. *Protostars and Planets VI*, pages 763–786, 2014. doi: 10.2458/azu_uapress-9780816531240-ch033.
- A. J. Barker. Three-dimensional simulations of internal wave breaking and the fate of planets around solar-type stars. *MNRAS*, 414:1365–1378, June 2011. doi: 10.1111/j.1365-2966.2011.18468.x.
- A. J. Barker and G. I. Ogilvie. On the tidal evolution of Hot Jupiters on inclined orbits. *MNRAS*, 395:2268–2287, June 2009. doi: 10.1111/j.1365-2966.2009.14694.x.
- A. J. Barker and G. I. Ogilvie. On internal wave breaking and tidal dissipation near the centre of a solar-type star. *MNRAS*, 404:1849–1868, June 2010. doi: 10.1111/j.1365-2966.2010.16400.x.
- A. J. Barker and G. I. Ogilvie. Stability analysis of a tidally excited internal gravity wave near the centre of a solar-type star. *MNRAS*, 417:745–761, October 2011. doi: 10.1111/j.1365-2966.2011.19322.x.
- N. E. Batalha and M. R. Line. Information Content Analysis for Selection of Optimal JWST Observing Modes for Transiting Exoplanet Atmospheres. *AJ*, 153:151, April 2017. doi: 10.3847/1538-3881/aa5faa.
- K. Batygin and M. E. Brown. Evidence for a Distant Giant Planet in the Solar System. *AJ*, 151:22, February 2016. doi: 10.3847/0004-6256/151/2/22.
- K. Batygin, P. H. Bodenheimer, and G. P. Laughlin. In Situ Formation and Dynamical Evolution of Hot Jupiter Systems. *ApJ*, 829:114, October 2016. doi: 10.3847/0004-637X/829/2/114.
- D. Bayliss, J. D. Hartman, G. Á. Bakos, K. Penev, G. Zhou, R. Brahm, M. Rabus, A. Jordán, L. Mancini, M. de Val-Borro, W. Bhatti, N. Espinoza, Z. Csubry, A. W. Howard, B. J. Fulton, L. A. Buchhave, T. Henning, B. Schmidt, S. Ciceri, R. W. Noyes, H. Isaacson, G. W. Marcy, V. Suc, J. Lázár, I. Papp, and P. Sári. HATS-8b: A Low-density Transiting Super-Neptune. *AJ*, 150:49, August 2015. doi: 10.1088/0004-6256/150/2/49.

- J. L. Bean, E. Miller-Ricci Kempton, and D. Homeier. A ground-based transmission spectrum of the super-Earth exoplanet GJ 1214b. *Nature*, 468:669–672, December 2010. doi: 10.1038/nature09596.
- J. L. Bean, J.-M. Désert, P. Kabath, B. Stalder, S. Seager, E. Miller-Ricci Kempton, Z. K. Berta, D. Homeier, S. Walsh, and A. Seifahrt. The Optical and Near-infrared Transmission Spectrum of the Super-Earth GJ 1214b: Further Evidence for a Metal-rich Atmosphere. *ApJ*, 743:92, December 2011. doi: 10.1088/0004-637X/743/1/92.
- J. L. Bean, J.-M. Désert, A. Seifahrt, N. Madhusudhan, I. Chilingarian, D. Homeier, and A. Szentgyorgyi. Ground-based Transit Spectroscopy of the Hot-Jupiter WASP-19b in the Near-infrared. *ApJ*, 771:108, July 2013. doi: 10.1088/0004-637X/771/2/108.
- T. G. Beatty, N. Madhusudhan, A. Tsiaras, M. Zhao, R. L. Gilliland, H. A. Knutson, A. Shporer, and J. T. Wright. Evidence for Atmospheric Cold-trap Processes in the Non-inverted Emission Spectrum of Kepler-13Ab Using HST/WFC3. *ArXiv e-prints*, December 2016.
- Z. K. Berta, D. Charbonneau, J.-M. Désert, E. Miller-Ricci Kempton, P. R. McCullough, C. J. Burke, J. J. Fortney, J. Irwin, P. Nutzman, and D. Homeier. The Flat Transmission Spectrum of the Super-Earth GJ1214b from Wide Field Camera 3 on the Hubble Space Telescope. *ApJ*, 747:35, March 2012. doi: 10.1088/0004-637X/747/1/35.
- J. L. Birkby, R. J. de Kok, M. Brogi, E. J. W. de Mooij, H. Schwarz, S. Albrecht, and I. A. G. Snellen. Detection of water absorption in the day side atmosphere of HD 189733 b using ground-based high-resolution spectroscopy at 3.2 μm . *MNRAS*, 436:L35–L39, November 2013. doi: 10.1093/mnras/slt107.
- J. L. Birkby, M. Cappetta, P. Cruz, J. Koppenhoefer, O. Ivanyuk, A. J. Mustill, S. T. Hodgkin, D. J. Pinfield, B. Sipócz, G. Kovács, R. Saglia, Y. Pavlenko, D. Barrado, A. Bayo, D. Campbell, S. Catalan, L. Fossati, M.-C. Gálvez-Ortiz, M. Kenworthy, J. Lillo-Box, E. L. Martín, D. Mislis, E. J. W. de Mooij, S. V. Nefs, I. A. G. Snellen, H. Stoev, J. Zendejas, C. del Burgo, J. Barnes, N. Goulding, C. A. Haswell, M. Kuznetsov, N. Lodieu, F. Murgas, E. Palle, E. Solano, P. Steele, and R. Tata. WTS-2 b: a hot Jupiter orbiting near its tidal destruction radius around a K dwarf. *MNRAS*, 440:1470–1489, May 2014. doi: 10.1093/mnras/stu343.
- R. Bohlin, S. E. Deustua, and N. Pirzkal. IR Grism Wavelength Solutions Using the Zero Order Image as the Reference Point. Technical report, STScI, June 2015.
- S. J. Bolton, A. Adriani, V. Adumitroaie, M. Allison, J. Anderson, S. Atreya, J. Bloxham, S. Brown, J. E. P. Connerney, E. DeJong, W. Folkner, D. Gautier, D. Grassi, S. Gulkis, T. Guillot, C. Hansen, W. B. Hubbard, L. Iess, A. Ingersoll, M. Janssen, J. Jorgensen, Y. Kaspi, S. M. Levin, C. Li, J. Lunine, Y. Miguel,

- A. Mura, G. Orton, T. Owen, M. Ravine, E. Smith, P. Steffes, E. Stone, D. Stevenson, R. Thorne, J. Waite, D. Durante, R. W. Ebert, T. K. Greathouse, V. Hue, M. Parisi, J. R. Szalay, and R. Wilson. Jupiter’s interior and deep atmosphere: The initial pole-to-pole passes with the Juno spacecraft. *Science*, 356:821–825, May 2017. doi: 10.1126/science.aal2108.
- A. Bonfanti, S. Ortolani, and V. Nascimbeni. Age consistency between exoplanet hosts and field stars. *A&A*, 585:A5, January 2016. doi: 10.1051/0004-6361/201527297.
- X. Bonfils, M. Gillon, S. Udry, D. Armstrong, F. Bouchy, X. Delfosse, T. Forveille, A. Fumel, E. Jehin, M. Lendl, C. Lovis, M. Mayor, J. McCormac, V. Neves, F. Pepe, C. Perrier, D. Pollaco, D. Queloz, and N. C. Santos. A hot Uranus transiting the nearby M dwarf GJ 3470. Detected with HARPS velocimetry. Captured in transit with TRAPPIST photometry. *A&A*, 546:A27, October 2012. doi: 10.1051/0004-6361/201219623.
- W. J. Borucki, D. Koch, G. Basri, N. Batalha, T. Brown, D. Caldwell, J. Caldwell, J. Christensen-Dalsgaard, W. D. Cochran, E. DeVore, E. W. Dunham, A. K. Dupree, T. N. Gautier, J. C. Geary, R. Gilliland, A. Gould, S. B. Howell, J. M. Jenkins, Y. Kondo, D. W. Latham, G. W. Marcy, S. Meibom, H. Kjeldsen, J. J. Lissauer, D. G. Monet, D. Morrison, D. Sasselov, J. Tarter, A. Boss, D. Brownlee, T. Owen, D. Buzasi, D. Charbonneau, L. Doyle, J. Fortney, E. B. Ford, M. J. Holman, S. Seager, J. H. Steffen, W. F. Welsh, J. Rowe, H. Anderson, L. Buchhave, D. Ciardi, L. Walkowicz, W. Sherry, E. Horch, H. Isaacson, M. E. Everett, D. Fischer, G. Torres, J. A. Johnson, M. Endl, P. MacQueen, S. T. Bryson, J. Dotson, M. Haas, J. Kolodziejczak, J. Van Cleve, H. Chandrasekaran, J. D. Twicken, E. V. Quintana, B. D. Clarke, C. Allen, J. Li, H. Wu, P. Tenenbaum, E. Verner, F. Bruhweiler, J. Barnes, and A. Prsa. Kepler Planet-Detection Mission: Introduction and First Results. *Science*, 327:977, February 2010. doi: 10.1126/science.1185402.
- A. P. Boss. Giant planet formation by gravitational instability. *Science*, 276:1836–1839, 1997. doi: 10.1126/science.276.5320.1836.
- A. P. Boss. Formation of gas and ice giant planets. *Earth and Planetary Science Letters*, 202:513–523, September 2002. doi: 10.1016/S0012-821X(02)00808-7.
- A. P. Boss. Rapid Formation of Outer Giant Planets by Disk Instability. *ApJ*, 599: 577–581, December 2003. doi: 10.1086/379163.
- F. Bouchy, F. Pont, C. Melo, N. C. Santos, M. Mayor, D. Queloz, and S. Udry. Doppler follow-up of OGLE transiting companions in the Galactic bulge. *A&A*, 431:1105–1121, March 2005. doi: 10.1051/0004-6361:20041723.
- R. Brahm, J. D. Hartman, A. Jordan, G. A. Bakos, N. Espinoza, M. Rabus, W. Bhatti, K. Penev, P. Sarkis, V. Suc, Z. Csubry, D. Bayliss, J. Bento, G. Zhou,

- L. Mancini, T. Henning, S. Ciceri, M. de Val-Borro, S. Shectman, J. D. Crane, P. Arriagada, P. Butler, J. Teske, I. Thompson, D. Osip, M. Diaz, B. Schmidt, J. Lazar, I. Papp, and P. Sari. HATS-43b, HATS-44b, HATS-45b, and HATS-46b: Four Short Period Transiting Giant Planets in the Neptune-Jupiter Mass Range. *ArXiv e-prints*, July 2017.
- J. M. Brewer, D. A. Fischer, and N. Madhusudhan. C/O and O/H Ratios Suggest Some Hot Jupiters Originate Beyond the Snow Line. *AJ*, 153:83, February 2017. doi: 10.3847/1538-3881/153/2/83.
- M. Brogi, R. J. de Kok, S. Albrecht, I. A. G. Snellen, J. L. Birkby, and H. Schwarz. Rotation and Winds of Exoplanet HD 189733 b Measured with High-dispersion Transmission Spectroscopy. *ApJ*, 817:106, February 2016. doi: 10.3847/0004-637X/817/2/106.
- T. M. Brown. Transmission Spectra as Diagnostics of Extrasolar Giant Planet Atmospheres. *ApJ*, 553:1006–1026, June 2001. doi: 10.1086/320950.
- A. Burrows, W. B. Hubbard, J. I. Lunine, and J. Liebert. The theory of brown dwarfs and extrasolar giant planets. *Reviews of Modern Physics*, 73:719–765, July 2001. doi: 10.1103/RevModPhys.73.719.
- A. Burrows, I. Hubeny, J. Budaj, H. A. Knutson, and D. Charbonneau. Theoretical Spectral Models of the Planet HD 209458b with a Thermal Inversion and Water Emission Bands. *ApJL*, 668:L171–L174, October 2007. doi: 10.1086/522834.
- A. Burrows, J. Budaj, and I. Hubeny. Theoretical Spectra and Light Curves of Close-in Extrasolar Giant Planets and Comparison with Data. *ApJ*, 678:1436–1457, May 2008a. doi: 10.1086/533518.
- A. Burrows, L. Ibgui, and I. Hubeny. Optical Albedo Theory of Strongly Irradiated Giant Planets: The Case of HD 209458b. *ApJ*, 682:1277–1282, August 2008b. doi: 10.1086/589824.
- A. Burrows, E. Rauscher, D. S. Spiegel, and K. Menou. Photometric and Spectral Signatures of Three-dimensional Models of Transiting Giant Exoplanets. *ApJ*, 719:341–350, August 2010. doi: 10.1088/0004-637X/719/1/341.
- R. P. Butler, S. S. Vogt, G. W. Marcy, D. A. Fischer, J. T. Wright, G. W. Henry, G. Laughlin, and J. J. Lissauer. A Neptune-Mass Planet Orbiting the Nearby M Dwarf GJ 436. *ApJ*, 617:580–588, December 2004. doi: 10.1086/425173.
- K. L. Cahoy, M. S. Marley, and J. J. Fortney. Exoplanet Albedo Spectra and Colors as a Function of Planet Phase, Separation, and Metallicity. *ApJ*, 724:189–214, November 2010. doi: 10.1088/0004-637X/724/1/189.
- D. Charbonneau, T. M. Brown, D. W. Latham, and M. Mayor. Detection of Planetary Transits Across a Sun-like Star. *ApJL*, 529:L45–L48, January 2000. doi: 10.1086/312457.

- D. Charbonneau, T. M. Brown, R. W. Noyes, and R. L. Gilliland. Detection of an Extrasolar Planet Atmosphere. *ApJ*, 568:377–384, March 2002. doi: 10.1086/338770.
- D. Charbonneau, L. E. Allen, S. T. Megeath, G. Torres, R. Alonso, T. M. Brown, R. L. Gilliland, D. W. Latham, G. Mandushev, F. T. O’Donovan, and A. Sozzetti. Detection of Thermal Emission from an Extrasolar Planet. *ApJ*, 626:523–529, June 2005. doi: 10.1086/429991.
- D. Charbonneau, Z. K. Berta, J. Irwin, C. J. Burke, P. Nutzman, L. A. Buchhave, C. Lovis, X. Bonfils, D. W. Latham, S. Udry, R. A. Murray-Clay, M. J. Holman, E. E. Falco, J. N. Winn, D. Queloz, F. Pepe, M. Mayor, X. Delfosse, and T. Forveille. A super-Earth transiting a nearby low-mass star. *Nature*, 462: 891–894, December 2009. doi: 10.1038/nature08679.
- A. Claret. A new non-linear limb-darkening law for LTE stellar atmosphere models. Calculations for $-5.0 \leq \log[M/H] \leq +1$, $2000 \text{ K} \leq T_{eff} \leq 50000 \text{ K}$ at several surface gravities. *A&A*, 363:1081–1190, November 2000.
- J. A. Crooke, A. Roberge, S. D. Domagal-Goldman, A. M. Mandell, M. R. Bolcar, N. M. Rioux, M. R. Perez, and E. C. Smith. Status and path forward for the large ultraviolet/optical/infrared surveyor (LUVOIR) mission concept study. In *Space Telescopes and Instrumentation 2016: Optical, Infrared, and Millimeter Wave*, volume 9904 of *Proc. SPIE*, page 99044R, July 2016. doi: 10.1117/12.2233084.
- I. J. M. Crossfield. Observations of Exoplanet Atmospheres. *PASP*, 127:941–960, October 2015. doi: 10.1086/683115.
- N. Crouzet, P. R. McCullough, D. Deming, and N. Madhusudhan. Water Vapor in the Spectrum of the Extrasolar Planet HD 189733b. II. The Eclipse. *ApJ*, 795: 166, November 2014. doi: 10.1088/0004-637X/795/2/166.
- P. Cubillos, N. V. Erkaev, I. Juvan, L. Fossati, C. P. Johnstone, H. Lammer, M. Lendl, P. Odert, and K. G. Kislyakova. An overabundance of low-density Neptune-like planets. *MNRAS*, 466:1868–1879, April 2017a. doi: 10.1093/mnras/stw3103.
- P. Cubillos, J. Harrington, T. J. Loredo, N. B. Lust, J. Blečić, and M. Stemm. On Correlated-noise Analyses Applied to Exoplanet Light Curves. *AJ*, 153:3, January 2017b. doi: 10.3847/1538-3881/153/1/3.
- I. de Pater and J. J. Lissauer. *Planetary Sciences*. Cambridge University Press, July 2010.
- D. Deming. Planetary science: A cloudy view of exoplanets. *Nature*, 468:636–637, December 2010. doi: 10.1038/468636a.
- D. Deming, S. Seager, L. J. Richardson, and J. Harrington. Infrared radiation from an extrasolar planet. *Nature*, 434:740–743, March 2005. doi: 10.1038/nature03507.

- D. Deming, H. Knutson, E. Agol, J.-M. Desert, A. Burrows, J. J. Fortney, D. Charbonneau, N. B. Cowan, G. Laughlin, J. Langton, A. P. Showman, and N. K. Lewis. Warm Spitzer Photometry of the Transiting Exoplanets CoRoT-1 and CoRoT-2 at Secondary Eclipse. *ApJ*, 726:95, January 2011. doi: 10.1088/0004-637X/726/2/95.
- D. Deming, A. Wilkins, P. McCullough, A. Burrows, J. J. Fortney, E. Agol, I. Dobbs-Dixon, N. Madhusudhan, N. Crouzet, J.-M. Desert, R. L. Gilliland, K. Haynes, H. A. Knutson, M. Line, Z. Magic, A. M. Mandell, S. Ranjan, D. Charbonneau, M. Clampin, S. Seager, and A. P. Showman. Infrared Transmission Spectroscopy of the Exoplanets HD 209458b and XO-1b Using the Wide Field Camera-3 on the Hubble Space Telescope. *ApJ*, 774:95, September 2013. doi: 10.1088/0004-637X/774/2/95.
- D. Deming, H. Knutson, J. Kammer, B. J. Fulton, J. Ingalls, S. Carey, A. Burrows, J. J. Fortney, K. Todorov, E. Agol, N. Cowan, J.-M. Desert, J. Fraine, J. Langton, C. Morley, and A. P. Showman. Spitzer Secondary Eclipses of the Dense, Modestly-irradiated, Giant Exoplanet HAT-P-20b Using Pixel-level Decorrelation. *ApJ*, 805:132, June 2015. doi: 10.1088/0004-637X/805/2/132.
- L. D. Deming and S. Seager. Illusion and reality in the atmospheres of exoplanets. *Journal of Geophysical Research (Planets)*, 122:53–75, January 2017. doi: 10.1002/2016JE005155.
- B.-O. Demory and S. Seager. Lack of Inflated Radii for Kepler Giant Planet Candidates Receiving Modest Stellar Irradiation. *ApJS*, 197:12, November 2011. doi: 10.1088/0067-0049/197/1/12.
- J.-M. Désert, J. Bean, E. Miller-Ricci Kempton, Z. K. Berta, D. Charbonneau, J. Irwin, J. Fortney, C. J. Burke, and P. Nutzman. Observational Evidence for a Metal-rich Atmosphere on the Super-Earth GJ1214b. *ApJL*, 731:L40, April 2011. doi: 10.1088/2041-8205/731/2/L40.
- I. Dobbs-Dixon and E. Agol. Three-dimensional radiative-hydrodynamical simulations of the highly irradiated short-period exoplanet HD 189733b. *MNRAS*, 435:3159–3168, November 2013. doi: 10.1093/mnras/stt1509.
- A. P. Doyle, B. Smalley, P. F. L. Maxted, D. R. Anderson, A. C. Cameron, M. Gillon, C. Hellier, D. Pollacco, D. Queloz, A. H. M. J. Triaud, and R. G. West. Accurate spectroscopic parameters of WASP planet host stars. *MNRAS*, 428:3164–3172, February 2013. doi: 10.1093/mnras/sts267.
- B. T. Draine. Interstellar Dust Grains. *ARA&A*, 41:241–289, 2003. doi: 10.1146/annurev.astro.41.011802.094840.
- D. Ehrenreich and J.-M. Désert. Mass-loss rates for transiting exoplanets. *A&A*, 529:A136, May 2011. doi: 10.1051/0004-6361/201016356.

- D. Ehrenreich, X. Bonfils, C. Lovis, X. Delfosse, T. Forveille, M. Mayor, V. Neves, N. C. Santos, S. Udry, and D. Ségransan. Near-infrared transmission spectrum of the warm-Uranus GJ 3470b with the Wide Field Camera-3 on the Hubble Space Telescope. *A&A*, 570:A89, October 2014. doi: 10.1051/0004-6361/201423809.
- T. Encrenaz. Infrared spectroscopy of exoplanets: observational constraints. *Philosophical Transactions of the Royal Society of London Series A*, 372:20130083–20130083, March 2014. doi: 10.1098/rsta.2013.0083.
- B. Enoch, A. Collier Cameron, N. R. Parley, and L. Hebb. An improved method for estimating the masses of stars with transiting planets. *A&A*, 516:A33, June 2010. doi: 10.1051/0004-6361/201014326.
- R. Essick and N. N. Weinberg. Orbital Decay of Hot Jupiters Due to Nonlinear Tidal Dissipation within Solar-type Hosts. *ApJ*, 816:18, January 2016. doi: 10.3847/0004-637X/816/1/18.
- T. M. Evans, F. Pont, D. K. Sing, S. Aigrain, J. K. Barstow, J.-M. Désert, N. Gibson, K. Heng, H. A. Knutson, and A. Lecavelier des Etangs. The Deep Blue Color of HD 189733b: Albedo Measurements with Hubble Space Telescope/Space Telescope Imaging Spectrograph at Visible Wavelengths. *ApJL*, 772:L16, August 2013. doi: 10.1088/2041-8205/772/2/L16.
- D. Foreman-Mackey, D. W. Hogg, D. Lang, and J. Goodman. emcee: The MCMC Hammer. *PASP*, 125:306–312, March 2013. doi: 10.1086/670067.
- J. J. Fortney and N. Nettelmann. The Interior Structure, Composition, and Evolution of Giant Planets. *SSRv*, 152:423–447, May 2010. doi: 10.1007/s11214-009-9582-x.
- J. J. Fortney, M. S. Marley, and J. W. Barnes. Planetary Radii across Five Orders of Magnitude in Mass and Stellar Insolation: Application to Transits. *ApJ*, 659:1661–1672, April 2007. doi: 10.1086/512120.
- J. J. Fortney, K. Lodders, M. S. Marley, and R. S. Freedman. A Unified Theory for the Atmospheres of the Hot and Very Hot Jupiters: Two Classes of Irradiated Atmospheres. *ApJ*, 678:1419–1435, May 2008. doi: 10.1086/528370.
- J. J. Fortney, M. Shabram, A. P. Showman, Y. Lian, R. S. Freedman, M. S. Marley, and N. K. Lewis. Transmission Spectra of Three-Dimensional Hot Jupiter Model Atmospheres. *ApJ*, 709:1396–1406, February 2010. doi: 10.1088/0004-637X/709/2/1396.
- L. Fossati, N. V. Erkaev, H. Lammer, P. E. Cubillos, P. Odert, I. Juvan, K. G. Kislyakova, M. Lendl, D. Kubyschkina, and S. J. Bauer. Aeronomical constraints to the minimum mass and maximum radius of hot low-mass planets. *A&A*, 598:A90, February 2017. doi: 10.1051/0004-6361/201629716.

- J. Fraine, D. Deming, B. Benneke, H. Knutson, A. Jordán, N. Espinoza, N. Madhusudhan, A. Wilkins, and K. Todorov. Water vapour absorption in the clear atmosphere of a Neptune-sized exoplanet. *Nature*, 513:526–529, September 2014. doi: 10.1038/nature13785.
- F. Fressin, G. Torres, D. Charbonneau, S. T. Bryson, J. Christiansen, C. D. Dressing, J. M. Jenkins, L. M. Walkowicz, and N. M. Batalha. The False Positive Rate of Kepler and the Occurrence of Planets. *ApJ*, 766:81, April 2013. doi: 10.1088/0004-637X/766/2/81.
- B. J. Fulton, E. A. Petigura, A. W. Howard, H. Isaacson, G. W. Marcy, P. A. Cargile, L. Hebb, L. M. Weiss, J. A. Johnson, T. D. Morton, E. Sinukoff, I. J. M. Crossfield, and L. A. Hirsch. The California-Kepler Survey. III. A Gap in the Radius Distribution of Small Planets. *ArXiv e-prints*, March 2017.
- N. P. Gibson, F. Pont, and S. Aigrain. A new look at NICMOS transmission spectroscopy of HD 189733, GJ-436 and XO-1: no conclusive evidence for molecular features. *MNRAS*, 411:2199–2213, March 2011. doi: 10.1111/j.1365-2966.2010.17837.x.
- N. P. Gibson, S. Aigrain, S. Roberts, T. M. Evans, M. Osborne, and F. Pont. A Gaussian process framework for modelling instrumental systematics: application to transmission spectroscopy. *MNRAS*, 419:2683–2694, January 2012. doi: 10.1111/j.1365-2966.2011.19915.x.
- M. Gillon, B.-O. Demory, T. Barman, X. Bonfils, T. Mazeh, F. Pont, S. Udry, M. Mayor, and D. Queloz. Accurate Spitzer infrared radius measurement for the hot Neptune GJ 436b. *A&A*, 471:L51–L54, September 2007. doi: 10.1051/0004-6361:20078283.
- M. Gillon, B. Smalley, L. Hebb, D. R. Anderson, A. H. M. J. TriAUD, C. Hellier, P. F. L. Maxted, D. Queloz, and D. M. Wilson. Improved parameters for the transiting hot Jupiters WASP-4b and WASP-5b. *A&A*, 496:259–267, March 2009. doi: 10.1051/0004-6361:200810929.
- M. Gillon, A. A. Lanotte, T. Barman, N. Miller, B.-O. Demory, M. Deleuil, J. Montalbán, F. Bouchy, A. Collier Cameron, H. J. Deeg, J. J. Fortney, M. Fridlund, J. Harrington, P. Magain, C. Moutou, D. Queloz, H. Rauer, D. Rouan, and J. Schneider. The thermal emission of the young and massive planet CoRoT-2b at 4.5 and 8 μm . *A&A*, 511:A3, February 2010. doi: 10.1051/0004-6361/200913507.
- M. Gillon, E. Jehin, P. Magain, V. Chantry, D. Hutsemékers, J. Manfroid, D. Queloz, and S. Udry. TRAPPIST: a robotic telescope dedicated to the study of planetary systems. In *European Physical Journal Web of Conferences*, volume 11 of *European Physical Journal Web of Conferences*, page 06002, February 2011. doi: 10.1051/epjconf/20101106002.

- M. Gillon, A. H. M. J. Triaud, J. J. Fortney, B.-O. Demory, E. Jehin, M. Lendl, P. Magain, P. Kabath, D. Queloz, R. Alonso, D. R. Anderson, A. Collier Cameron, A. Fumel, L. Hebb, C. Hellier, A. Lanotte, P. F. L. Maxted, N. Mowlavi, and B. Smalley. The TRAPPIST survey of southern transiting planets. I. Thirty eclipses of the ultra-short period planet WASP-43 b. *A&A*, 542:A4, June 2012. doi: 10.1051/0004-6361/201218817.
- M. Gillon, E. Jehin, L. Delrez, P. Magain, C. Opitom, and S. Sohy. SPECULOOS: Search for habitable Planets EClipsing ULtra-cOOl Stars. In *Protostars and Planets VI Posters*, July 2013.
- P. Goldreich. On the eccentricity of satellite orbits in the solar system. *MNRAS*, 126:257, 1963. doi: 10.1093/mnras/126.3.257.
- P. Goldreich and P. D. Nicholson. Turbulent viscosity and Jupiter’s tidal Q. *Icarus*, 30:301–304, February 1977. doi: 10.1016/0019-1035(77)90163-4.
- P. Goldreich and S. Soter. Q in the Solar System. *Icarus*, 5:375–389, 1966. doi: 10.1016/0019-1035(66)90051-0.
- J. Goodman and E. S. Dickson. Dynamical Tide in Solar-Type Binaries. *ApJ*, 507: 938–944, November 1998. doi: 10.1086/306348.
- C. J. Grillmair, D. Charbonneau, A. Burrows, L. Armus, J. Stauffer, V. Meadows, J. Van Cleve, and D. Levine. A Spitzer Spectrum of the Exoplanet HD 189733b. *ApJL*, 658:L115–L118, April 2007. doi: 10.1086/513741.
- T. Guillot and M. Havel. An analysis of the CoRoT-2 system: a young spotted star and its inflated giant planet. *A&A*, 527:A20, March 2011. doi: 10.1051/0004-6361/201015051.
- T. Guillot, A. Burrows, W. B. Hubbard, J. I. Lunine, and D. Saumon. Giant Planets at Small Orbital Distances. *ApJL*, 459:L35, March 1996. doi: 10.1086/309935.
- Douglas P. Hamilton. Extrasolar planets: Secrets that only tides will tell. *Nature*, 460(7259):1086–1087, 08 2009. URL <http://dx.doi.org/10.1038/4601086a>.
- J. D. Hartman, G. Á. Bakos, D. M. Kipping, G. Torres, G. Kovács, R. W. Noyes, D. W. Latham, A. W. Howard, D. A. Fischer, J. A. Johnson, G. W. Marcy, H. Isaacson, S. N. Quinn, L. A. Buchhave, B. Béky, D. D. Sasselov, R. P. Stefanik, G. A. Esquerdo, M. Everett, G. Perumpilly, J. Lázár, I. Papp, and P. Sári. HAT-P-26b: A Low-density Neptune-mass Planet Transiting a K Star. *ApJ*, 728:138, February 2011. doi: 10.1088/0004-637X/728/2/138.
- C. Hellier, D. R. Anderson, A. Collier Cameron, M. Gillon, L. Hebb, P. F. L. Maxted, D. Queloz, B. Smalley, A. H. M. J. Triaud, R. G. West, D. M. Wilson, S. J. Bentley, B. Enoch, K. Horne, J. Irwin, T. A. Lister, M. Mayor, N. Parley, F. Pepe, D. L. Pollacco, D. Segransan, S. Udry, and P. J. Wheatley. An orbital

- period of 0.94days for the hot-Jupiter planet WASP-18b. *Nature*, 460:1098–1100, August 2009. doi: 10.1038/nature08245.
- C. Hellier, D. R. Anderson, A. Collier Cameron, L. Delrez, M. Gillon, E. Jehin, M. Lendl, P. F. L. Maxted, M. Neveu-VanMalle, F. Pepe, D. Pollacco, D. Queloz, D. Ségransan, B. Smalley, J. Southworth, A. H. M. J. Triaud, S. Udry, T. Wagg, and R. G. West. Wasp-south transiting exoplanets: Wasp-130b, wasp-131b, wasp-132b, wasp-139b, wasp-140b, wasp-141b and wasp-142b. *Monthly Notices of the Royal Astronomical Society*, 465(3):3693–3707, 2017. doi: 10.1093/mnras/stw3005. URL [+http://dx.doi.org/10.1093/mnras/stw3005](http://dx.doi.org/10.1093/mnras/stw3005).
- K. Heng. *Exoplanetary Atmospheres: Theoretical Concepts and Foundations*. Princeton University Press, 2017.
- K. Heng and M. Marley. Radiative Transfer for Exoplanet Atmospheres. *ArXiv e-prints*, June 2017.
- S. B. Howell, C. Sobeck, M. Haas, M. Still, T. Barclay, F. Mullally, J. Troeltzsch, S. Aigrain, S. T. Bryson, D. Caldwell, W. J. Chaplin, W. D. Cochran, D. Huber, G. W. Marcy, A. Miglio, J. R. Najita, M. Smith, J. D. Twicken, and J. J. Fortney. The K2 Mission: Characterization and Early Results. *PASP*, 126:398, April 2014. doi: 10.1086/676406.
- S. Hoyer, E. Pallé, D. Dragomir, and F. Murgas. Ruling out the Orbital Decay of the WASP-43b Exoplanet. *AJ*, 151:137, June 2016. doi: 10.3847/0004-6256/151/6/137.
- R. Hu and S. Seager. Photochemistry in Terrestrial Exoplanet Atmospheres. III. Photochemistry and Thermochemistry in Thick Atmospheres on Super Earths and Mini Neptunes. *ApJ*, 784:63, March 2014. doi: 10.1088/0004-637X/784/1/63.
- I. Hubeny, A. Burrows, and D. Sudarsky. A Possible Bifurcation in Atmospheres of Strongly Irradiated Stars and Planets. *ApJ*, 594:1011–1018, September 2003. doi: 10.1086/377080.
- C. M. Huitson, D. K. Sing, F. Pont, J. J. Fortney, A. S. Burrows, P. A. Wilson, G. E. Ballester, N. Nikolov, N. P. Gibson, D. Deming, S. Aigrain, T. M. Evans, G. W. Henry, A. Lecavelier des Etangs, A. P. Showman, A. Vidal-Madjar, and K. Zahnle. An HST optical-to-near-IR transmission spectrum of the hot Jupiter WASP-19b: detection of atmospheric water and likely absence of TiO. *MNRAS*, 434:3252–3274, October 2013. doi: 10.1093/mnras/stt1243.
- C. M. Huitson, J.-M. Désert, J. L. Bean, J. J. Fortney, K. B. Stevenson, and M. Bergmann. Gemini/GMOS Transmission Spectral Survey: Complete Optical Transmission Spectrum of the Hot Jupiter WASP-4b. *AJ*, 154:95, September 2017. doi: 10.3847/1538-3881/aa7f72.

- B. Jackson, R. Barnes, and R. Greenberg. Observational Evidence for Tidal Destruction of Exoplanets. *ApJ*, 698:1357–1366, June 2009. doi: 10.1088/0004-637X/698/2/1357.
- H. Jang-Condell. Observable Differences Between Core Accretion and Disk Instability. In K. J. Meech, J. V. Keane, M. J. Mumma, J. L. Siefert, and D. J. Werthimer, editors, *Bioastronomy 2007: Molecules, Microbes and Extraterrestrial Life*, volume 420 of *Astronomical Society of the Pacific Conference Series*, page 305, December 2009.
- E. Jehin, M. Gillon, D. Queloz, P. Magain, J. Manfroid, V. Chantry, M. Lendl, D. Hutsemékers, and S. Udry. TRAPPIST: TRAnsiting Planets and Planetesimals Small Telescope. *The Messenger*, 145:2–6, September 2011.
- I.-G. Jiang, C.-Y. Lai, A. Savushkin, D. Mkrtychian, K. Antonyuk, E. Griv, H.-F. Hsieh, and L.-C. Yeh. The Possible Orbital Decay and Transit Timing Variations of the Planet WASP-43b. *AJ*, 151:17, January 2016. doi: 10.3847/0004-6256/151/1/17.
- C. Jurgenson, D. Fischer, T. McCracken, D. Sawyer, A. Szymkowiak, A. Davis, G. Muller, and F. Santoro. EXPRES: a next generation RV spectrograph in the search for earth-like worlds. In *Ground-based and Airborne Instrumentation for Astronomy VI*, volume 9908 of *Proc. SPIE*, page 99086T, August 2016. doi: 10.1117/12.2233002.
- E. M.-R. Kempton, R. Lupu, A. Owusu-Asare, P. Slough, and B. Cale. Exo-Transmit: An Open-Source Code for Calculating Transmission Spectra for Exoplanet Atmospheres of Varied Composition. *PASP*, 129(4):044402, April 2017. doi: 10.1088/1538-3873/aa61ef.
- W. Kley and R. P. Nelson. Planet-Disk Interaction and Orbital Evolution. *ARA&A*, 50:211–249, September 2012. doi: 10.1146/annurev-astro-081811-125523.
- H. A. Knutson, D. Charbonneau, L. E. Allen, J. J. Fortney, E. Agol, N. B. Cowan, A. P. Showman, C. S. Cooper, and S. T. Megeath. A map of the day-night contrast of the extrasolar planet HD 189733b. *Nature*, 447:183–186, May 2007. doi: 10.1038/nature05782.
- H. A. Knutson, D. Charbonneau, L. E. Allen, A. Burrows, and S. T. Megeath. The 3.6-8.0 μm Broadband Emission Spectrum of HD 209458b: Evidence for an Atmospheric Temperature Inversion. *ApJ*, 673:526-531, January 2008. doi: 10.1086/523894.
- H. A. Knutson, A. W. Howard, and H. Isaacson. A Correlation Between Stellar Activity and Hot Jupiter Emission Spectra. *ApJ*, 720:1569–1576, September 2010. doi: 10.1088/0004-637X/720/2/1569.

- H. A. Knutson, B. Benneke, D. Deming, and D. Homeier. A featureless transmission spectrum for the Neptune-mass exoplanet GJ436b. *Nature*, 505:66–68, January 2014a. doi: 10.1038/nature12887.
- H. A. Knutson, D. Dragomir, L. Kreidberg, E. M.-R. Kempton, P. R. McCullough, J. J. Fortney, J. L. Bean, M. Gillon, D. Homeier, and A. W. Howard. Hubble Space Telescope Near-IR Transmission Spectroscopy of the Super-Earth HD 97658b. *ApJ*, 794:155, October 2014b. doi: 10.1088/0004-637X/794/2/155.
- L. Kreidberg. batman: BAseic Transit Model cAlculation in Python. *PASP*, 127: 1161–1165, November 2015. doi: 10.1086/683602.
- L. Kreidberg, J. L. Bean, J.-M. Désert, B. Benneke, D. Deming, K. B. Stevenson, S. Seager, Z. Berta-Thompson, A. Seifahrt, and D. Homeier. Clouds in the atmosphere of the super-Earth exoplanet GJ1214b. *Nature*, 505:69–72, January 2014. doi: 10.1038/nature12888.
- Walsh-J. R. Kuntzschner H. & Bushouse H. Kümmel, M. *aXe User Manual*. STScI, 2.3 edition, June 2011.
- H. Kuntzschner, H. Bushouse, M. Kümmel, and J. R. Walsh. WFC3 SMOV proposal 11552: Calibration of the G141 grism. Technical report, STScI, October 2009.
- A. F. Lanza, I. Pagano, G. Leto, S. Messina, S. Aigrain, R. Alonso, M. Auvergne, A. Baglin, P. Barge, A. S. Bonomo, P. Boumier, A. Collier Cameron, M. Comparato, G. Cutispoto, J. R. de Medeiros, B. Foing, A. Kaiser, C. Moutou, P. S. Parihar, A. Silva-Valio, and W. W. Weiss. Magnetic activity in the photosphere of CoRoT-Exo-2a. Active longitudes and short-term spot cycle in a young Sun-like star. *A&A*, 493:193–200, January 2009. doi: 10.1051/0004-6361:200810591.
- A. F. Lanza, C. Damiani, and D. Gandolfi. Constraining tidal dissipation in F-type main-sequence stars: the case of CoRoT-11. *A&A*, 529:A50, May 2011. doi: 10.1051/0004-6361/201016144.
- H. F. Levison, A. Morbidelli, K. Tsiganis, D. Nesvorný, and R. Gomes. Late Orbital Instabilities in the Outer Planets Induced by Interaction with a Self-gravitating Planetesimal Disk. *AJ*, 142:152, November 2011. doi: 10.1088/0004-6256/142/5/152.
- D. N. C. Lin, P. Bodenheimer, and D. C. Richardson. Orbital migration of the planetary companion of 51 Pegasi to its present location. *Nature*, 380:606–607, April 1996. doi: 10.1038/380606a0.
- M. R. Line and V. Parmentier. The Influence of Nonuniform Cloud Cover on Transit Transmission Spectra. *ApJ*, 820:78, March 2016. doi: 10.3847/0004-637X/820/1/78.

- M. R. Line, H. Knutson, D. Deming, A. Wilkins, and J.-M. Desert. A Near-infrared Transmission Spectrum for the Warm Saturn HAT-P-12b. *ApJ*, 778:183, December 2013a. doi: 10.1088/0004-637X/778/2/183.
- M. R. Line, A. S. Wolf, X. Zhang, H. Knutson, J. A. Kammer, E. Ellison, P. Deroo, D. Crisp, and Y. L. Yung. A Systematic Retrieval Analysis of Secondary Eclipse Spectra. I. A Comparison of Atmospheric Retrieval Techniques. *ApJ*, 775:137, October 2013b. doi: 10.1088/0004-637X/775/2/137.
- M. R. Line, K. B. Stevenson, J. Bean, J.-M. Desert, J. J. Fortney, L. Kreidberg, N. Madhusudhan, A. P. Showman, and H. Diamond-Lowe. No Thermal Inversion and a Solar Water Abundance for the Hot Jupiter HD 209458b from HST/WFC3 Spectroscopy. *AJ*, 152:203, December 2016. doi: 10.3847/0004-6256/152/6/203.
- E. D. Lopez and J. J. Fortney. The Role of Core Mass in Controlling Evaporation: The Kepler Radius Distribution and the Kepler-36 Density Dichotomy. *ApJ*, 776:2, October 2013. doi: 10.1088/0004-637X/776/1/2.
- S. H. Lubow and S. Ida. *Planet Migration*, pages 347–371. University of Arizona Press, December 2010.
- G. Maciejewski, D. Dimitrov, M. Fernández, A. Sota, G. Nowak, J. Ohlert, G. Nikolov, Ł. Bukowiecki, T. C. Hinse, E. Pallé, B. Tingley, D. Kjurkchieva, J. W. Lee, and C.-U. Lee. Departure from the constant-period ephemeris for the transiting exoplanet WASP-12. *A&A*, 588:L6, April 2016. doi: 10.1051/0004-6361/201628312.
- B. Macintosh, J. R. Graham, P. Ingraham, Q. Konopacky, C. Marois, M. Perrin, L. Poyneer, B. Bauman, T. Barman, A. S. Burrows, A. Cardwell, J. Chilcote, R. J. De Rosa, D. Dillon, R. Doyon, J. Dunn, D. Erikson, M. P. Fitzgerald, D. Gavel, S. Goodsell, M. Hartung, P. Higon, P. Kalas, J. Larkin, J. Maire, F. Marchis, M. S. Marley, J. McBride, M. Millar-Blanchaer, K. Morzinski, A. Norton, B. R. Oppenheimer, D. Palmer, J. Patience, L. Pueyo, F. Rantakyro, N. Sadakuni, L. Saddlemyer, D. Savransky, A. Serio, R. Soummer, A. Sivaramakrishnan, I. Song, S. Thomas, J. K. Wallace, S. Wiktorowicz, and S. Wolff. First light of the Gemini Planet Imager. *Proceedings of the National Academy of Science*, 111:12661–12666, September 2014. doi: 10.1073/pnas.1304215111.
- N. Madhusudhan. C/O Ratio as a Dimension for Characterizing Exoplanetary Atmospheres. *ApJ*, 758:36, October 2012. doi: 10.1088/0004-637X/758/1/36.
- N. Madhusudhan and S. Seager. A Temperature and Abundance Retrieval Method for Exoplanet Atmospheres. *ApJ*, 707:24–39, December 2009. doi: 10.1088/0004-637X/707/1/24.
- N. Madhusudhan and S. Seager. On the Inference of Thermal Inversions in Hot Jupiter Atmospheres. *ApJ*, 725:261–274, December 2010. doi: 10.1088/0004-637X/725/1/261.

- N. Madhusudhan, M. A. Amin, and G. M. Kennedy. Toward Chemical Constraints on Hot Jupiter Migration. *ApJL*, 794:L12, October 2014. doi: 10.1088/2041-8205/794/1/L12.
- N. Madhusudhan, M. Agúndez, J. I. Moses, and Y. Hu. Exoplanetary Atmospheres—Chemistry, Formation Conditions, and Habitability. *SSRv*, May 2016. doi: 10.1007/s11214-016-0254-3.
- C. Majeau, E. Agol, and N. B. Cowan. A Two-dimensional Infrared Map of the Extrasolar Planet HD 189733b. *ApJL*, 747:L20, March 2012. doi: 10.1088/2041-8205/747/2/L20.
- K. Mandel and E. Agol. Analytic Light Curves for Planetary Transit Searches. *ApJL*, 580:L171–L175, December 2002. doi: 10.1086/345520.
- A. M. Mandell, K. Haynes, E. Sinukoff, N. Madhusudhan, A. Burrows, and D. Deming. Exoplanet Transit Spectroscopy Using WFC3: WASP-12 b, WASP-17 b, and WASP-19 b. *ApJ*, 779:128, December 2013. doi: 10.1088/0004-637X/779/2/128.
- M. S. Marley, A. S. Ackerman, J. N. Cuzzi, and D. Kitzmann. *Clouds and Hazes in Exoplanet Atmospheres*, pages 367–391. University of Arizona Press, 2013. doi: 10.2458/azu_uapress.9780816530595-ch15.
- C. Marois, B. Macintosh, T. Barman, B. Zuckerman, I. Song, J. Patience, D. Lafrenière, and R. Doyon. Direct Imaging of Multiple Planets Orbiting the Star HR 8799. *Science*, 322:1348, November 2008. doi: 10.1126/science.1166585.
- P. F. L. Maxted, D. R. Anderson, A. P. Doyle, M. Gillon, J. Harrington, N. Iro, E. Jehin, D. Lafrenière, B. Smalley, and J. Southworth. Spitzer 3.6 and 4.5 μm full-orbit light curves of WASP-18. *MNRAS*, 428:2645–2660, January 2013. doi: 10.1093/mnras/sts231.
- M. Mayor and D. Queloz. A Jupiter-mass companion to a solar-type star. *Nature*, 378:355–359, November 1995. doi: 10.1038/378355a0.
- R. Mbarek and E. M.-R. Kempton. Clouds in Super-Earth Atmospheres: Chemical Equilibrium Calculations. *ApJ*, 827:121, August 2016. doi: 10.3847/0004-637X/827/2/121.
- P. McCullough and J. MacKenty. Considerations for using Spatial Scans with WFC3. Technical report, STScI, May 2012.
- C. F. McKee and E. C. Ostriker. Theory of Star Formation. *ARA&A*, 45:565–687, September 2007. doi: 10.1146/annurev.astro.45.051806.110602.
- S. Meibom and R. D. Mathieu. A Robust Measure of Tidal Circularization in Coeval Binary Populations: The Solar-Type Spectroscopic Binary Population in the Open Cluster M35. *ApJ*, 620:970–983, February 2005. doi: 10.1086/427082.

- M. C. Miller and D. P. Hamilton. Implications of the PSR 1257+12 Planetary System for Isolated Millisecond Pulsars. *ApJ*, 550:863–870, April 2001. doi: 10.1086/319813.
- N. Miller and J. J. Fortney. The Heavy-element Masses of Extrasolar Giant Planets, Revealed. *ApJL*, 736:L29, August 2011. doi: 10.1088/2041-8205/736/2/L29.
- E. Miller-Ricci and J. J. Fortney. The Nature of the Atmosphere of the Transiting Super-Earth GJ 1214b. *ApJL*, 716:L74–L79, June 2010. doi: 10.1088/2041-8205/716/1/L74.
- S. Nymeyer, J. Harrington, R. A. Hardy, K. B. Stevenson, C. J. Campo, N. Madhusudhan, A. Collier-Cameron, T. J. Loredó, J. Blečić, W. C. Bowman, C. B. T. Britt, P. Cubillos, C. Hellier, M. Gillon, P. F. L. Maxted, L. Hebb, P. J. Wheatley, D. Pollacco, and D. R. Anderson. Spitzer Secondary Eclipses of WASP-18b. *ApJ*, 742:35, November 2011. doi: 10.1088/0004-637X/742/1/35.
- K. I. Öberg, R. Murray-Clay, and E. A. Bergin. The Effects of Snowlines on C/O in Planetary Atmospheres. *ApJL*, 743:L16, December 2011. doi: 10.1088/2041-8205/743/1/L16.
- T. E. Oberst, J. E. Rodríguez, K. D. Colón, D. Angerhausen, A. Bieryla, H. Ngo, D. J. Stevens, K. G. Stassun, B. S. Gaudi, J. Pepper, K. Penev, D. Mawet, D. W. Latham, T. M. Heintz, B. W. Osei, K. A. Collins, J. F. Kielkopf, T. Visgaitis, P. A. Reed, A. Escamilla, S. Yazdi, K. K. McLeod, L. T. Lunsford, M. Spencer, M. D. Joner, J. Gregorio, C. Gaillard, K. Matt, M. T. Dumont, D. C. Stephens, D. H. Cohen, E. L. N. Jensen, S. Calchi Novati, V. Bozza, J. Labadie-Bartz, R. J. Siverd, M. B. Lund, T. G. Beatty, J. D. Eastman, M. T. Penny, M. Manner, R. Zambelli, B. J. Fulton, D. L. DePoy, J. L. Marshall, R. W. Pogge, A. Gould, M. Trueblood, and P. Trueblood. KELT-16b: A highly irradiated, ultra-short period hot Jupiter nearing tidal disruption. *ArXiv e-prints*, August 2016.
- G. I. Ogilvie. Tidal Dissipation in Stars and Giant Planets. *ARA&A*, 52:171–210, August 2014. doi: 10.1146/annurev-astro-081913-035941.
- G. I. Ogilvie and G. Lesur. On the interaction between tides and convection. *MNRAS*, 422:1975–1987, May 2012. doi: 10.1111/j.1365-2966.2012.20630.x.
- G. I. Ogilvie and D. N. C. Lin. Tidal Dissipation in Rotating Solar-Type Stars. *ApJ*, 661:1180–1191, June 2007. doi: 10.1086/515435.
- J. E. Owen and Y. Wu. Kepler Planets: A Tale of Evaporation. *ApJ*, 775:105, October 2013. doi: 10.1088/0004-637X/775/2/105.
- J. E. Owen and Y. Wu. The evaporation valley in the Kepler planets. *ArXiv e-prints*, May 2017.

- B. Paxton, L. Bildsten, A. Dotter, F. Herwig, P. Lesaffre, and F. Timmes. Modules for Experiments in Stellar Astrophysics (MESA). *ApJS*, 192:3, January 2011. doi: 10.1088/0067-0049/192/1/3.
- K. Penev and D. Sasselov. Tidal Evolution of Close-in Extrasolar Planets: High Stellar Q from New Theoretical Models. *ApJ*, 731:67, April 2011. doi: 10.1088/0004-637X/731/1/67.
- J. Pepper, R. W. Pogge, D. L. DePoy, J. L. Marshall, K. Z. Stanek, A. M. Stutz, S. Poindexter, R. Siverd, T. P. O'Brien, M. Trueblood, and P. Trueblood. The Kilodegree Extremely Little Telescope (KELT): A Small Robotic Telescope for Large-Area Synoptic Surveys. *PASP*, 119:923–935, August 2007. doi: 10.1086/521836.
- J. Pepper, R. B. Kuhn, R. Siverd, D. James, and K. Stassun. The KELT-South Telescope. *PASP*, 124:230, March 2012. doi: 10.1086/665044.
- E. A. Petigura, E. Sinukoff, E. D. Lopez, I. J. M. Crossfield, A. W. Howard, J. M. Brewer, B. J. Fulton, H. T. Isaacson, D. R. Ciardi, S. B. Howell, M. E. Everett, E. P. Horch, L. A. Hirsch, L. M. Weiss, and J. E. Schlieder. Four Sub-Saturns with Dissimilar Densities: Windows into Planetary Cores and Envelopes. *AJ*, 153:142, April 2017. doi: 10.3847/1538-3881/aa5ea5.
- N. Pirzkal, R. Ryan, and G. Brammer. Trace and Wavelength Calibrations of the WFC3 G102 and G141 IR Grisms. Technical report, STScI, September 2016.
- D. L. Pollacco, I. Skillen, A. Collier Cameron, D. J. Christian, C. Hellier, J. Irwin, T. A. Lister, R. A. Street, R. G. West, D. R. Anderson, W. I. Clarkson, H. Deeg, B. Enoch, A. Evans, A. Fitzsimmons, C. A. Haswell, S. Hodgkin, K. Horne, S. R. Kane, F. P. Keenan, P. F. L. Maxted, A. J. Norton, J. Osborne, N. R. Parley, R. S. I. Ryans, B. Smalley, P. J. Wheatley, and D. M. Wilson. The WASP Project and the SuperWASP Cameras. *PASP*, 118:1407–1418, October 2006. doi: 10.1086/508556.
- J. B. Pollack, O. Hubickyj, P. Bodenheimer, J. J. Lissauer, M. Podolak, and Y. Greenzweig. Formation of the Giant Planets by Concurrent Accretion of Solids and Gas. *Icarus*, 124:62–85, November 1996. doi: 10.1006/icar.1996.0190.
- F. Pont, D. K. Sing, N. P. Gibson, S. Aigrain, G. Henry, and N. Husnoo. The prevalence of dust on the exoplanet HD 189733b from Hubble and Spitzer observations. *MNRAS*, 432:2917–2944, July 2013. doi: 10.1093/mnras/stt651.
- K. M. Pontoppidan. Spatial mapping of ices in the Ophiuchus-F core. A direct measurement of CO depletion and the formation of CO₂. *A&A*, 453:L47–L50, July 2006. doi: 10.1051/0004-6361:20065569.
- A. Rajan and et al. *WFC3 Data Handbook v. 2.1*. STScI, May 2011.

- S. Ranjan, D. Charbonneau, J.-M. Désert, N. Madhusudhan, D. Deming, A. Wilkins, and A. M. Mandell. Atmospheric Characterization of Five Hot Jupiters with the Wide Field Camera 3 on the Hubble Space Telescope. *ApJ*, 785:148, April 2014. doi: 10.1088/0004-637X/785/2/148.
- S. Redfield, M. Endl, W. D. Cochran, and L. Koesterke. Sodium Absorption from the Exoplanetary Atmosphere of HD 189733b Detected in the Optical Transmission Spectrum. *ApJL*, 673:L87, January 2008. doi: 10.1086/527475.
- C. Richard, I. E. Gordon, L. S. Rothman, M. Abel, L. Frommhold, M. Gustafsson, J.-M. Hartmann, C. Hermans, W. J. Lafferty, G. S. Orton, K. M. Smith, and H. Tran. New section of the HITRAN database: Collision-induced absorption (CIA). *JQSRT*, 113:1276–1285, July 2012. doi: 10.1016/j.jqsrt.2011.11.004.
- L. J. Richardson, D. Deming, K. Horning, S. Seager, and J. Harrington. A spectrum of an extrasolar planet. *Nature*, 445:892–895, February 2007. doi: 10.1038/nature05636.
- G. R. Ricker, J. N. Winn, R. Vanderspek, D. W. Latham, G. Á. Bakos, J. L. Bean, Z. K. Berta-Thompson, T. M. Brown, L. Buchhave, N. R. Butler, R. P. Butler, W. J. Chaplin, D. Charbonneau, J. Christensen-Dalsgaard, M. Clampin, D. Deming, J. Doty, N. De Lee, C. Dressing, E. W. Dunham, M. Endl, F. Fressin, J. Ge, T. Henning, M. J. Holman, A. W. Howard, S. Ida, J. Jenkins, G. Jernigan, J. A. Johnson, L. Kaltenegger, N. Kawai, H. Kjeldsen, G. Laughlin, A. M. Levine, D. Lin, J. J. Lissauer, P. MacQueen, G. Marcy, P. R. McCullough, T. D. Morton, N. Narita, M. Paegert, E. Palle, F. Pepe, J. Pepper, A. Quirrenbach, S. A. Rinehart, D. Sasselov, B. Sato, S. Seager, A. Sozzetti, K. G. Stassun, P. Sullivan, A. Szentgyorgyi, G. Torres, S. Udry, and J. Villaseñor. Transiting Exoplanet Survey Satellite (TESS). In *Space Telescopes and Instrumentation 2014: Optical, Infrared, and Millimeter Wave*, volume 9143 of *Proc. SPIE*, page 914320, August 2014. doi: 10.1117/12.2063489.
- J. F. Rowe, J. M. Matthews, S. Seager, E. Miller-Ricci, D. Sasselov, R. Kuschnig, D. B. Guenther, A. F. J. Moffat, S. M. Rucinski, G. A. H. Walker, and W. W. Weiss. The Very Low Albedo of an Extrasolar Planet: MOST Space-based Photometry of HD 209458. *ApJ*, 689:1345–1353, December 2008. doi: 10.1086/591835.
- P. V. Sada, D. Deming, D. E. Jennings, B. k. Jackson, C. M. Hamilton, J. Fraine, S. W. Peterson, F. Haase, K. Bays, A. Lunsford, and E. O’Gorman. Extrasolar Planet Transits Observed at Kitt Peak National Observatory. *PASP*, 124:212, March 2012. doi: 10.1086/665043.
- S. Schröter, S. Czesla, U. Wolter, H. M. Müller, K. F. Huber, and J. H. M. M. Schmitt. The corona and companion of CoRoT-2a. Insights from X-rays and optical spectroscopy. *A&A*, 532:A3, August 2011. doi: 10.1051/0004-6361/201116961.
- S. Seager. *Exoplanet Atmospheres: Physical Processes*. Princeton University Press, 2010.

- S. Seager and D. D. Sasselov. Theoretical Transmission Spectra during Extrasolar Giant Planet Transits. *ApJ*, 537:916–921, July 2000. doi: 10.1086/309088.
- S. Seager, D. Deming, and J. A. Valenti. Transiting Exoplanets with JWST. *Astrophysics and Space Science Proceedings*, 10:123, 2009. doi: 10.1007/978-1-4020-9457-6_5.
- Marie Šimečková, David Jacquemart, Laurence S. Rothman, Robert R. Gamache, and Aaron Goldman. Einstein a -coefficients and statistical weights for molecular absorption transitions in the hitran database. *Journal of Quantitative Spectroscopy and Radiative Transfer*, 98(1):130 – 155, 2006. ISSN 0022-4073. doi: <http://dx.doi.org/10.1016/j.jqsrt.2005.07.003>. URL <http://www.sciencedirect.com/science/article/pii/S0022407305002931>.
- D. K. Sing, F. Pont, S. Aigrain, D. Charbonneau, J.-M. Désert, N. Gibson, R. Gilliland, W. Hayek, G. Henry, H. Knutson, A. Lecavelier Des Etangs, T. Mazeh, and A. Shporer. Hubble Space Telescope transmission spectroscopy of the exoplanet HD 189733b: high-altitude atmospheric haze in the optical and near-ultraviolet with STIS. *MNRAS*, 416:1443–1455, September 2011. doi: 10.1111/j.1365-2966.2011.19142.x.
- D. K. Sing, J. J. Fortney, N. Nikolov, H. R. Wakeford, T. Kataria, T. M. Evans, S. Aigrain, G. E. Ballester, A. S. Burrows, D. Deming, J.-M. Désert, N. P. Gibson, G. W. Henry, C. M. Huitson, H. A. Knutson, A. L. D. Etangs, F. Pont, A. P. Showman, A. Vidal-Madjar, M. H. Williamson, and P. A. Wilson. A continuum from clear to cloudy hot-Jupiter exoplanets without primordial water depletion. *Nature*, 529:59–62, January 2016. doi: 10.1038/nature16068.
- R. M. Smith, M. Zavodny, G. Rahmer, and M. Bonati. A theory for image persistence in HgCdTe photodiodes. In *High Energy, Optical, and Infrared Detectors for Astronomy III*, volume 7021 of *Proc. SPIE*, page 70210J, July 2008. doi: 10.1117/12.789372.
- I. A. G. Snellen, S. Albrecht, E. J. W. de Mooij, and R. S. Le Poole. Ground-based detection of sodium in the transmission spectrum of exoplanet HD 209458b. *A&A*, 487:357–362, August 2008. doi: 10.1051/0004-6361:200809762.
- I. A. G. Snellen, R. J. de Kok, E. J. W. de Mooij, and S. Albrecht. The orbital motion, absolute mass and high-altitude winds of exoplanet HD209458b. *Nature*, 465:1049–1051, June 2010a. doi: 10.1038/nature09111.
- I. A. G. Snellen, E. J. W. de Mooij, and A. Burrows. Bright optical day-side emission from extrasolar planet CoRoT-2b. *A&A*, 513:A76, April 2010b. doi: 10.1051/0004-6361/200913338.
- J. Southworth. Homogeneous studies of transiting extrasolar planets - I. Light-curve analyses. *MNRAS*, 386:1644–1666, May 2008. doi: 10.1111/j.1365-2966.2008.13145.x.

- J. Southworth, T. C. Hinse, M. Dominik, M. Glittrup, U. G. Jørgensen, C. Liebig, M. Mathiasen, D. R. Anderson, V. Bozza, P. Browne, M. Burgdorf, S. Calchi Novati, S. Dreizler, F. Finet, K. Harpsøe, F. Hessman, M. Hundertmark, G. Maier, L. Mancini, P. F. L. Maxted, S. Rahvar, D. Ricci, G. Scarpetta, J. Skottfelt, C. Snodgrass, J. Surdej, and F. Zimmer. Physical Properties of the 0.94-Day Period Transiting Planetary System WASP-18. *ApJ*, 707:167, December 2009. doi: 10.1088/0004-637X/707/1/167.
- J. Southworth, T. C. Hinse, M. Dominik, M. Glittrup, U. G. Jørgensen, C. Liebig, M. Mathiasen, D. R. Anderson, V. Bozza, P. Browne, M. Burgdorf, S. Calchi Novati, S. Dreizler, F. Finet, K. Harpsøe, F. Hessman, M. Hundertmark, G. Maier, L. Mancini, P. F. L. Maxted, S. Rahvar, D. Ricci, G. Scarpetta, J. Skottfelt, C. Snodgrass, J. Surdej, and F. Zimmer. ERRATUM: "Physical Properties of the 0.94 Day Period Transiting Planetary System WASP-18" [\[A href="/abs/2009ApJ...707..167S" \(2009, ApJ, 707, 167\)\]/A](#). *ApJ*, 723:1829, November 2010. doi: 10.1088/0004-637X/723/2/1829.
- K. B. Stevenson, J. Harrington, S. Nymeyer, N. Madhusudhan, S. Seager, W. C. Bowman, R. A. Hardy, D. Deming, E. Rauscher, and N. B. Lust. Possible thermochemical disequilibrium in the atmosphere of the exoplanet GJ 436b. *Nature*, 464:1161–1164, April 2010. doi: 10.1038/nature09013.
- K. B. Stevenson, J.-M. Désert, M. R. Line, J. L. Bean, J. J. Fortney, A. P. Showman, T. Kataria, L. Kreidberg, P. R. McCullough, G. W. Henry, D. Charbonneau, A. Burrows, S. Seager, N. Madhusudhan, M. H. Williamson, and D. Homeier. Thermal structure of an exoplanet atmosphere from phase-resolved emission spectroscopy. *Science*, 346:838–841, November 2014. doi: 10.1126/science.1256758.
- P. W. Sullivan, J. N. Winn, Z. K. Berta-Thompson, D. Charbonneau, D. Deming, C. D. Dressing, D. W. Latham, A. M. Levine, P. R. McCullough, T. Morton, G. R. Ricker, R. Vanderspek, and D. Woods. The Transiting Exoplanet Survey Satellite: Simulations of Planet Detections and Astrophysical False Positives. *ApJ*, 809:77, August 2015. doi: 10.1088/0004-637X/809/1/77.
- M. Swain, P. Deroo, G. Tinetti, M. Hollis, M. Tessenyi, M. Line, H. Kawahara, Y. Fujii, A. P. Showman, and S. N. Yurchenko. Probing the extreme planetary atmosphere of WASP-12b. *Icarus*, 225:432–445, July 2013. doi: 10.1016/j.icarus.2013.04.003.
- M. R. Swain, J. Bouwman, R. L. Akeson, S. Lawler, and C. A. Beichman. The Mid-Infrared Spectrum of the Transiting Exoplanet HD 209458b. *ApJ*, 674:482-497, February 2008. doi: 10.1086/523832.
- J. J. Swift, M. Bottom, J. A. Johnson, J. T. Wright, N. McCrady, R. A. Wittenmyer, P. Plavchan, R. Riddle, P. S. Muirhead, E. Herzig, J. Myles, C. H. Blake, J. Eastman, T. G. Beatty, S. I. Barnes, S. R. Gibson, B. Lin, M. Zhao, P. Gardner, E. Falco, S. Criswell, C. Nava, C. Robinson, D. H. Sliski, R. Hedrick, K. Ivarsen,

- A. Hjelstrom, J. de Vera, and A. Szentgyorgyi. Miniature Exoplanet Radial Velocity Array (MINERVA) I. Design, Commissioning, and First Science Results. *Journal of Astronomical Telescopes, Instruments, and Systems*, 1(2):027002, April 2015. doi: 10.1117/1.JATIS.1.2.027002.
- D. P. Thorngren, J. J. Fortney, R. A. Murray-Clay, and E. D. Lopez. The Mass-Metallicity Relation for Giant Planets. *ApJ*, 831:64, November 2016. doi: 10.3847/0004-637X/831/1/64.
- K. O. Todorov, D. Deming, H. A. Knutson, A. Burrows, P. V. Sada, N. B. Cowan, E. Agol, J.-M. Desert, J. J. Fortney, D. Charbonneau, G. Laughlin, J. Langton, A. P. Showman, and N. K. Lewis. Warm Spitzer Observations of Three Hot Exoplanets: XO-4b, HAT-P-6b, and HAT-P-8b. *ApJ*, 746:111, February 2012. doi: 10.1088/0004-637X/746/1/111.
- K. O. Todorov, D. Deming, H. A. Knutson, A. Burrows, J. J. Fortney, N. K. Lewis, N. B. Cowan, E. Agol, J.-M. Desert, P. V. Sada, D. Charbonneau, G. Laughlin, J. Langton, and A. P. Showman. Warm Spitzer Photometry of Three Hot Jupiters: HAT-P-3b, HAT-P-4b and HAT-P-12b. *ApJ*, 770:102, June 2013. doi: 10.1088/0004-637X/770/2/102.
- K. O. Todorov, D. Deming, A. Burrows, and C. J. Grillmair. Updated Spitzer Emission Spectroscopy of Bright Transiting Hot Jupiter HD 189733b. *ApJ*, 796:100, December 2014. doi: 10.1088/0004-637X/796/2/100.
- A. H. M. J. Triaud, A. Collier Cameron, D. Queloz, D. R. Anderson, M. Gillon, L. Hebb, C. Hellier, B. Loillet, P. F. L. Maxted, M. Mayor, F. Pepe, D. Pollacco, D. Ségransan, B. Smalley, S. Udry, R. G. West, and P. J. Wheatley. Spin-orbit angle measurements for six southern transiting planets. New insights into the dynamical origins of hot Jupiters. *A&A*, 524:A25, December 2010. doi: 10.1051/0004-6361/201014525.
- A. Tsiaras, I. P. Waldmann, M. Rocchetto, R. Varley, G. Morello, M. Damiano, and G. Tinetti. A New Approach to Analyzing HST Spatial Scans: The Transmission Spectrum of HD 209458 b. *ApJ*, 832:202, December 2016. doi: 10.3847/0004-637X/832/2/202.
- A. Tsiaras, I. P. Waldmann, T. Zingales, M. Rocchetto, G. Morello, M. Damiano, K. Karpouzas, G. Tinetti, L. K. McKemmish, J. Tennyson, and S. N. Yurchenko. A population study of hot Jupiter atmospheres. *ArXiv e-prints*, April 2017.
- K. Tsiganis, R. Gomes, A. Morbidelli, and H. F. Levison. Origin of the orbital architecture of the giant planets of the Solar System. *Nature*, 435:459–461, May 2005. doi: 10.1038/nature03539.
- F. Valsecchi and F. A. Rasio. Tidal Dissipation and Obliquity Evolution in Hot Jupiter Systems. *ApJ*, 786:102, May 2014. doi: 10.1088/0004-637X/786/2/102.

- A. Vidal-Madjar, A. Lecavelier des Etangs, J.-M. Désert, G. E. Ballester, R. Ferlet, G. Hébrard, and M. Mayor. An extended upper atmosphere around the extrasolar planet HD209458b. *Nature*, 422:143–146, March 2003. doi: 10.1038/nature01448.
- H. R. Wakeford, D. K. Sing, D. Deming, N. P. Gibson, J. J. Fortney, A. S. Burrows, G. Ballester, N. Nikolov, S. Aigrain, G. Henry, H. Knutson, A. Lecavelier des Etangs, F. Pont, A. P. Showman, A. Vidal-Madjar, and K. Zahnle. HST hot Jupiter transmission spectral survey: detection of water in HAT-P-1b from WFC3 near-IR spatial scan observations. *MNRAS*, 435:3481–3493, November 2013. doi: 10.1093/mnras/stt1536.
- H. R. Wakeford, D. K. Sing, T. Kataria, D. Deming, N. Nikolov, E. D. Lopez, P. Tremblin, D. S. Amundsen, N. K. Lewis, A. M. Mandell, J. J. Fortney, H. Knutson, B. Benneke, and T. M. Evans. HAT-P-26b: A Neptune-mass exoplanet with a well-constrained heavy element abundance. *Science*, 356:628–631, May 2017a. doi: 10.1126/science.aah4668.
- H. R. Wakeford, K. B. Stevenson, N. K. Lewis, D. K. Sing, M. López-Morales, M. Marley, T. Kataria, A. Mandell, G. E. Ballester, J. Barstow, L. Ben-Jaffel, V. Bourrier, L. A. Buchhave, D. Ehrenreich, T. Evans, A. García Muñoz, G. Henry, H. Knutson, P. Lavvas, A. Lecavelier des Etangs, N. Nikolov, and J. Sanz-Forcada. HST PanCET program: A Cloudy Atmosphere for the Promising JWST Target WASP-101b. *ApJL*, 835:L12, January 2017b. doi: 10.3847/2041-8213/835/1/L12.
- H. R. Wakeford, C. Visscher, N. K. Lewis, T. Kataria, M. S. Marley, J. J. Fortney, and A. M. Mandell. High-temperature condensate clouds in super-hot Jupiter atmospheres. *MNRAS*, 464:4247–4254, February 2017c. doi: 10.1093/mnras/stw2639.
- I. P. Waldmann, G. Tinetti, P. Deroo, M. D. J. Hollis, S. N. Yurchenko, and J. Tennyson. Blind Extraction of an Exoplanetary Spectrum through Independent Component Analysis. *ApJ*, 766:7, March 2013. doi: 10.1088/0004-637X/766/1/7.
- K. J. Walsh, A. Morbidelli, S. N. Raymond, D. P. O’Brien, and A. M. Mandell. Populating the asteroid belt from two parent source regions due to the migration of giant planets: “The Grand Tack”. *Meteoritics and Planetary Science*, 47: 1941–1947, December 2012. doi: 10.1111/j.1945-5100.2012.01418.x.
- N. N. Weinberg, P. Arras, E. Quataert, and J. Burkart. Nonlinear Tides in Close Binary Systems. *ApJ*, 751:136, June 2012. doi: 10.1088/0004-637X/751/2/136.
- L. M. Weiss, G. W. Marcy, J. F. Rowe, A. W. Howard, H. Isaacson, J. J. Fortney, N. Miller, B.-O. Demory, D. A. Fischer, E. R. Adams, A. K. Dupree, S. B. Howell, R. Kolbl, J. A. Johnson, E. P. Horch, M. E. Everett, D. C. Fabrycky, and S. Seager. The Mass of KOI-94d and a Relation for Planet Radius, Mass, and Incident Flux. *ApJ*, 768:14, May 2013. doi: 10.1088/0004-637X/768/1/14.

- G. W. Wetherill. The Formation and Habitability of Extra-Solar Planets. *Icarus*, 119:219–238, January 1996. doi: 10.1006/icar.1996.0015.
- D. C. B. Whittet. Oxygen Depletion in the Interstellar Medium: Implications for Grain Models and the Distribution of Elemental Oxygen. *ApJ*, 710:1009–1016, February 2010. doi: 10.1088/0004-637X/710/2/1009.
- A. N. Wilkins, D. Deming, N. Madhusudhan, A. Burrows, H. Knutson, P. McCullough, and S. Ranjan. The Emergent 1.1–1.7 μm Spectrum of the Exoplanet CoRoT-2b as Measured Using the Hubble Space Telescope. *ApJ*, 783:113, March 2014. doi: 10.1088/0004-637X/783/2/113.
- A. N. Wilkins, L. Delrez, A. J. Barker, D. Deming, D. Hamilton, M. Gillon, and E. Jehin. Searching for Rapid Orbital Decay of WASP-18b. *ApJL*, 836:L24, February 2017. doi: 10.3847/2041-8213/aa5d9f.
- J. N. Winn. *Exoplanet Transits and Occultations*, pages 55–77. University of Arizona Press, December 2010.
- J. N. Winn, M. J. Holman, G. Torres, P. McCullough, C. Johns-Krull, D. W. Latham, A. Shporer, T. Mazeh, E. Garcia-Melendo, C. Foote, G. Esquerdo, and M. Everett. The Transit Light Curve Project. IX. Evidence for a Smaller Radius of the Exoplanet XO-3b. *ApJ*, 683:1076–1084, August 2008. doi: 10.1086/589737.
- A. Wolszczan and D. A. Frail. A planetary system around the millisecond pulsar PSR1257 + 12. *Nature*, 355:145–147, January 1992. doi: 10.1038/355145a0.
- J. P. Zahn. Les marées dans une étoile double serrée (suite). *Annales d’Astrophysique*, 29:489, February 1966.
- J. P. Zahn. Tidal friction in close binary stars. *A&A*, 57:383–394, May 1977.
- K. Zhang and D. P. Hamilton. Orbital resonances in the inner neptunian system. II. Resonant history of Proteus, Larissa, Galatea, and Despina. *Icarus*, 193:267–282, January 2008. doi: 10.1016/j.icarus.2007.08.024.
- G. Zhou, D. D. R. Bayliss, L. Kedziora-Chudczer, C. G. Tinney, J. Bailey, G. Salter, and J. Rodriguez. Secondary eclipse observations for seven hot-Jupiters from the Anglo-Australian Telescope. *MNRAS*, 454:3002–3019, December 2015. doi: 10.1093/mnras/stv2138.
- Y. Zhou, D. Apai, B. W. P. Lew, and G. Schneider. A Physical Model-based Correction for Charge Traps in the Hubble Space Telescope’s Wide Field Camera 3 Near-IR Detector and Its Applications to Transiting Exoplanets and Brown Dwarfs. *AJ*, 153:243, June 2017. doi: 10.3847/1538-3881/aa6481.